UNIVERSITY OF CALIFORNIA

Los Angeles

Use of Dynamic Optical Contrast Imaging (DOCI) for Head & Neck Surgical Applications

A dissertation submitted in partial satisfaction of the

requirements for the degree Doctor of Philosophy

in Materials Science and Engineering

by

Shan Huang

2022

© Copyright by

Shan Huang

2022

ABSTRACT OF THE DISSERTATION

Use of Dynamic Optical Contrast Imaging (DOCI) for Head & Neck Surgical Applications

by

Shan Huang

Doctor of Philosophy in Materials Science and Engineering

University of California, Los Angeles, 2022

Professor Maie A. R. St. John, Co-Chair

Professor Ya-Hong Xie, Co-Chair

In surgical oncology, intraoperative tissue identification is vital for the ideal surgical outcome: resection of the entire tumor tissue and maximum preservation of the adjacent normal tissue. Meanwhile, the need for negative margins should be carefully balanced against excessive resection of healthy tissue which can result in significant patient morbidity. Currently, intraoperative tissue identification relies on a combination of visual cues, palpation, and surgeon experience as well as frozen section. In this dissertation, we demonstrate that Dynamic Optical Contrast Imaging (DOCI) can help surgeons accurately identify tissue intraoperatively. DOCI is a label-free and non-invasive optical modality that provides relative fluorescence lifetime images with extremely short acquisition and computational times. We report recent progress on system implementation towards intraoperative use, as well as systematically characterized performance

of the system. We report the use of DOCI system in several head and neck surgical applications. Data from animal tissue shows that DOCI accurately differentiates tissue type and clearly delineate margins from mouse cancer models. Results from *ex vivo* experiments demonstrate that DOCI enables sensitive and specific mapping of hypercellular parathyroid gland. It is demonstrated that DOCI allows for real-time visualization and accurate delineation of OCSCC and adjacent healthy tissue, and that DOCI can be used in to clearly delineate margins between oropharyngeal cancer and surrounding healthy tissue.

The dissertation of Shan Huang is approved.

Ramesh Shori

Jaime Marian

Ximin He

Ya-Hong Xie, Committee Co-Chair

Maie A. R. St. John, Committee Co-Chair

University of California, Los Angeles

2022

Dedicated to my family.

Table of Contents

Table of Figures

Table of Tables

Acknowledgements

My Ph.D. study in UCLA would not be accomplished without the support, guidance, companionship, and help from my advisors, family, colleagues, and friends. I want to thank all the great people I met in UCLA.

First and foremost, I acknowledge my great thank to my committee members Dr. Maie St. John, Dr. Ya-Hong Xie, Dr. Ramesh Shori, Dr. Ximin He, and Dr. Jaime Marian for their patient mentorship and providing a flexible and accessible research environment that allowed many of the exploratory work. I would also like to thank my former committee member Dr. Oscar Stafsudd and his wife Jacquie Stafsudd for their unreserved guidance.

I appreciate the current and past members in Dr. St. John's lab, Dr. Alhiyari Yazeed, Dr. Yong Hu, Dr. Kenric Tam, Dr. Albert Han, and Dr. Peter Pellionisz, for their guidance and assistance in my Ph.D. study. I would also like to thank Dr. Peter Yu for his efforts in circuit development. To Songping (Catherina) Sun, Jake Pensa, and Dr. Rory Geoghegan for their help in 3D printing.

All the clinical work was made possible by our clinical collaborators from UCLA Ronald Reagan Medical Center that contributed to the research. I am grateful to Dr. Jeffrey Krane, Ko Kiehle, Jennifer Filipek, Jessica Jones, Zhongyi Zhang, Flores Marin, Alvin Ramos, Pam Chitvanith, Grahamn Tobby Guiao, and Jesse Heinrichs for spending their valuable time supporting our work. I also want to thank all the operating room personnel for their patience with experimenting new research process.

I would like to extend my appreciation to the fellow graduate students I met in the Department of Materials Science and Engineering. I have benefited a lot from working with Dr.

Jimmy Ng, Dr. Xinke Yu, Dr. Peiyi Ye, Dr. Owen Liang, Dr. Shiqi Dong, Dr. Yao Yang, Zirui Liu, Jun Liu, Tieyi Li and Ming Dong.

Last, I would like to thank my family. My special thank goes to my wife, Danyang Wang, for accompanying me throughout all the years of my Ph.D. study. Thank you to my parents and parents-in-law, who have been always supportive. To our cats, Yuwan (Fishball) and Meiqiu (Lucky) for their emotional support.

VITA

2014	B.S. in Microelectronics
	Fudan University
	Shanghai, China
2017	M.S. in Microelectronics and Solid State Electronics
	Fudan University
	Shanghai, China

Chapter 1. Introduction

1.1. Medical Imaging

Medical imaging refers to the technology and process of obtaining internal tissue images of the human body or a certain part of the human body in a non-invasive way for medical treatment or medical research. The origins of medical imaging can be traced back to the discovery of X-rays 127 years ago. When high-energy ionizing radiation passes through different tissue structures of the human body, the degree of absorption is different, and images with different contrasts of light and dark or black and white are formed on the screen or X-ray film. In the 1950s nuclear imaging and ultrasound were successively applied to medicine, the former uses certain properties of isotopes and high-energy particles emitted by radioactive substances to diagnose various lesions, such as positron emission tomography (PET), while the latter uses high-frequency broadband sound waves to be reflected by tissues to produce pictures. In the 1970s, computed tomography (CT) and magnetic resonance imaging (MRI) were introduced into medical diagnosis. CT visualizes the internal structure of the body by taking images of a series of slices of the body and then putting them back together with a computer. MRI maps the interaction of hydrogen nuclei proton spins immersed in a magnetic field and stimulated by radio frequency (RF) pulses. Today, after a long development spanning more than 120 years, medical imaging plays a pivotal role in the screening, diagnosis, and monitoring of diseases.

1.2. Image-Guided Surgery

The role of medical imaging in oncology is very important, it is often involved in the entire treatment process. Taking the treatment of cancer of the oral cavity as an example, the diagnosis

and treatment process can be divided into five parts: workup, clinical staging, treatment of primary and neck, adjuvant treatment, and follow-up. Workup is used to identify if a patient has tumor, to classify the kind of tumor, and to characterize the tumor. Primary methods used in workup include history and physical (H&P) examination, biopsy, imaging, multidisciplinary consultation, and other examinations, evaluations, and counseling. According to the results of workup, the disease can be clinically staged from the three perspectives of primary tumor (T), regional lymph nodes (N) and distant metastasis (M), which is also known as the TNM system. Depending on the staging, surgery, radiation therapy, systemic therapy, or clinical trials is applied in the treatment of primary and neck. Adjuvant treatment, which is usually a new round of therapy using the methods mentioned above, is used if adverse features, such as positive/close margins, perineural invasion, or lymphatic invasion, are observed. After treatment, patients participate in follow-up care, such as H&P examination, imaging, supportive care, and rehabilitation, to watch for recurrence, manage any side effects, and monitor overall health.

In addition to the use of medical imaging in workup and follow-up, the application of medical imaging in surgery is also of great value. This type of surgery involving medical imaging is also known as image-guided surgery. In surgical oncology, intraoperative tissue identification is vital for the ideal surgical outcome: resection of the entire tumor tissue and maximum preservation of the adjacent normal tissue. Meanwhile, the need for negative margins should be carefully balanced against excessive resection of healthy tissue which can result in significant patient morbidity. For example, within the anatomic confines of the head and neck, excessively wide margins with over-resection of healthy tissue can result in deficits to speech and swallowing. Surgeons rely on visual cues, palpation, surgeon experience, frozen section consultation, and intraoperative imaging to assess the margin.

For many years, the mainstay of image-guided surgery includes X-ray fluoroscopy, ultrasound, and near-infrared (NIR) imaging. The use of fluoroscopy exposes operating room (OR) personnel to ionizing radiation, as a result, cumbersome bulky personal protective equipment is needed as well as a shielded medical suite [1]. Intraoperative ultrasound requires direct tissue contact for best contrast visualization, the existence of various ultrasound artifacts such as acoustic enhancement artifacts may make intraoperative ultrasound unreliable [2]. NIR imaging is a kind of fluorescence imaging that uses NIR light as excitation light and detects fluorescence emission between 700 to 900 nm, but typically a contrast agent such as indocyanine green (ICG) needs to be injected into the body for best contrast [3]. As a fluorescence intensity-based technique, NIR imaging is greatly influenced by intensity artifacts that are associated with ambient light, local concentration of fluorophores, local illumination intensity, optical path, target geometry and detection efficiency. MRI has limited use for image-guided surgery, while MRI provides excellent soft tissue contrast, it is not sufficiently sensitive for the detection of microscopic disease [4], and the imaging at a fine resolution takes around 1 hour [5]. The large magnetic field needed to generate images is incompatible with most other medical devices, this logistic disadvantage also limits the use of MRI to pre- and post-operative margin assessment.

Attempts have been made to integrate scanners for CT, PET and MRI into operating rooms (ORs) and interventional suites [6], such as the Advanced Multimodal Image-Guided Operating (AMIGO) suite at Brigham and Women's Hospital in Boston [7]. More widely adopted are portable scanners compatible with regular OR environment, yet they still have limitations including lack of specificity for tumor tissue, long scan time, and high cost [8].

1.3. Emerging Optical Imaging Modalities

There exists a multitude of optical imaging modalities used for identification and localization of tissues of specific interest, such as hyperspectral imaging (HIS) [9, 10], autofluorescence imaging, fluorescence lifetime imaging microscopy (FLIM), and Raman spectroscopy. HSI combines a set of two-dimensional images across a wide range of the electromagnetic spectrum to generate a three-dimensional dataset, also known as a hyperspectral cube. HSI can provide diagnostic information on tissues composition beyond the natural capabilities of human vision, it can be used to spatially delineate tumors without the need for exogenous contrast [11]. The available HSI systems are still relatively bulky and expensive, limiting the diffusion of this technology in the operating room [12].

The development of autofluorescence imaging has had some interest as it's a real-time imaging method that can rely on endogenous biological fluorophores or the use of a fluorescently labeled biological agent. Several studies have investigated direct autofluorescence use for margin detection in the intraoperative settings [13], however the accuracy rate of detection was limited.

Pulsed light-based imaging paradigms like fluorescence lifetime imaging microscopy (FLIM) and Raman spectroscopy have largely remained incompatible for real-time or intraoperative imaging. FLIM has been used in a wide range of studies demonstrating its ability to identify head and neck cancer [14-18], brain tumor [19, 20], skin lesion [21] and parathyroid gland [22] under *in vivo* settings. *Ex vivo* studies have also been carried out on breast cancer [23-25], urothelial carcinoma [26], corneal collagen crosslinking [27], and colon diseases [28]. Raman [29] has more recently joined the fray of cancer detection. The major limitation with all these techniques is the lack of wide-field ability. Images or measurements are taken in raster format with a scanning laser, thus producing long image acquisitions. Furthermore, traditional FLIM is

computationally intensive as exacting lifetime measurements requires solving complicated mathematics. This has led many research groups to utilize mathematic equations that are approximations that are faster to solve (reducing accuracy) or attempting to improve photon efficiency (at the expense of field of view) [30]. The collection of enough photons is what limits Ramen spectroscopy and FLIM from achieving real-time imaging regardless of the individual unique limitations between each modality.

1.4. Dynamic Optical Contrast Imaging (DOCI)

Although optical imaging methods (HSI, fluorescence imaging) have shown great potential, imaging results are susceptible to ambient light changes so usually the room lights need to be turned off, they could also be invasive if injection of fluorescent probes is needed. FLIM is a powerful tool for *ex vivo* biomedical applications but is impractical for providing real-time intraoperative guidance due to the long time for data acquisition and data analysis. An affordable, non-invasive, rapid, and accurate technique for intraoperative imaging would benefit surgeons and their patients across all disciplines, guiding accuracy of biopsies, increasing adequacy of resections, and in some instances even providing diagnostic information [31].

Dynamic optical contrast imaging (DOCI) was developed [32, 33] to provide relative fluorescence lifetime images with extremely short acquisition and computational times. It generates contrast from relative differences in endogenous fluorophore lifetimes without having to compute the absolute lifetime values. Unlike most time-domain techniques that apply excitation light pulses with short pulse width, DOCI utilizes a relatively long pulse width with a short fall time to capture the lifetime difference of different fluorophores. It overcomes the limitations of other fluorescence-based techniques such as fluorescence imaging and FLIM and is therefore more suitable for image-guided surgery.

1.5. Thesis Overview

This thesis is divided into 6 chapters, which go from the system design of DOCI to the application in its tissue differentiation. Chapter 1 reviews the development of medical imaging and discusses the importance of a reliable imaging modality for image-guided surgery.

Chapter 2 and chapter 3 describe the principle of DOCI and current progress in system implementation. After introducing the theory and mathematical model, we provide simulation results to demonstrate the rationale for finding suitable parameters. The recent iterations of system implementation are discussed each with specific improvements. System is characterized and validated in terms of the spectral and temporal performances.

Chapter 4 shows the adaption of the implemented system to animal tissue differentiation. The system is first validated on *ex vivo* and *in vivo* porcine tissues, results show clear differences of data from different tissue types including adipose, lymph node, muscle, thymus, and thyroid. The system is also validated on *in vivo* murine models, results show the margin between tumor tissue and adjacent healthy tissues is accurately delineated.

Chapter 5 is focused on the identification of hypercellular parathyroid gland *ex vivo*. The system is validated on an *ex vivo* dataset with a total of 115 tissue specimen obtained from 47 patients. Results show DOCI and integrated machine learning algorithms can be utilized to visually differentiate and classify hypercellular parathyroid adenomas from normal parathyroid glands and surrounding tissues.

Chapter 6 presents the results from *ex vivo* and *in vivo* oral and oropharyngeal squamous cell carcinoma imaging. Statistical difference is found between DOCI data from tumor tissue and healthy tissue, *in vivo* imaging results demonstrate DOCI is able to detect the tumor margin. By

replacing the camera lens with an endoscope, DOCI has the capability to locate the tumor margins of oropharyngeal cancers.

Chapter 7 concludes the dissertation by giving a summary of the key findings in this thesis work, future directions that can build on the results presented herein are discussed.

Chapter 2. DOCI Theory and Model

2.1. Fluorescence and Fluorescence Lifetime

Fluorescence is one of the two categories of luminescence (fluorescence and phosphorescence) that is caused by the absorption of light at one wavelength followed by nearly immediate light emission usually at a different wavelength. It ceases almost at once when the incident radiation stops. In the excited singlet state of the fluorophore, the electron in the excited orbital is paired with the second electron in the ground state orbital (via the opposite spin). Therefore, returning to the ground state is spin allowed, and occurs rapidly by the allowed emission of a photon.

The process of fluorescence contains 3 steps: light absorption, internal conversion, and photon emission. First, absorption of light excites the fluorophore to a higher vibrational level from the ground state level. Then it quickly relaxes to the lowest vibrational level through internal conversion, this internal conversion process usually happens within 10^{-12} s [34]. Last, the fluorophore returns to a vibrational ground state level, emits a fluorescent photon and completes the fluorescence emission.

For a fluorophore, there are two important properties: quantum yield and fluorescence lifetime. Quantum yield is the ratio between the number of emitted photons and absorbed photons, it is defined by the fraction of excited state fluorophores that decay through fluorescence. Fluorescence lifetime is the average time that fluorophores spend in the excited state before returning to the ground state. The lifetime can be extracted using a single excitation wavelength. Changes in the lifetime reveal important metabolic information that is independent of pumped intensity but is sensitive to environmental changes such as pH, temperature and viscosity [35].

Suppose a fluorophore sample is excited with an ideal light impulse., as is shown in Figure 2.1. This results in an initial population (n_0) of fluorophores in the excited state. The population decays with a rate $\Gamma + k_{nr}$:

$$\frac{dn(t)}{dt} = (\Gamma + k_{nr})n(t)$$

where $n(t)$ is the population of excited fluorophores at time t following the pulse of light; Γ is the emissive rate; and k_{nr} is the non-radiative decay rate. After integration, the population of fluorophores in the excited state ($n(t)$) has an exponential decay profile:

$$n(t) = n_0 \exp(-t/\tau)$$

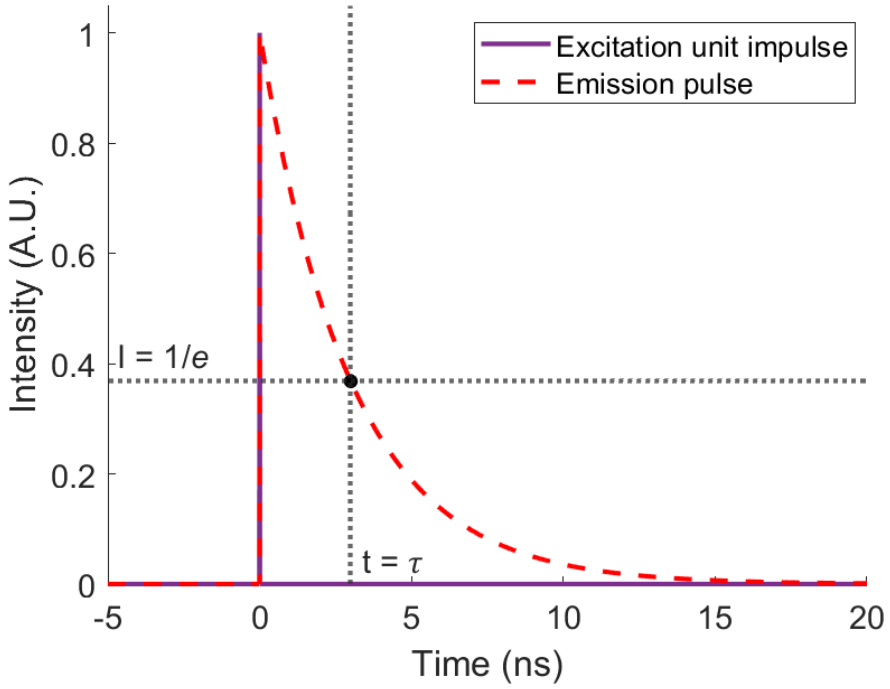

Figure 2.1 Fluorescence response to an excitation pulse

The population $n(t)$ can also be represented by the time-dependent intensity of fluorescence $I(t)$:

$$I(t) = I_0 \exp(-t/\tau)$$

and τ is the inverse of the total decay rate $\tau = (\Gamma + k_{nr})^{-1}$. The average time of the fluorophore staying in the excited state $\bar{t}$ can be calculated by:

$$\bar{t} = \frac{\int_0^\infty tI(t)dt}{\int_0^\infty I(t)dt} = \frac{\int_0^\infty tI_0\exp(-t/\tau)dt}{\int_0^\infty I_0\exp(-t/\tau)dt} = \tau$$

Therefore, for a single exponential decay, the fluorescence lifetime equals to the time the fluorophore requires to decay to the probability of 1/e (0.37). If several fluorophores contribute to the fluorescence decay, $I(t)$ becomes a multi exponential decay:

$$I(t) = \sum_{i=0}^{n} I_i\exp(-t/\tau_i)$$

with I_i being the amplitude and τ_i being the fluorescence lifetime of the *i*th fluorophore.

2.2. Intrinsic Fluorophores in Cells and Tissues

Fluorophores can be classified into two categories based on origin: intrinsic fluorophores and extrinsic fluorophores. Intrinsic fluorophores are those that occur naturally. There are mainly various intrinsic fluorophores that exist in cells and tissues, such as aromatic amino acids (phenylalanine, tyrosine, tryptophan), redox-active coenzymes (nicotinamide adenine dinucleotide (NADH) and its phosphate derivative (NADPH), flavin adenine dinucleotide (FAD)), structural proteins (collagen and elastin), and fluorescent pigments (melanin). Their unique fluorescent features such as excitation wavelength, emission wavelength and lifetime (Table 2.1) make it possible for us to monitor the metabolic state and constitution of the sample in a label-free and non-invasive manner.

Table 2.1 Representative intrinsic fluorophores responsible for autofluorescence in cells and tissues [36]

Fluorophore	**Excitation (nm)**	**Emission (nm)**	**Lifetime (ns)**
phenylalanine	258 (max)	280 (max)	7.5
tyrosine	275 (max)	300 (max)	2.5

tryptophan	280 (max)	350 (max)	3.03
NAD(P)H free	300-380	450-500	0.3
NAD(P)H protein bound	300-380	450-500	2.0-2.3
FAD	420-500	520-570	2.91
FAD protein bound	420-500	520-570 (weak)	<0.01
collagen	280-350	370-440	≤5.3
elastin	300-370	420-460	≤2.3
melanin	300-800	440,520,575	0.1/1.9/8

2.3. Fluorescence Lifetime Imaging Microscopy (FLIM)

Conventionally, there are two types of imaging techniques that monitors fluorescence activity, fluorescence imaging and fluorescence lifetime imaging (FLIM). Fluorescence imaging generates contrast based on emission intensity, while FLIM produces an image based on the differences in the fluorescence decay parameters from a fluorescent sample. FLIM has several advantages in studying a sample's fluorescence. First, it resolves fluorophores with overlapping emission spectra but with different lifetimes; second, it reveals environmental changes such as in temperature and pH; third, it is independent of light intensity, thus provides robust quantitative measurements.

FLIM techniques can be classified into two categories: time-domain and frequency-domain. In time-domain, the fluorescent sample is excited by a pulse of light with short pulse width and sufficient delay between pulses. The time-dependent intensity decay curve is measured after the excitation pulse, and the lifetime can be extracted from the slope of a logarithmic plot of emission intensity versus time. Common time-domain FLIM techniques are time correlated single photon counting (TCSPC), gated detection and pulsed sampling [37]. TCSPC is the most commonly used

technique for time-domain measurements because of its high sensitivity and low degree of systematic errors [38]. The sample is excited by the periodic light pulses with extremely short pulse width, the time between the excitation pulse and the first observed photon is recorded. No more than one photon can be detected per laser pulse, a typical detection rate is 1 photon per 100 excitation pulses.

The time-domain FLIM using gated methods repetitively samples the intensity decay during pulsed excitation. It is usually realized using a time-gated detector. In this case, a series of limited excitation pulses are used to induce the fluorescence emission of the sample. The detector integrates the fluorescence intensity at each different delay time along the attenuation curve and uses it to reconstruct the attenuation curve (intensity versus time). This detection technique is preferred in wide-field FLIM [39, 40].

Unlike the gated method, the pulsed sampling technique keeps the detector on until the entire fluorescent decay is detected. The resulting emission pulse signal is then sampled using a digitizer (e.g., digital oscilloscope) with a high sampling frequency and analog bandwidth (resolution of tens of picoseconds). In general, TCSPC technology (single photon) is characterized by high sensitivity and high time resolution, but the data collection speed is slow. In contrast, time-gated detection is characterized by rapid and simultaneous acquisition of all pixels, but the sensitivity is low, and moderate sample fluorescence emission is also required.

The frequency-domain or phase-modulation method relies on an intensity modulated excitation light source. This technique derives lifetime information from the measurement of the phase difference (ϕ_ω) between the sinusoidally modulated excitation and the resulting sinusoidally modulated fluorescent signal, where ω is the modulation frequency in radians/s. In addition, the finite response of the sample leads to demodulation of the transmission, as defined by the

demodulation factor M. The frequency-domain technique has the advantage of relatively simpler electronic instrumentation and excitation source requirements over the time-domain techniques, but the frequency-domain technique requires the sample to have relatively higher concentration and higher emission intensity [41].

The measured FLIM data is moderately complex, and in general cannot be analyzed using graphical methods [37]. Mathematically, the measured fluorescence intensity decay is the convolution of the fluorescence impulse response function (fIRF) with the instrument response [38], therefore, the fIRF should first be deconvoluted from the measured FLIM data before the lifetime is extracted. Among the various methods proposed for FLIM data analysis, the nonlinear least-square iterative method is most popular [30, 37, 38], but it is time-consuming because of the complex iterative process. Alternative methods such as the Laguerre polynomial analysis, the first-moment calculation and the rapid lifetime determination method were applied to reduce the calculation time [30]. Instead of extracting the lifetime value, phasor analysis also provides good representation of the decay profile by applying the Fourier transformation on the FLIM data [42].

2.4. DOCI Theory

Conventional FLIM techniques have yielded fruitful results for biomedical applications in the *ex vivo* laboratory environment but are impractical for providing real-time intraoperative guidance primarily due to the long time for data acquisition and computationally intensive data analysis. As an approach for *in vivo* application, DOCI was developed [32, 33] to provide relative fluorescence lifetime images with reduced acquisition time and computation time. The idea of DOCI is to generate contrast from relative differences in fluorescence lifetimes of different fluorophores, without having to compute the exact lifetime values. Particularly, unlike most time-domain techniques that apply excitation light pulses with extremely short pulse width, DOCI utilizes a

relatively long pulse width with a short fall time to capture the lifetime difference of different fluorophores.

Figure 2.2 graphically demonstrates the principle of DOCI. Figure 2.2 (a) shows the data acquisition process, a pulsed illumination source (purple) is used to excite the fluorescence emission (red). Three images are acquired to generate image with contrast from fluorescence lifetime difference: the first image (I_{SS}) is the reference image taken during the steady-state illumination stage, the fluorescence emission reaches and stays at the maximum; the second image (I_{DS}) is the decay image taken during the fluorescence decay stage, with the start of the falling edge of the excitation pulse, the emission also starts to decay; the third image (I_{BG}) is the background image taken when there is no excitation light and no fluorescence. The three images have identical window width for integration of light intensity. As is shown in Figure 2.2 (b), the DOCI image (I_{DOCI}) is then produced by pixel-wise calculation using I_{SS}, I_{DS} and I_{BG}:

$$I_{DOCI} = \frac{I_{DS} - I_{BG}}{I_{SS} - I_{BG}}$$

The background (I_{BG}) is subtracted from both I_{SS} and I_{DS} to eliminate the baseline bias. Ideally, value of pixels in I_{DOCI} ranges from 0 to 1, because the intensity during the decay stage should be less than during the steady-state stage, and the DOCI value has positive monotonic relationship to the fluorescence lifetime value. In the following 2 sections, we will elaborate on this from both the mathematical derivation and simulation approaches.

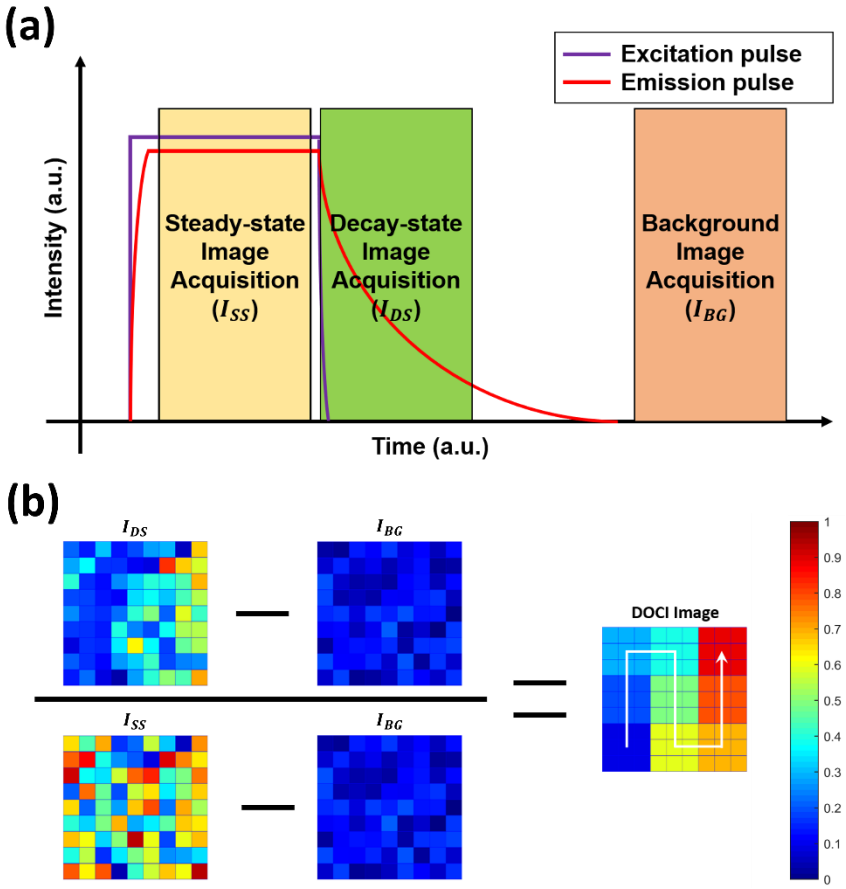

Figure 2.2 Principle of DOCI. (a) Image acquisition process; (b) DOCI image generation algorithm [43].

2.5. Mathematical Derivation

2.5.1. Single Fluorophore System

As mentioned, DOCI is a technique that seeks to generate contrast from relative differences in fluorophore lifetimes without the need to compute absolute lifetime values. This eliminates the complex and computationally intensive data fitting routines that has prevented successful translation of using fluorescence lifetime properties to intraoperatively differentiate tissue types [44]. Our previous work [33] have mathematically shown that for a single fluorophore, under

certain assumptions, its DOCI value and fluorescence lifetime value have a linear relationship. If we:

1. Model the time-dependent fluorescence intensity decay response $f(t)$ (Figure 2.3) using a similar single-exponential decay function with a decay lifetime of τ_{em}:

$$f(t) = I_0 \exp\left(-\frac{t}{\tau_{em}}\right)$$

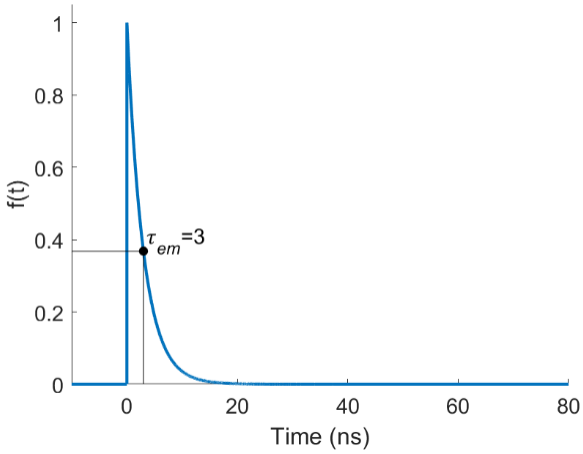

Figure 2.3 Example fluorescence intensity decay response $f(t)$ profile.

2. Model the excitation pulse $h(t)$ (Figure 2.4) using a function that is the convolution of a square pulse with pulse width C and an unit impulse with decay lifetime of τ_{exc}:

$$h(t) = (u(t) - u(t - C)) * g(t)$$

$$u(t) = \begin{cases} 0, t < 0 \\ 1, t \geq 0 \end{cases}$$

$$g(t) = I_{exc} \exp\left(-\frac{t}{\tau_{exc}}\right)$$

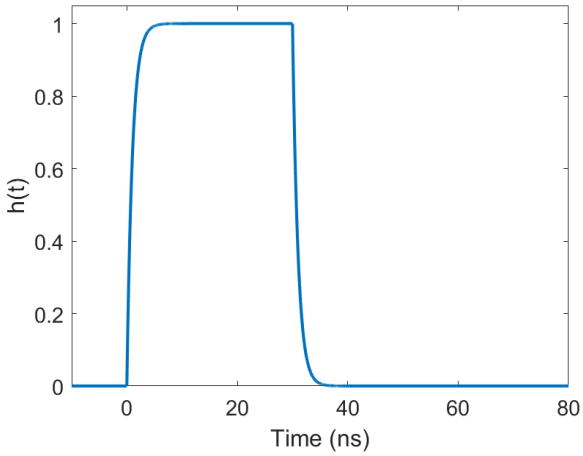

Figure 2.4 Example excitation pulse $h(t)$ profile.

3. Define $q(t)$ (Figure 2.5(b)) as a finite integration of the convolution between the response function $f(t)$ and the pulse function $h(t)$ (Figure 2.5(a)):

$$q(t) = \int_0^t (f * h)(t)dt$$

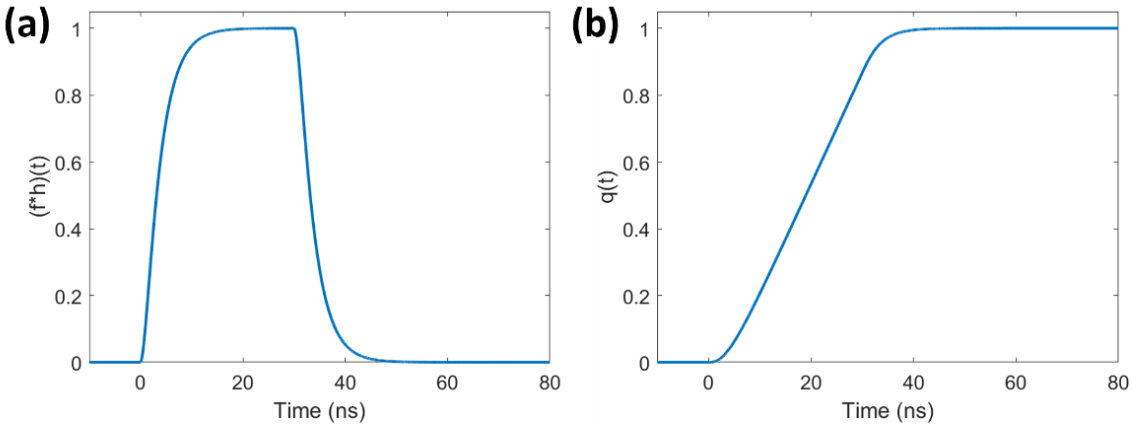

Figure 2.5 Profile of (a) $(f * h)(t)$ and (b) $q(t)$.

4. Specify the following (Figure 2.6):

   a. The window width/integration time is B
   b. The reference window spans from $t = C - B$ to $t = C$
   c. The decay window spans from $t = C$ to $t = C + B$
   d. The pulse width is greater than the window width $C > B$

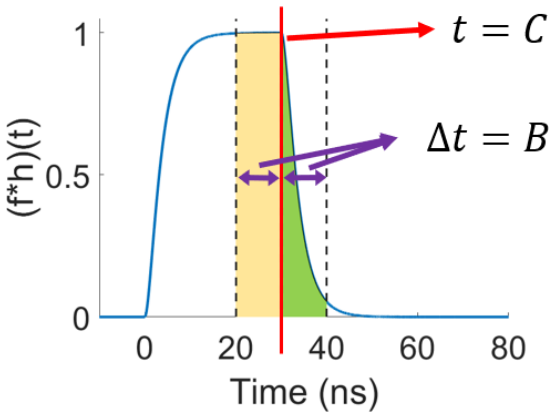

Figure 2.6 Illustrations of pulse width C and window width B, the yellow-shaded and green-shaded areas denote steady-state and decay-state intensities, respectively.

Then the corresponding DOCI value is given by:

$$DOCI = \frac{Decay\ State}{Steady\ State} = \frac{q(C+B) - q(C)}{q(C) - q(C-B)}$$

$$= \frac{{\tau_{em}}^2\left[1 + e^{-\frac{(C+B)}{\tau_{em}}} - e^{-\frac{C}{\tau_{em}}} - e^{-\frac{B}{\tau_{em}}}\right] - {\tau_{exc}}^2\left[1 + e^{-\frac{(C+B)}{\tau_{exc}}} - e^{-\frac{C}{\tau_{exc}}} - e^{-\frac{B}{\tau_{exc}}}\right]}{{\tau_{em}}^2\left[e^{-\frac{C}{\tau_{em}}} - e^{-\frac{(C-B)}{\tau_{em}}} + \frac{B}{\tau_{em}}\right] - {\tau_{exc}}^2\left[e^{-\frac{C}{\tau_{exc}}} - e^{-\frac{(C-B)}{\tau_{exc}}} + \frac{B}{\tau_{exc}}\right]}$$

The equation shows that when noise is not considered, the ideal DOCI method is insensitive to variation in illumination intensity (I_{exc}) as well as variation in fluorophore concentration, which affects I_0. The value of DOCI is determined by 4 variables: integration window width B, pulse width C, fluorophore's fluorescence lifetime τ_{em}, and excitation pulse's decay lifetime τ_{exc}. If we assume:

a. $C \gg B$
b. $B \gg \tau_{em}$
c. $B \gg \tau_{exc}$

we can have the approximated expression for the DOCI value:

$$DOCI \approx \frac{({\tau_{em}}^2 - {\tau_{exc}}^2)}{B(\tau_{em} - \tau_{exc})} = \frac{\tau_{em} + \tau_{exc}}{B}$$

The simplified equation shows the DOCI value is a function of τ_{em}, τ_{exc}, and B. For a working system, τ_{exc} and B are constants, therefore the DOCI value can be regarded positively linear to the fluorophore's decay lifetime τ_{em} under the constraint $B \gg \tau_{em}$. This condition can be easily satisfied as we already know most endogenous fluorophores have a lifetime value smaller than 10 ns [36], and the value of B can be set based on this knowledge.

2.5.2. Multiple Fluorophore System

More often, two or more fluorophores with different fluorescence lifetimes exist in a tissue, each contributing a different emission component to the calculation of DOCI:

$$DOCI = \frac{\sum Decay\ State_i}{\sum Steady\ State_i} = \frac{\sum[q_i(C+B) - q_i(C)]}{\sum[q_i(C) - q_i(C-B)]}$$

where $Decay\ State_i$ and $Steady\ State_i$ denote the integrated intensities of the *i*th fluorophore during the decay state and the steady state, respectively, and $q_i(t)$ refers to the integral of the emission response of the *i*th fluorophore.

If we assume the fluorescence activity of each fluorophore is independent, then the aggregated fluorescence is the direct sum of the fluorescence from each fluorophore. Then we can specify the fluorescence impulse response of the *i*th fluorophore is:

$$f_i(t) = \alpha_i \exp\left(-\frac{t}{\tau_{em,i}}\right)$$

α_i is the normalized amplitude of the *i*th fluorophore, the sum of α_i of all components is 1:

$$\sum \alpha_i = 1$$

Now if we assume from time $t = C - B$ to $t = C$, the emission stays at its peak amplitude, which means the steady-state intensity value is proportional to α_i:

$$Steady\ State_i = [q_i(C) - q_i(C-B)] \propto \alpha_i$$

Thus, the steady-state intensity of the *i*th fluorophore equals to the multiplication of α_i and the overall steady-state intensity:

$$Steady\ State_i = \alpha_i \sum Steady\ State_i$$

And the DOCI value can be expressed as:

$$DOCI = \frac{\sum Decay\ State_i}{\sum Steady\ State_i} = \sum \left(\frac{Decay\ State_i}{\sum Steady\ State_i}\right)$$

$$= \sum \left(\frac{Decay\ State_i}{Steady\ State_i/\alpha_i}\right) = \sum \alpha_i \frac{Decay\ State_i}{Steady\ State_i} = \sum \alpha_i DOCI_i$$

The equation shows the aggregate DOCI value is a linear combination of each single fluorophore's DOCI value.

2.6. Computer Simulation

To further explore the impact of different parameters on the relationship between DOCI value and fluorophore's fluorescence lifetime, we first show results of a series of simulations to evaluate 3 parameters, integration window width B, excitation pulse width C, and excitation pulse decay lifetime τ_{exc}, then we show simulated results of a representative 2-fluorophore system.

2.6.1. Integration Window Width *B*

The fluorescence emission curve can be described as the convolution of the sample's fluorescence decay response and the excitation response. Assuming the excitation pulse has ideal rising and falling edges and the pulse width is 100 ns, the fluorescence emission profiles with different fluorescence lifetimes from 0 to 10 ns are shown in Figure 2.7. The vertical dashed lines denote the integration windows for the steady-state and decay-state images. It is assumed the background activity is zero, so the background image is ignored here. Different fluorescence lifetimes are

coded with different colors, with shortest coded blue and longest code red. Longer fluorescence lifetime results slower rising and falling edge, as well as shorter period of steady state.

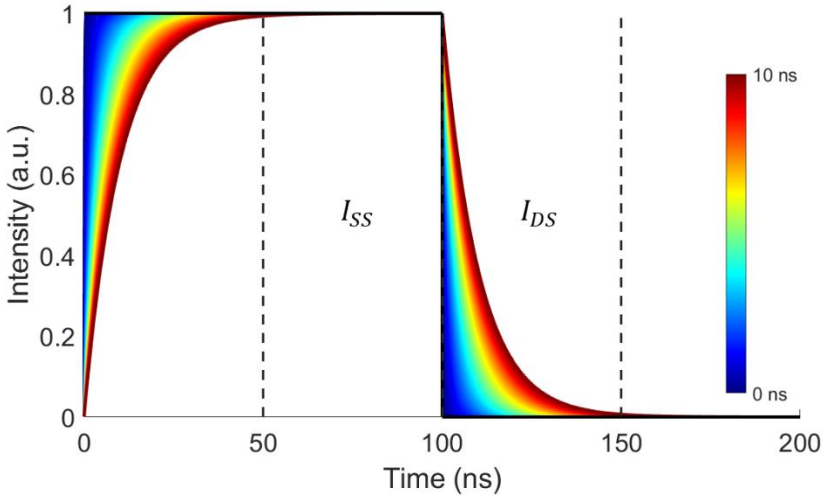

Figure 2.7 Excitation pulse profile and emission pulse profiles with different fluorescence lifetimes. The excitation pulse is plotted in black, it has ideal rising and falling edges.

Figure 2.8 shows the plots of DOCI values calculated on the emission pulses in Figure 2.7 using different integration window widths from 5 ns to 50 ns with an incremental of 5 ns. With a narrow integration window, the slope of the curve decreases as the lifetime value increases, because the increment in I_{DS} due to increased lifetime decreased. With increasing window width, the change in the slope value becomes smaller, and the relationship between lifetime and DOCI becomes more linear. Increased window width also reduces the dynamic range of DOCI value, as the increment in I_{SS} due to increased window width is greater than the increment in I_{DS}, and the difference keeps increasing. Although wider window improves the linearity of relationship between DOCI and fluorescence lifetime, it makes the image sensor more likely saturate for I_{SS} acquisition or more likely to undersample for I_{DS} acquisition. Therefore, from the perspective of hardware implementation, a moderate window width needs to consider both the relationship linearity and the sensor utilization.

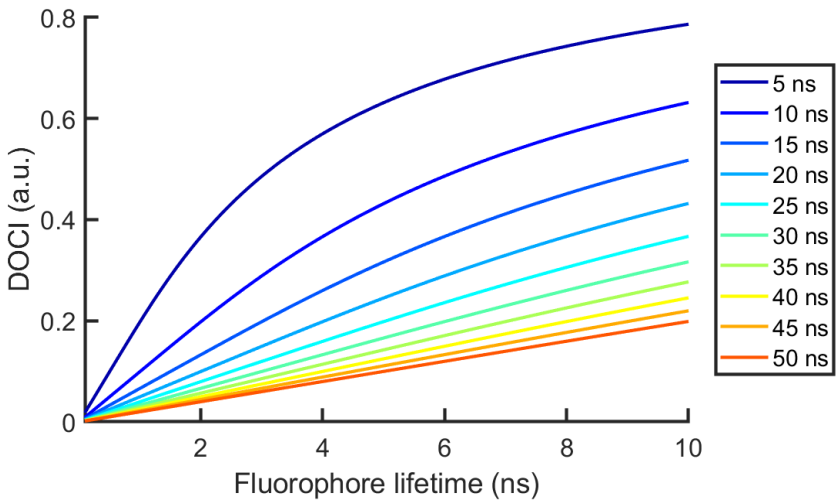

Figure 2.8 Plot of DOCI values calculated on the emission pulses in Figure 2.7 using different integration window widths.

2.6.2. Excitation Pulse Width C

At a fixed integration window width of 30 ns, Figure 2.9 (a) shows the DOCI values as a function of fluorophore lifetime at different excitation pulse widths. In this set of simulations, the excitation pulse has ideal rising and falling edges. The calculated DOCI values are consistent across different excitation pulse widths only except for the width of 30 ns and 50 ns. Figure 2.9 (b)-(d) are emission pulse profiles excited by pulses with pulse width of 30 ns, 50 ns, and 70 ns, respectively. With a short excitation pulse, if the fluorophore has a long lifetime compared to the excitation pulse width, its emission response is not able to reach the steady-state before the arrival of falling edge, thus the intensity of the steady-state image I_{SS} is reduced compared to those with a wide excitation pulse. The denominator term in the DOCI equation subsequently decreases, so the resultant DOCI value increases, and may result in a DOCI value larger than 1.

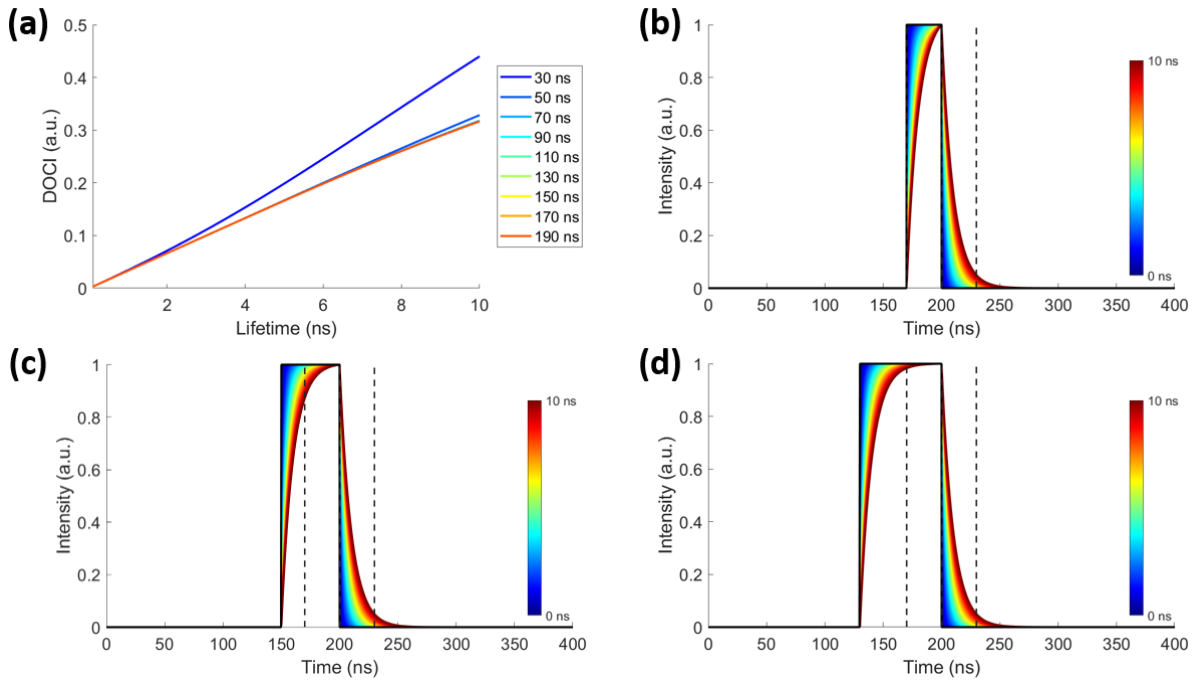

Figure 2.9 Effect of different excitation pulse widths on DOCI values. (a) DOCI as a function of fluorophore lifetime at different excitation pulse widths. (b)-(d) Emission pulse profiles excited by pulses with pulse width of 30 ns, 50 ns, and 70 ns, respectively. Dashed lines denote the integration windows for the steady-state and decay-state images.

2.6.3. Excitation Pulse Decay Lifetime τ_{exc}

It is impossible to create an ideal excitation pulse with perfect rising and falling edges in real life. If we model the decay activity of the excitation pulse using a single-exponential function, its decay activity can be described by the excitation pulse decay lifetime, and Figure 2.10 (a) shows the relationship between DOCI value, fluorophore's lifetime, and excitation decay lifetime. The excitation pulse has a pulse width of 100 ns to make sure every observation has reached steady state in the first integration window. Figure 2.10 (b)-(d) are emission pulse profiles excited by pulses with decay lifetimes of 0 ns, 10 ns, and 20 ns, respectively. As the decay lifetime of the excitation pulse increases, the curve in Figure 2.10 (a) moves upward to the larger end of the DOCI

value, the dynamic range of the DOCI value decreases, and the linearity of the curve becomes worse.

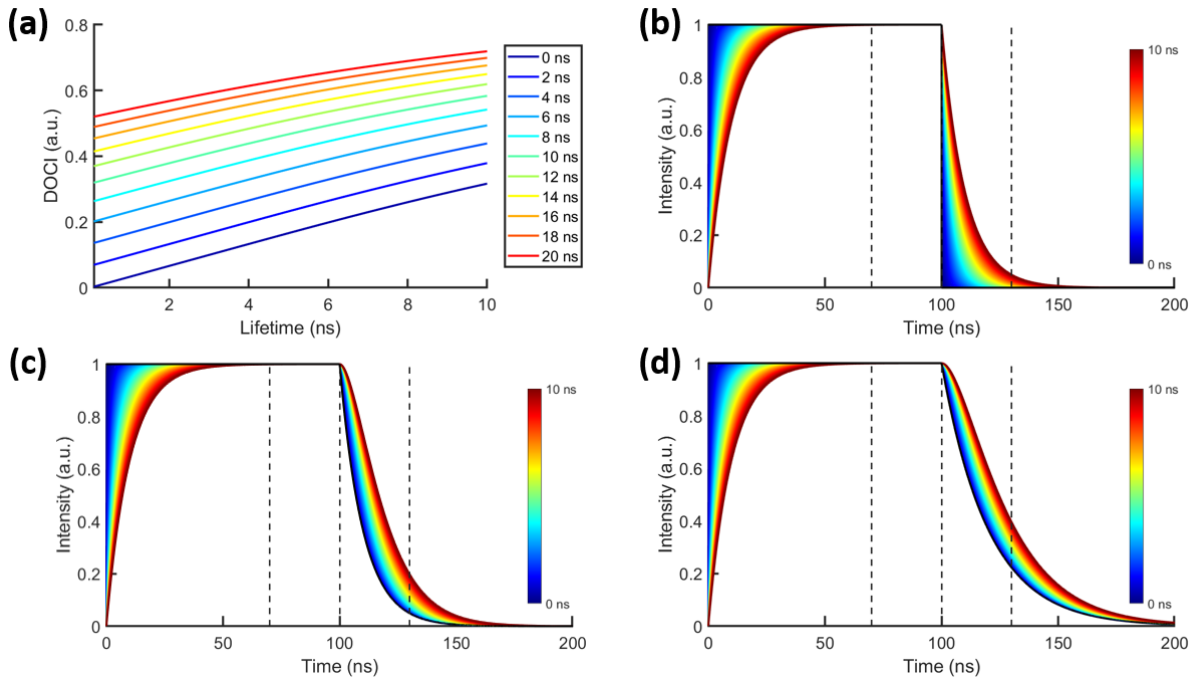

Figure 2.10 Effect of different excitation pulse decay lifetime on DOCI values. (a) DOCI as a function of fluorophore lifetime at different excitation pulse decay lifetimes. (b)-(d) Emission pulse profiles excited by pulses with decay lifetimes of 0 ns, 10 ns, and 20 ns, respectively. Dashed lines denote the integration windows for the steady-state and decay-state images.

2.6.4. 2-Fluorophore System

The simulation of multi-fluorophore emission can be complicated, here we show the simulation results from a two-fluorophore emission, assuming fluorophore A has a fluorescence lifetime of 1 ns, fluorophore B has a fluorescence lifetime of 10 ns, we evaluate the change of DOCI value when the proportion of the two in the fluorescence emission process changes. Figure 2.11 shows the results of DOCI plotted as a function of normalized amplitude of fluorophore A with different integration window widths (Figure 2.11 (a)), excitation pulse widths (Figure 2.11 (b)), or excitation

pulse decay lifetimes (Figure 2.11 (c)). The results are similar to those shown in Figure 2.8, Figure 2.9 (a), Figure 2.10 (a). A linear relationship can be properly maintained between the DOCI value and the normalized amplitude of fluorophore A, in other words, the DOCI value of the two-fluorophore system can be regarded as a linear combination of the two single-fluorophore systems.

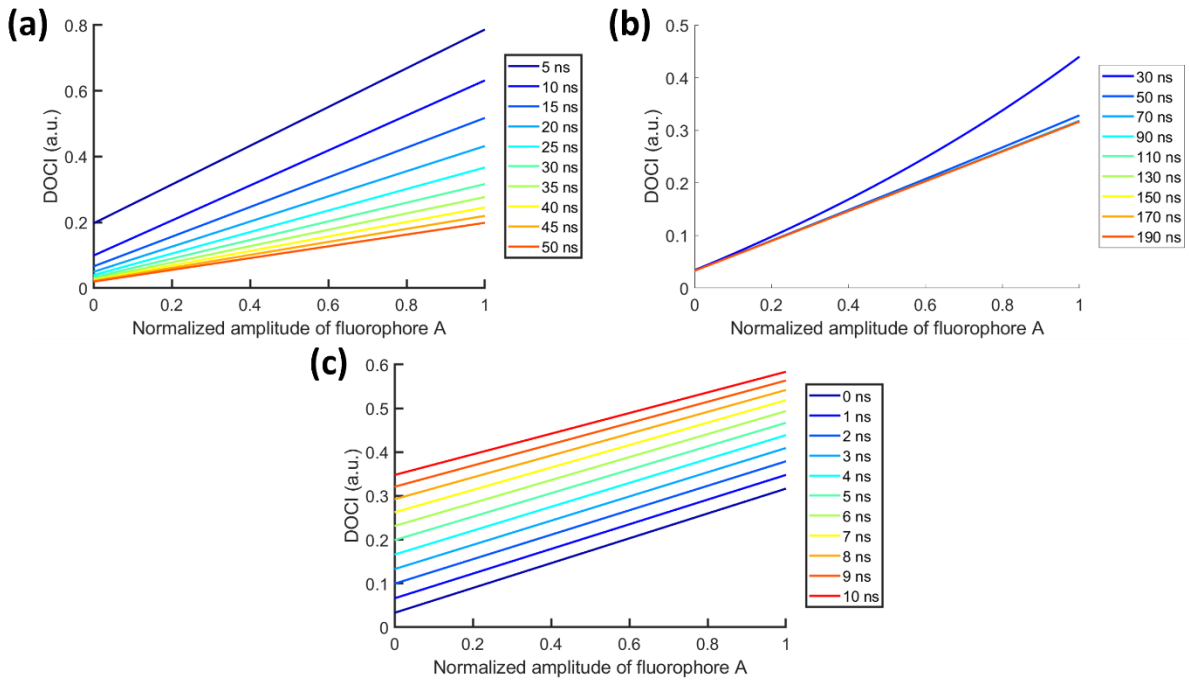

Figure 2.11 DOCI as a function of normalized amplitude of fluorophore A. (a) Results with different integration window widths. (b) Results with different excitation pulse widths. (c) Results with different excitation pulse decay lifetimes.

2.7. Conclusion

In this chapter, we introduced the theory and model of DOCI. The metabolic state and constitution of a biological sample can be revealed from its fluorescence activity, which can be monitored by DOCI in a label-free and non-invasive manner. Mathematical derivations and simulations have shown that the DOCI value has a monotonically increasing relationship with the fluorescence lifetime, by carefully setting the parameters, the relationship obtains a good linearity. DOCI of a

multiple fluorophore system can be regarded as a linear combination of DOCI of each single fluorophore system.

Chapter 3. DOCI System Implementation

3.1. System Composition

The DOCI system can be functionally broken down into 4 sub-systems: image acquisition unit, illumination unit, light filtration unit, and imaging unit. During the acquisition process, the target is illuminated by the pulsed fluorescence excitation light, after image focusing and optical filtration through the imaging unit and the light filtration unit, respectively, the image data of the fluorescence emission is recorded by the image acquisition unit.

3.1.1. Image Acquisition

The image acquisition unit is where optical signal is converted into electrical signal, it should have the ability for widefield, gated, and high-speed image acquisition. Candidate devices include charge-coupled device (CCD), scientific complementary metal-oxide-semiconductor (sCMOS) and single-photon avalanche diode (SPAD). The CCD image sensor consists of photodiode-potential well pairs, which form the elemental pixel of the sensor. Photoelectrons accumulate in each pixel when enabled, during readout all of the photoelectrons are relayed from one pixel to the next down each row, and converted into voltage serially into a buffer at the end of the relay. Each pixel of a sCMOS image sensor consists of a photodiode-amplifier pair, the conversion from photoelectron to voltage is done at each pixel, and the voltages are read out row-by-row to the buffer output. For SPAD, each pixel contains an avalanche photodiode (APD), each photon arriving on the sensing site excites an electron and the electron immediately excites multiple additional electrons and causes an avalanche current to develop, thus SPAD actually measures each photon that reaches the pixel. CCD provides high resolution, high quantum

efficiency (QE), and low noise level, but the speed of image acquisition is limited due to the way data is read out. sCMOS provides high image acquisition speed and high resolution, but has limited QE and noise level. SPAD has good frame rate, high QE, and low noise level, but it is still difficult to create a high-pixel-count SPAD sensor.

3.1.2. Illumination

The illumination unit is for the generation and collimation of pulsed fluorescence excitation light. As DOCI is a wide-field imaging technique, it requires the excitation light to uniformly illuminate on the entire imaging area, the uniformity refers to spatial uniformity of both intensity and temporal synchronization. High repetition rate is also important as it allows faster data acquisition. Light-emitting diode (LED) and laser both meet the requirements for uniformity and repetition rate. Laser light has higher repetition rate and is monochromatic, yet laser generates coherent light, the coherent light reflection generated inside the optical system can cause interference patterns developed in images. Light emitted from a LED has broader spectrum and lower temporal coherence, therefore is free from interference.

3.1.3. Light Filtration

The light filtration unit filters the fluorescence emission light that arrives at the image sensor. It serves two purposes, first is to select the emission band, previously we discussed, DOCI data from multiple spectral bands helps to improve the specificity. The second purpose is to block the excitation light, which could be reflected by the sample. In general, the excitation band and the emission band do not overlap, so the two purposes can be achieved at the same time with an optical filter, which is usually a band-pass filter or a long-pass filter (if the excitation light is in the ultraviolet (UV) range). For flexibility in spectral band selection, a liquid crystal tunable filter or

a motorized filter wheel holding a set of optical filters can be employed here. Liquid crystal tunable filter offers higher degrees of freedom for spectral band tuning, while motorized filter wheel is more affordable.

3.1.4. Imaging

The imaging unit focuses the image of the fluorescence emission from the target. The quality of the focus directly affects the DOCI image contrast, for spots with poor focus, the emitted fluorescence light will be recorded not only by the corresponding pixel, but also by other neighbor pixels, resulting in inaccurate DCOI value estimation. Different applications have different requirements for focusing, such as depth of field, aperture size and lens size, and the appropriate lens system needs to be selected according to the specific application. For imaging of processed samples with flat surface, such as tissue sections, the requirement for depth of filed is low, therefore camera lenses with large apertures and lens diameters are more suitable because they can collect more light. For microscopic imaging that study microstructures, a microscope lens with suitable magnification should be used. For *in vivo* imaging, where the site of interest is usually not flat, smaller aperture is beneficial to ensure adequate depth of view, specialized clinical lens systems such as endoscopes should be chosen if it is unreachable for conventional camera lenses.

In terms of system implementation, the intensified charged-coupled device (iCCD) cameras are selected for image acquisition, because this kind of image sensor meets our needs for wide-field, high-speed, and high-sensitivity, and can perform well in low-light image acquisition conditions. Specifically, considering the outstanding features of sub-nanosecond gating precision, high repetition rate and high quantum efficiency, the Andor iStar CCD series cameras are used in our DOCI systems. The development of our system is carried out around this series of cameras. Among the options for other 3 sub-systems discussed above, we chose to use ultraviolet light-

emitting diodes (UV-LEDs) to generate excitation light, use motorized filter wheel and optical filter sets for light filtration, and use digital single-lens reflex (DSLR) camera lenses for target focusing.

3.2. Previous Implementation

The development of DOCI implementation can be divided into two generations based on the illumination unit used in the system. The first-generation systems were developed and tested between 2015 and 2018, featuring direct illumination from multiple UV-LEDs. The current research on the second-generation systems began in 2019, the illumination light is generated by a single high-power UV-LED and coupled to the output by a liquid light guide. Figure 3.1 shows the system diagram of the first-generation DOCI system [44], a group of UV-LEDs are placed in front the system to provide pulsed UV excitation, a DSLR camera lens is used for focusing, a motorized filter wheel is used for optical filtration.

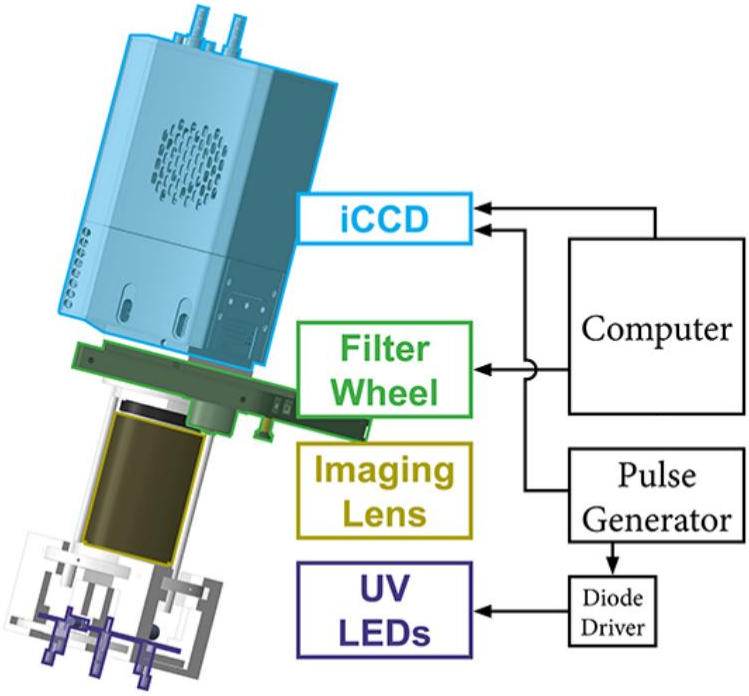

Figure 3.1 First-generation DOCI system diagram [44].

Figure 3.2 shows the multiple iterations of the first-generation DOCI system that was developed from 2015 to 2018. After the pre-DOCI FLIM system, DOCI 1.0 was the first rapid-prototyped system for *in vivo* imaging, yet it was noticed the transportation and operation of the system was very difficult. DOCI 2.0 was designed to address the logistical problems with transportation and system operations from DOCI 1.0, improvements include putting the system on a custom cart with large air cushioned tread wheels and mounting the imaging module onto a flexible robotic arm. DOCI 3.0 was designed to primarily improve the ergonomics and illumination, including the incorporation of a custom designed LED circuit board and a robotic arm with longer reach and higher weight limit.

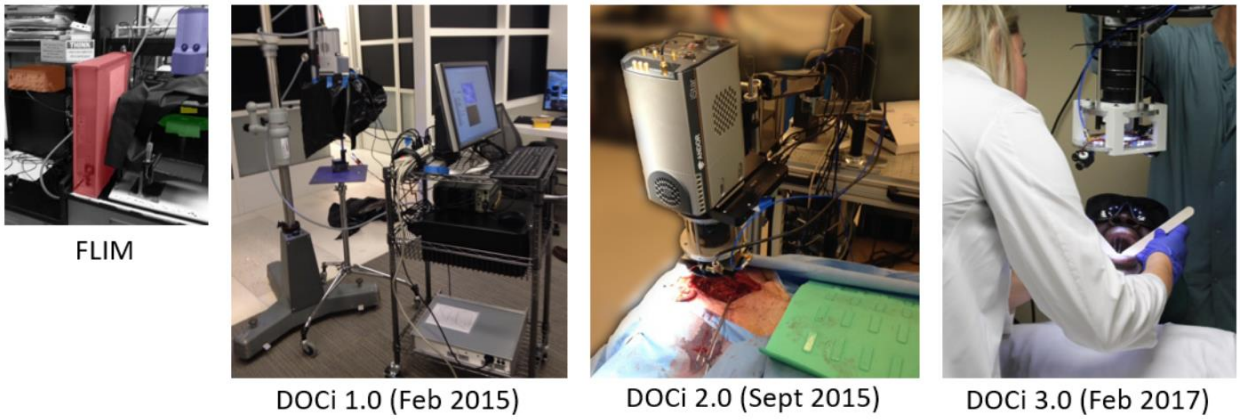

Figure 3.2 Different iterations of the first-generation DOCI system implementation [44].

Three Andor USB iStar series cameras DH734 Gen 2 (W-AGT, -03), 334T Gen 3-FL (VIH, -73) and 334T Gen 3-FL (EV3, -A3) were used on DOCI 1.0, 2.0 and 3.0, respectively. The Andor 334T Gen 3-FL (EV3, -A3) has the best overall performance for DOCI applications considering its repetition rate (500 kHz), temporal resolution (<2 ns) and quantum efficiency (> 40% in 280 - 810 nm).

The illumination unit is a custom-designed LED driver board with 6 UV-LEDs (LED370E, Thorlabs) mounted on it, each LED has an optical power of 2.5 mW. The circuit board is mounted in front of the camera lens and at a proximity to the focal point of the imaging system, so the target can get maximum illumination. The last iteration of this design has the system mounted on a custom-built wheeled cart through a monitor arm, allowing the system to be freely moved around and used for *in vivo* measurement. During validation and testing, it was found that although putting the LEDs close to the focal points seems to grant a high light utilization, but the diodes have a round clear epoxy casing, which results in a wide beam angle, thus actually reduces the light utilization. The bulky supporting structure that is used to mount the circuit board makes it more challenging to focus the system onto the target position in tight spaces. In addition, since the LEDs

are driven in a pulsed manner with low duty cycle, the actual light intensity is far lower than the LEDs' nominal optical power.

Three different camera lenses were evaluated: Canon MP-E 65mm f/2.8 1-5X Macro, Canon EF-S 18-55mm f/3.5-5.6 IS II, and Canon EF-S 55-250mm F4-5.6 IS. The most important metric for lens comparison is the depth of field (DOF): the distance between the closest and farthest objects that appears acceptably sharp. For clinical experiments, the target of imaging could have a very uneven surface, it requires the imaging unit to have enough DOF to have good sharpness. However, increasing the DOF comes at the cost of reducing the aperture, which reduces the amount of light passing through the lens, and as a result decreases the image resolution and signal-to-noise ratio (SNR). Another important factor is the working distance, with the UV-LEDs placed in front of the lens, the lens should maintain a suitable working distance so that the diodes don't hit the target. The comprehensive comparison showed the Canon EF-S 55-250mm F4-5.6 IS lens best suits the system.

3.3. Current Implementation

Compared with the first-generation system, the development of the second-generation system seeks to improve from three aspects: (a) Access to more possible surgical sites in head and neck surgery; (b) Imaging quality improvement; (c) System user-friendly improvement. The first two aspects are mainly at the hardware design level, and the third is mainly at the software design level. Overall, the purpose is to make the system work more efficiently in *in vivo* head and neck surgical scenarios.

After we evaluated the first-generation system in both *ex vivo* and *in vivo* tasks, we noticed the system can only be used in limited *in vivo* head and neck surgery scenarios. The use of the camera lens and the front-mount LED circuit board can effectively access most surgical sites on

the body surface, but because of the size of the circuit board and its mounting frame, it is very difficult to reach surgical sites in the oral cavity, and nearly impossible to reach oropharyngeal sites. To reach those geographically difficult sites, the size of the components should be appropriately reduced. For access to oropharyngeal sites, the conventional camera lens should be replaced with endoscopic optics, as it requires access to a deeper and narrower cavity.

The illumination units design affects both the system flexibility and the imaging quality. As mentioned earlier, the front-mount LED driver board and its supporting structure have a cross-sectional area that is larger than most surgical sites in head and neck surgery, let alone reaching into the oropharynx. However, it is already very hard to shrink the circuit area while having 6 LEDs onboard, reducing the number of the LEDs would devastate the illumination uniformity.

The workaround is to remove the LED driver board from the front end of the imaging unit and mount it on the system cart, then use a light guide system to direct the generated light to the target surface. Thus, only the light outlet with much smaller size is placed in front of or next to the imaging unit. The relocation of the LED driver board also reduces the size constraints on the circuit design, making it possible to further improve circuit performance. On the other hand, UV-LEDs with higher power and better temporal response have become available in recent years, making it possible to reduce the number of LEDs but still have the same illumination density and better illumination uniformity. Overall, lower circuit size constraints and a reduction in the number of diodes on the board facilitate circuit design for higher performance.

3.3.1. Upgraded Single-LED Board

Figure 3.3 shows the upgraded single-LED board designed and manufactured by the Physics & Astronomy Electronics Shop at UCLA. The board has a dimension of 178 mm * 99 mm * 23 mm, a 24 V power supply is used to power the circuit, a pulse signal with 2 V offset, 4 V

amplitude is used to synchronize the LED emission through a SMA trigger input. The light emitted from the LED can be coupled into light transmission guides such as a liquid light guide cable, as is shown in Figure 3.4. The guide is aligned with the LED and the two are very close. The LED has a dome shaped epoxy lens with a diameter of 3 mm, the guide has a core diameter of 5 mm, the cable can efficiently collect the light emitted by the LED. In addition to higher optical power, the custom board is also fine tuned to have fast optical falling edge and accurately synchronized output, which guarantees the consistency of data measurement.

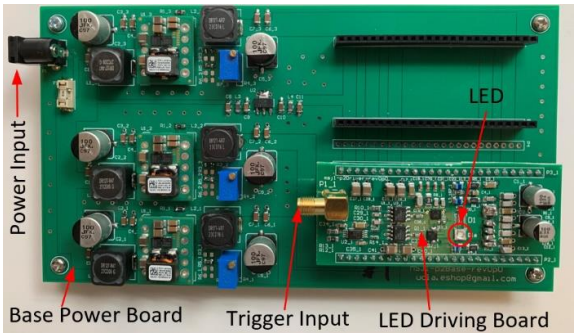

Figure 3.3 Custom LED board manufactured for increased light intensity with robust pulse shape.

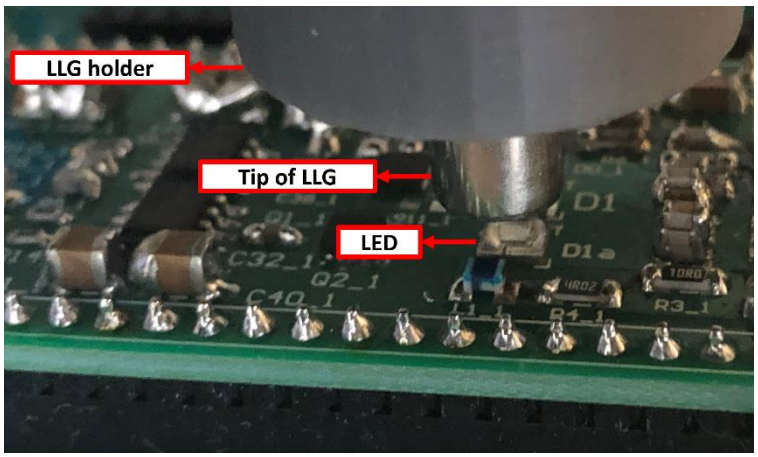

Figure 3.4 Light coupling between the LED and the LLG. A LLG holder is 3D printed to hold the LLG in place. LLG: liquid light guide.

3.3.2. Iterations of System Implementation

Figure 3.5 shows the 3 iterations of the second-generation DOCI system that has been developed. The main differences between the 3 iterations are how the UV excitation light is coupled to the sample and how the imaging unit is constructed. The first iteration (Figure 3.5 (a)) is an *ex vivo* system with camera lens and 45° incident illumination. The second iteration (Figure 3.5 (b)) is an *in vivo* camera lens system with 90° incident illumination. The third iteration (Figure 3.5 (c)) is an *in vivo* system with endoscope and imaging fiber bundle. The *in vivo* systems also have the capability to do *ex vivo* imaging.

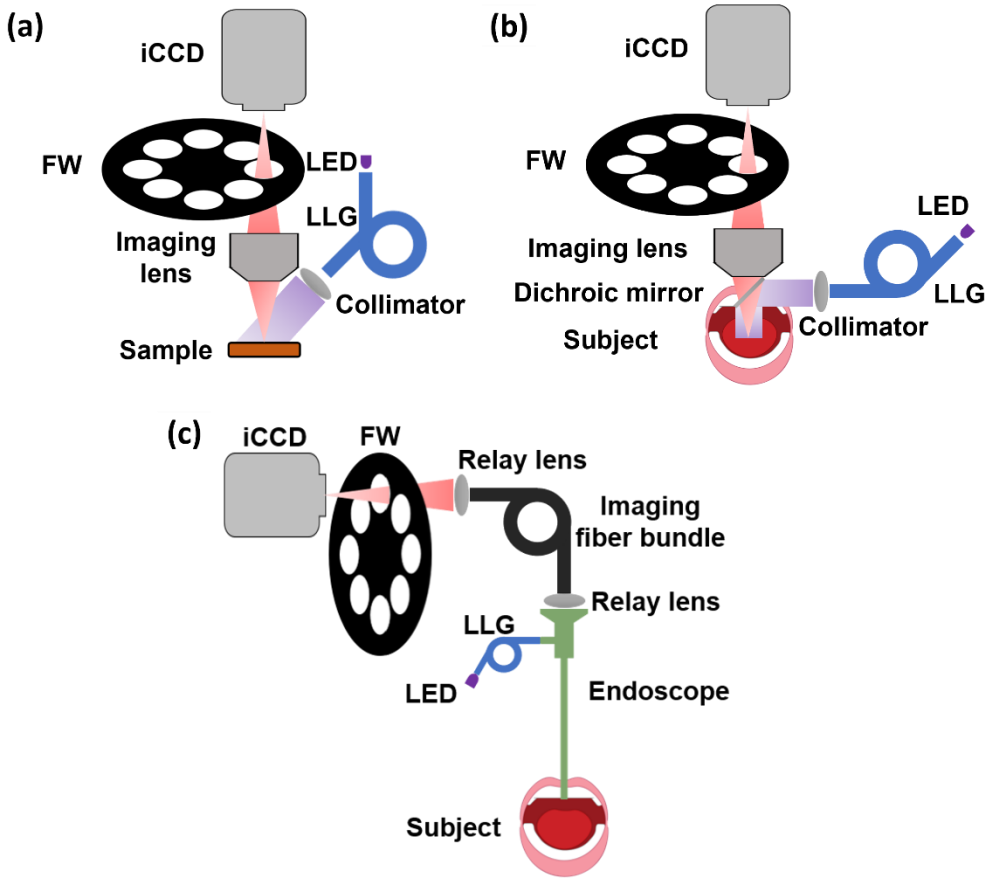

Figure 3.5 Different versions of the second-generation DOCI system. (a) *Ex vivo* system with camera lens and 45° incident illumination; (b) *In vivo* system with camera lens and 90° incident illumination; (c) *In vivo* system with endoscope and imaging fiber bundle. LLG: liquid light guide.

3.3.2.1. *Ex Vivo* System with Camera Lens and 45° Incident Illumination

The system diagram and implementation of the first iteration system are shown in Figure 3.5 (a) and Figure 3.6, this version was developed for system verification and used only for *ex vivo* experiments. The illumination unit contains one single-LED board (Figure 3.3), one liquid light guide (LLG) cable of 1.2 m length (LLG5-4T, Thorlabs), one 365 nm bandpass filter (Hg01-365-25, Semrock) and a collimating lens (ACL25416U-A, Thorlabs). The collimator lens directs the excitation light to the sample with a 45° incident angle to reduce potential reflection to the camera from the illumination. A Canon EF 50mm f/2.5 Compact Macro lens was used for system characterization then it was replaced by a Canon EF 50mm f/1.2L USM lens for *ex vivo* imaging for higher resolution and light intensity. A 10-slot motorized filter wheel (X-FWR-E, Zaber) is used to hold one 405 nm long-pass filter (LPF) (BLP01-405R-25, Semrock) and 8 band-pass filters (BPF) with center wavelength/FWHM of: 415/10 nm (FF01-415/10-25, Semrock), 434/17 nm (FF01-434/17-25, Semrock), 465/30 nm (FF01-465/30-25, Semrock), 494/20 nm (FF01-494/20-25, Semrock), 520/15 nm (FF01-520/15-25, Semrock), 542/27 nm (FF01-542/27-25, Semrock), 572/28 nm (FF01-572/28-25, Semrock), and 605/15 nm (FF01-605/15-25, Semrock). Figure 3.7 shows the spectra of all the optical filters in wavelength range between 300 to 600 nm.

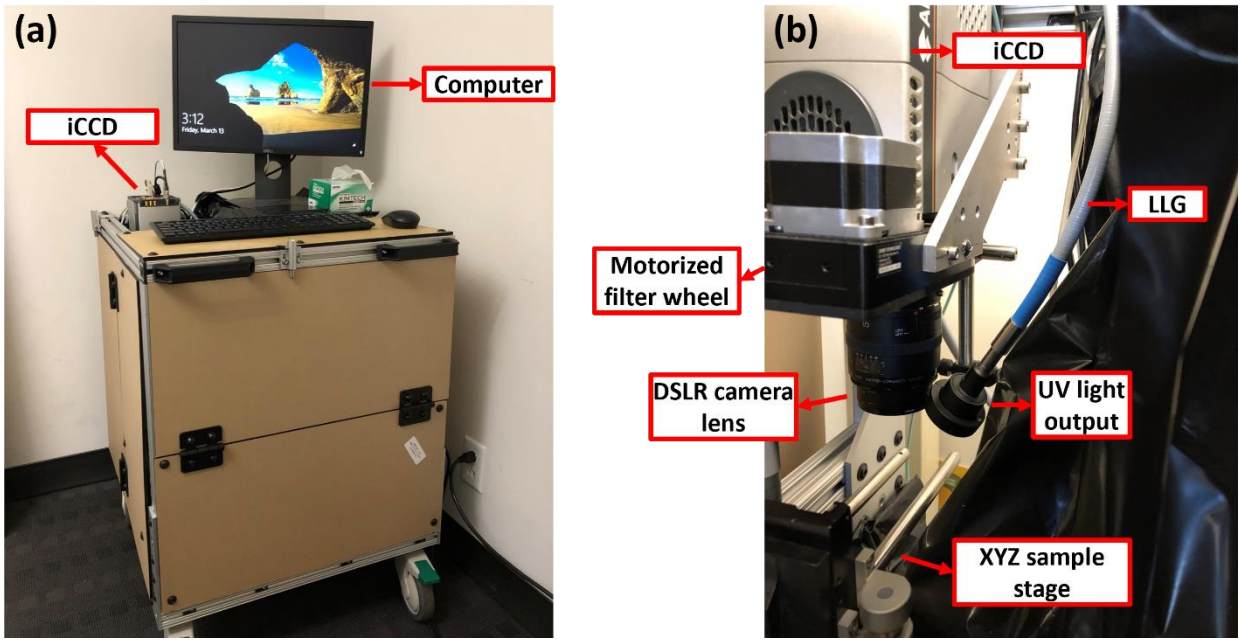

Figure 3.6 *Ex vivo* system with camera lens and 45° incident illumination. (a) System cart; (b) Interior part of the system cart. LLG: liquid light guide.

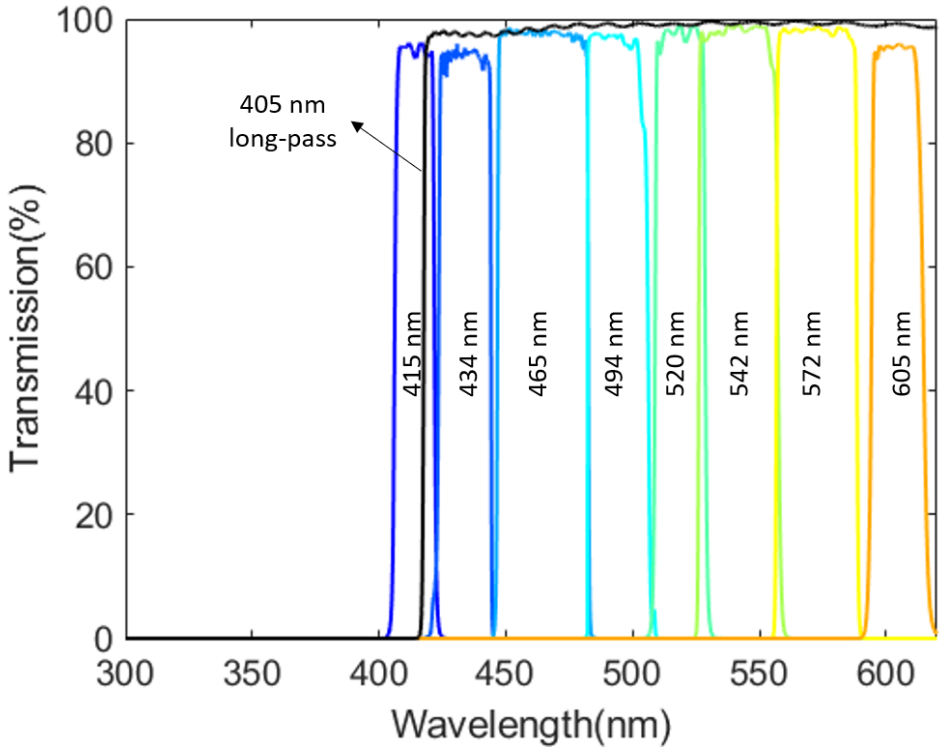

Figure 3.7 Spectra of optical filters used in the system.

3.3.2.2. *In Vivo* System with Camera Lens and 90° Incident Illumination

The system diagram and implementation of the second iteration system are shown in Figure 3.5 (b) and Figure 3.8, this system is an *in vivo* camera lens system with 90° incident illumination. The previous 45° incident illumination design was found to be unsuitable for *in vivo* measurements, because the natural geographical profile of the target site could cause some captured areas to be unlit. To have even illumination on the target, the illumination beam is concentric to the camera lens. Compared with the 45° incident illumination unit, the 90° incident illumination unit employs a dichroic mirror (FF389-Di01-25x36x1.5, Semrock) to reflect the UV light onto the target, and the emission light reaches the sensor after passing through the mirror.

As is shown in Figure 3.8 (a), the LED driver circuit board is mounted on top of the cart, unlike in the first iteration it is mounted inside the cart, because mounting the board on top of the cart puts less stress on the LLG. For UV exposure safety consideration, a 3D printed enclosure is used to encapsulate the circuit board and protect users' eyes from direct UV exposure. A cooling fan is installed on the enclosure to cool the circuit, cooling the circuit helps prevent radiant flux from decreasing due to increased LED temperature, and prevent circuit components from burnt out due to overheating.

A monitor arm (M8, Humanscale) was integrated to allow for 3-axis movement of the system, and a rotation stage (481-A, Newport) was mounted vertically to allow angular orientation. To commute between the laboratory and the operating room, the system is placed on a custom mobile cart. An uninterruptible power supply (UPS) (APC Smart-UPS 1500VA) was onboard to protect the instruments and power the system for half an hour while unplugged. A Canon EF-S 55-250mm F4-5.6 IS lens was used for imaging, as it has higher depth-of-view than the Canon EF 50mm f/1.2L USM lens used in the first iteration. Compared with the first-generation *in vivo*

system, the illumination light of this system is better in intensity, uniformity and pulse profile, and the operation of the system is also simpler.

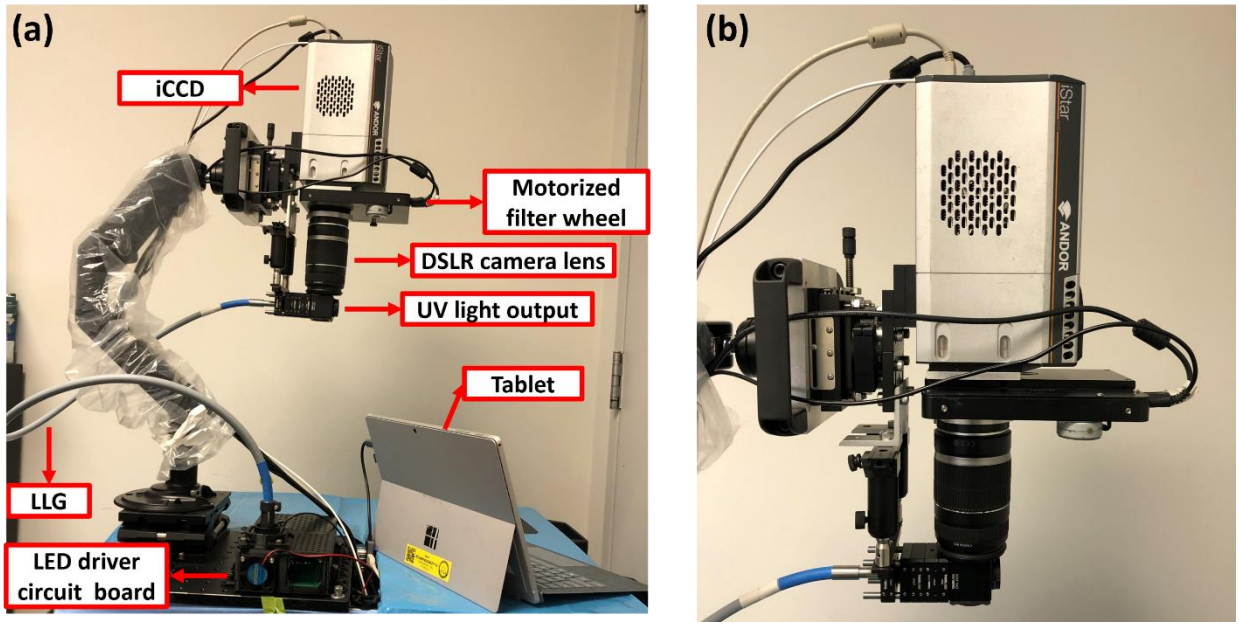

Figure 3.8 *In vivo* camera lens system with 90° incident illumination. (a) The system is assembled on a mobile cart, in addition to the parts shown in the image, the UPS and the waveform generator are installed inside the cart; (b) Zoomed in image of the components mounted on the robotic arm. LLG: liquid light guide.

3.3.2.3. *In Vivo* System with Endoscope and Imaging Fiber Bundle

Figure 3.5 (c) shows the system diagram of the *in vivo* system with endoscope and imaging fiber bundle. The change is mainly in the imaging unit, an endoscope, an imaging fiber bundle (0719113, SCHOTT) and two collimating lenses form the imaging unit instead of a single camera lens. We evaluated two endoscope products, Stryker 502-485-010 with 5 mm core diameter and KARL STORZ 26003AA with 10 mm core diameter, larger core diameter has better image quality, but make it harder to position the endoscope in narrow cavities. We also evaluated two strategies for coupling the UV light to the endoscope tip, using external UV transmission fibers, as is shown in Figure 3.9, and using the internal fiber optics of the endoscope. The UV transmission fiber is

superior to the endoscope internal fiber in terms of transmission performance, but the overall output intensity is lower because the prototype bundle that we used has only 7 fibers, thus it was not able to collect all light generated from the LED.

Therefore, for evaluation on tissue samples, we used a KARL STORZ 26003AA endoscope and used its internal fiber optics for UV transmission. The endoscope is also a part of the illumination unit, it has fiber optic light transmission incorporated with a 5 mm input, which allows the 5 mm LLG to be directly connected to the endoscope. During the operation, the endoscope is first detached from the system, moved to the desired position and fixed with a rigid robotic holder. Then the imaging fiber bundle is connected to the endoscope through a quick-release adapter and the acquisition starts. The imaging unit and the illumination unit both suffer from low light transmission because of the fiber optics in the endoscope and the image guide cable, and the small aperture of the endoscope.

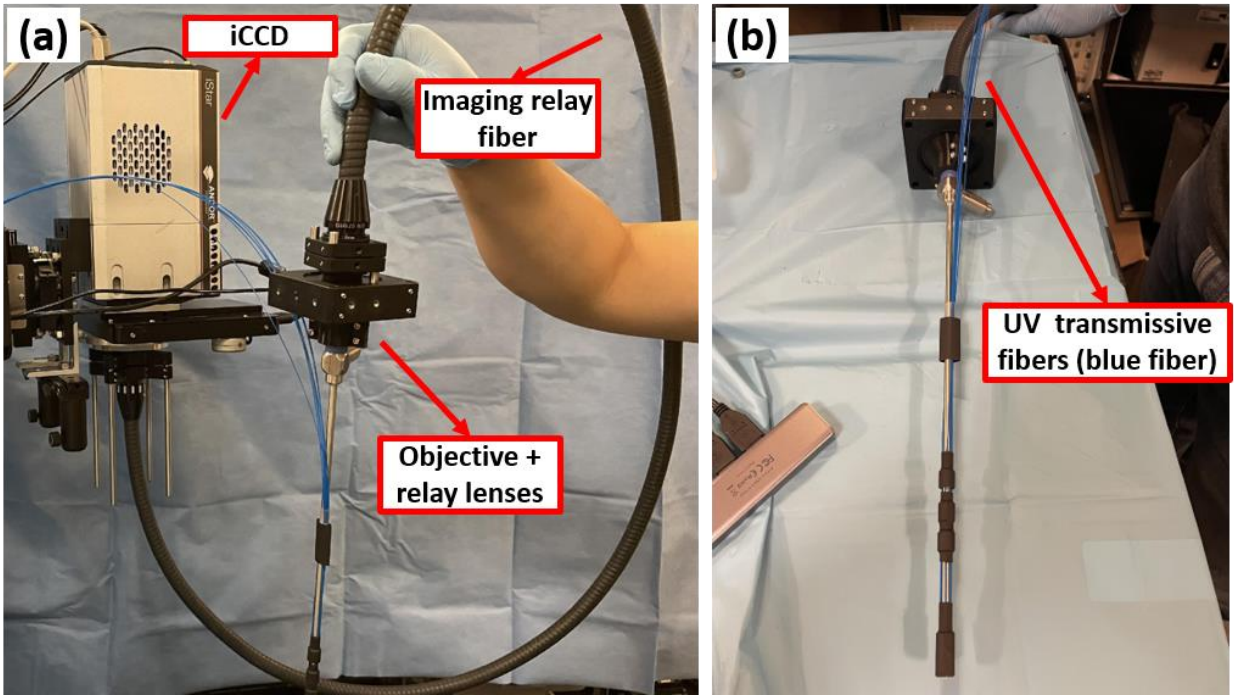

Figure 3.9 *In vivo* system with endoscope and imaging fiber bundle.

3.4. System Control

3.4.1. Control Software

As is shown in Figure 3.1, a computer is used to synchronize and control the iCCD and the filter wheel in the first-generation system, a software interface was developed in LABVIEW that automates most of the acquisition processes. In the second-generation system, system control is further integrated into the computer: after powered on, all instruments can be controlled on a computer through a customized program with a graphical user interface (GUI). The program is developed based on the MATLAB platform in the form of a MATLAB GUIDE app, we migrated from LABVIEW to MATLAB because MATLAB provides the easy-to-use environment with a variety of integrated toolboxes, such as app design, instrument control, and image analysis, which facilitates the fast iteration of our program.

Figure 3.10 shows the layout of the GUI, different functional blocks are highlighted in red boxes. There are primarily 3 types of blocks: (1) Instrument connection and monitoring. iCCD, motorized filter wheel, and waveform generator can be controlled through the GUI. Two important values that indicate the system running status, i.e., iCCD temperature and LED runtime, are displayed in the GUI in real time. (2) Regular video display for target alignment. The left-top window is dedicated for regular video and DOCI video display, video frame size can be changed according to preference for resolution and frame rate. (3) DOCI data parameter configuration, acquisition, display, and output.

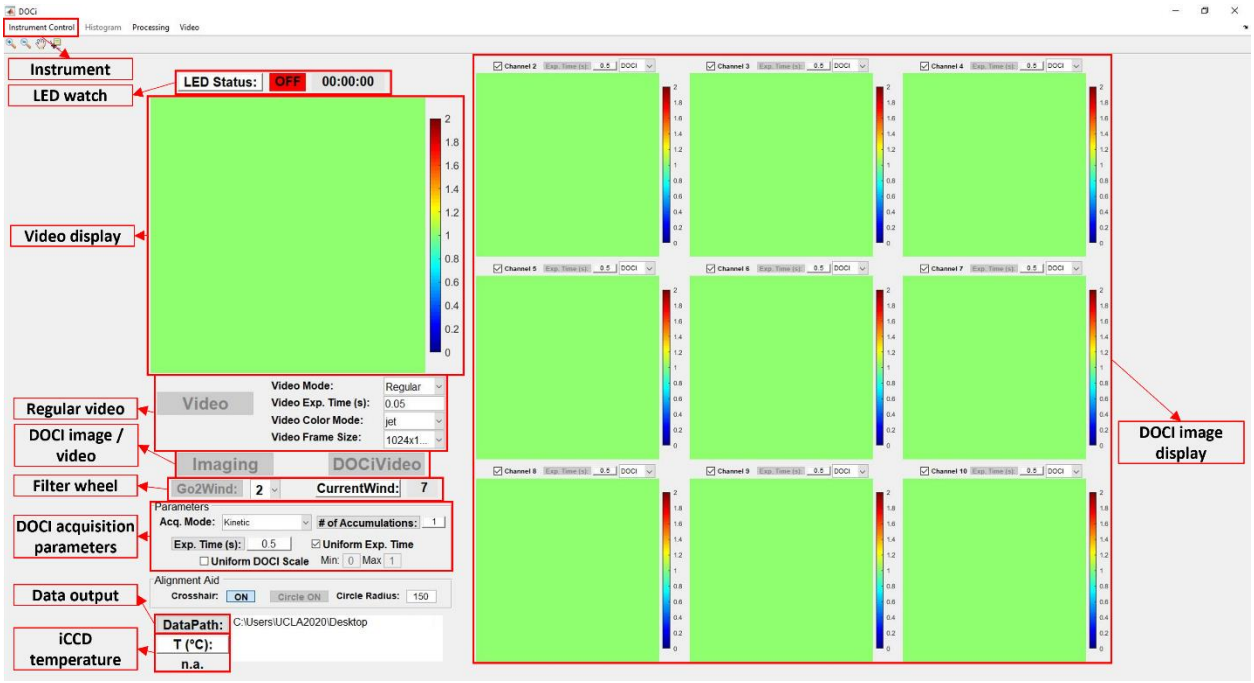

Figure 3.10 Graphical user interface developed in MATLAB for system control.

The acquisition mode, selected filter channels, number of accumulations, and exposure time for a single accumulation are the 4 parameters that can be configured through the GUI, more parameters are configurable through a table file which the program reads in during startup, as is shown in Figure 3.11. In the table file, rows 2 to 11 are universal parameters, rows 12 to 14 are parameters related to video frame acquisition, rows 15 and 16 are parameters related to RGB image acquisition, and rows 17 to 23 are parameters related to DOCI image acquisition.

1	ICCD Parameters		
2	HSSpeed	[0,0]	Horizontal shift speed
3	VSSpeed	1	Vertical shift speed
4	preAmpGain	2	Pre-amplifier gain
5	XPixels	1024	Number of horizontal pixels
6	YPixels	1024	Number of vertical pixels
7	DDGInsertionDelay	1	DDG insertion delay
8	DDGOpticalWidthEnabled	1	DDG optical width enable
9	triggerLevel	1.5	Trigger voltage threshold (V)
10	triggerInvert	0	Trigger edge (0 - rising, 1- falling)
11	externalTriggerTermination	0	Trigger termination (0 - 50Ω, 1 - high z)
12	videoMode	0	iCCD mode for regular video acquisition
13	videoExpTime	0.05	Exposure time (s) for regular video acquisition
14	videoGain	500	Gain for regular video acquisition
15	RGBExpTime	0.1	Exposure time for RGB image acquisition
16	RGBGain	500	Gain for RGB image acquisition
17	expTime	[.5,.5,.5,.5,.5,.5,.5,.5,.5,.5]	Exposure times (s) for DOCI image acquisition
18	DOCIWinWidth	3.00E+04	DOCI window width (ps)
19	DOCIFilterGain	[500, 500, 500, 500, 500, 500, 500, 500, 500, 500]	Gains for DOCI image acquisition
20	DOCIVideoGain	500	Gain for DOCI video acquisition
21	DOCIWinDelay	[134e3, 164e3, 300e3]	Delay (ps) series for 3 windows
22	AcquisitionMode	Kinetic	Default DOCI acquisition mode
23	NAccumulation	1	Default number of accumulations

Figure 3.11 During program startup, a 2-column table file is loaded for system parameter configuration. The explanation of each row is given in the red-lined table on the right. DDG: digital delay generator.

Figure 3.12 shows the workflow behind the control software. After the program is started, it first loads software configuration and parameters from the external file. After the user manually connects the devices in the software, the software would wait until all the devices are ready. To start a data acquisition, the user first turns on the regular video and manually move the sample or the camera into focus. As the user manually start imaging, the software iterates through all filter windows to perform data acquisition, image display, and data exportation.

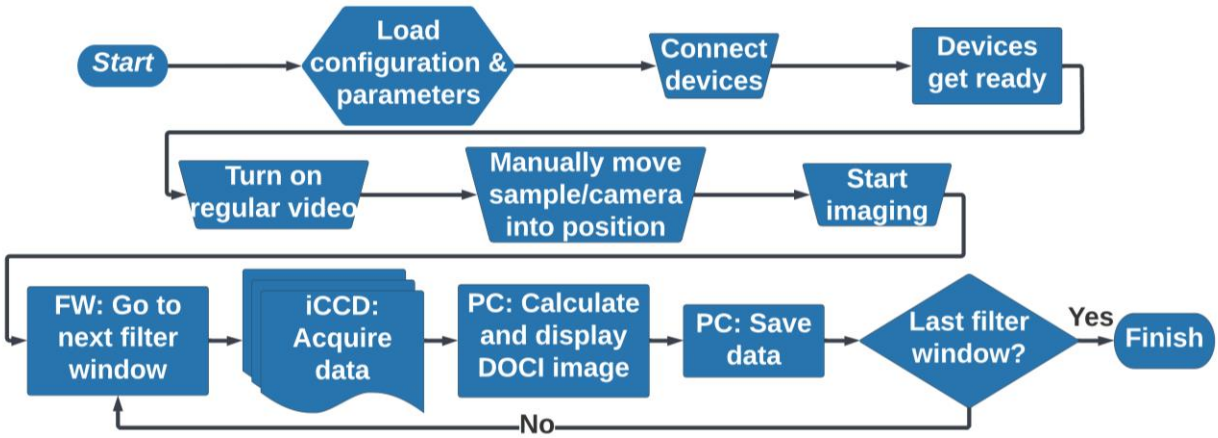

Figure 3.12 DOCI system control software workflow.

There are 4 acquisition modes: Single Scan, Single Accumulate, Kinetic, and Kinetic Accumulate. The difference between each of them is the mode the iCCD is configured to acquire data. For DOCI Single Scan mode, the iCCD works in Single Scan mode (Figure 3.13 (a)), only one image is acquired without accumulation for each acquisition, 3 iCCD acquisitions are performed for one DOCI acquisition. For DOCI Single Accumulate mode, the iCCD works in Accumulated mode (Figure 3.13 (b)), the only difference to DOCI single scan mode is that accumulations are allowed. For DOCI Kinetic mode, the iCCD works in Kinetic Series mode (Figure 3.13 (c)), 3 delay values are passed to the iCCD at the same time, and the iCCD acquires the 3 images in one acquisition run, for more than one accumulations, the iCCD performs acquisition for each accumulation, the image data is transferred to and accumulated on the computer. The iCCD works in Accumulated Kinetic Series mode (Figure 3.13 (d)) when DOCI Kinetic Accumulate mode is chosen, the camera acquires the accumulation for each window individually, and the accumulation is performed on the camera, in this mode one DOCI acquisition involves one iCCD acquisition.

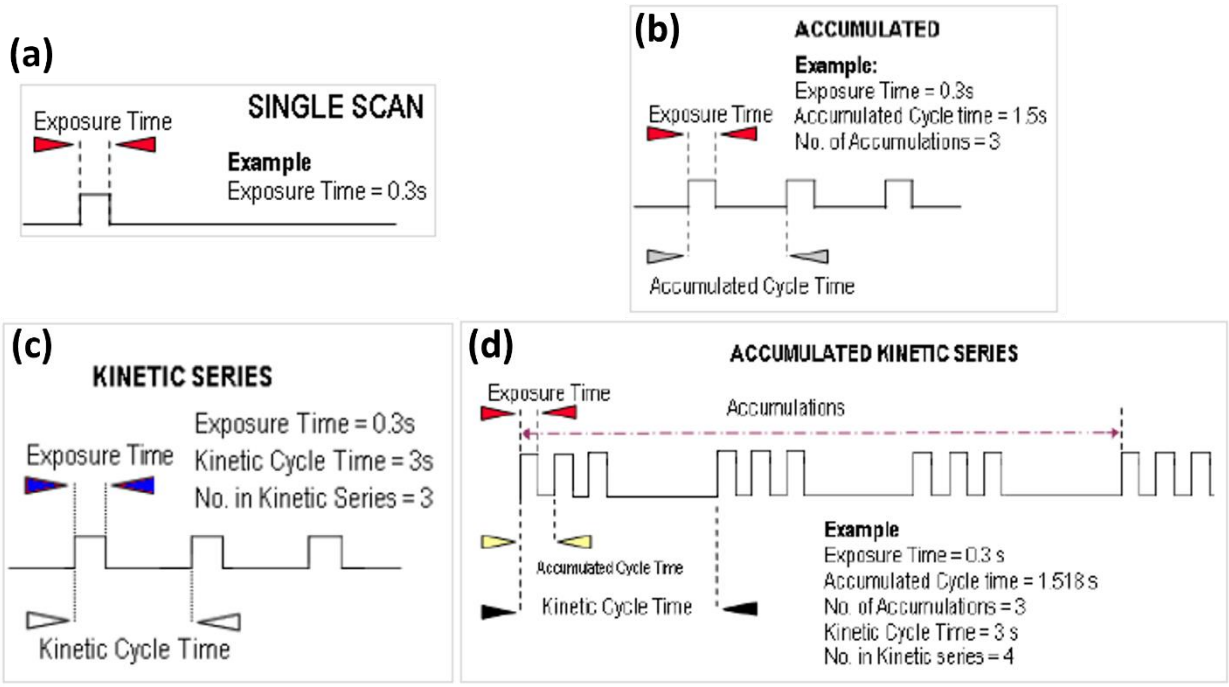

Figure 3.13 Acquisition modes of the iCCD. (a) Single scan. (b) Accumulated. (c) Kinetic Series. (d) Accumulated Sinetic Series. [45]

By default, DOCI image is displayed on the screen with the jet colormap (Figure 3.14), with minimum assigned to RGB triplets [0 0 1] and maximum assigned to RGB triplets [1 0 0]. It features strong contrast between two ends in the value range, yet for values in the middle, it might be difficult to tell the difference from the color. The program supports manual setting the limits of the colormap, it also can automatically set the limits by calculating a pair of low and high values from the image, the processing flow is shown in Figure 3.15. The flow helps to display tissue contrast for conditions where the target tissue type has a value that is in one end of the value range throughout the image. Manually adjusting the limits based on the calculated limits may be necessary to further enhance the tissue contrast.

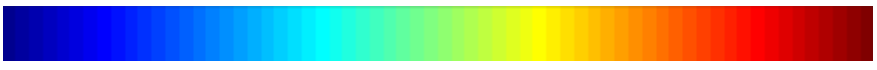

Figure 3.14 MATLAB jet colormap

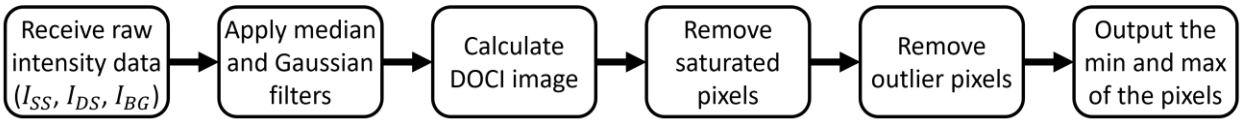

Figure 3.15 Processing flow for colormap limits calculation.

The purpose of developing this software is to simplify the operation of the user. The user does not need to have specific knowledge about the instruments, only need to maneuver the system into the position, click a couple of buttons in the GUI and wait for the acquisition to finish. The control program is fully configurable, so system parameters can be easily changed without touching the code. After the acquired raw data is received by the computer, the computer will save it in the form of image files, and at the same time display the DOCI images generated according to it in the GUI.

3.4.2. DOCI Data Acquisition

A complete data acquisition of DOCI includes the collection of 3 images I_{SS}, I_{DS} and I_{BG}. Using the iCCD, the 3 images are acquired one-by-one on the time scale (Figure 3.16). Figure 3.17 shows the example waveforms during a single round of DOCI data acquisition. Parameters such as iCCD exposure time, trigger pulse width and repetition rate, window width, and window delays are set only for demonstration purpose. Fire is the reference signal for beginning and end of individual iCCD exposure, the fire signal on high level indicates the iCCD is acquiring data of one image, the low-level areas between two high-level areas represent the iCCD is in the read-out and clean cycles. Trigger is the input trigger that synchronizes the CCD and the LED. Gate monitor is the exact photocathode on/off switching and timings, the gate monitor signal in Figure 3.16 poorly captured the real waveform because of the sampling rate. Figure 3.18, Figure 3.19, and Figure 3.20 are the magnified views of the acquisition of the 3 images in a single trigger pulse cycle. A negative

gate monitor spike indicates the photocathode is turned on, while a positive monitor spike indicates the photocathode is turned off.

Figure 3.16 DOCI data acquisition flow.

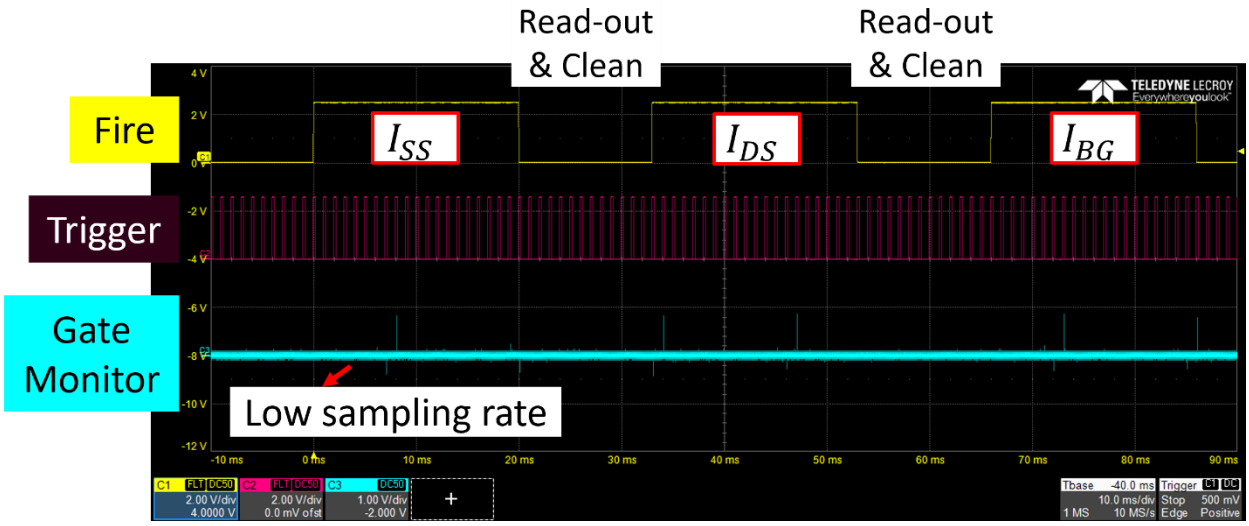

Figure 3.17 Example waveforms during a single round of DOCI data acquisition.

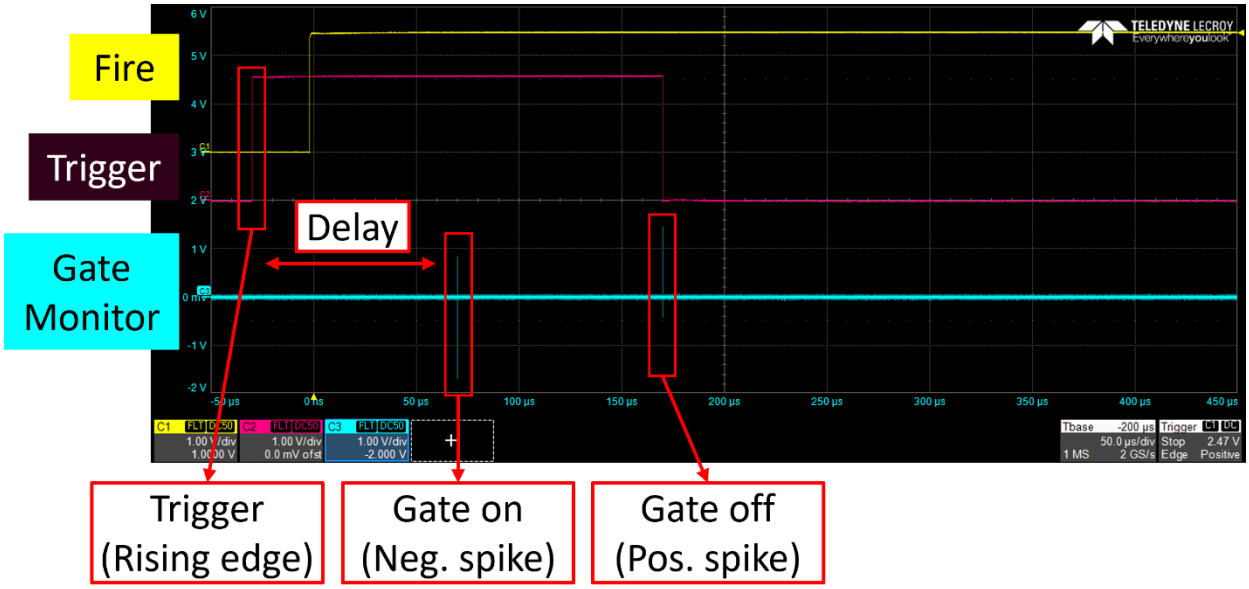

Figure 3.18 Example waveforms of the acquisition of I_{SS} in a single trigger pulse cycle.

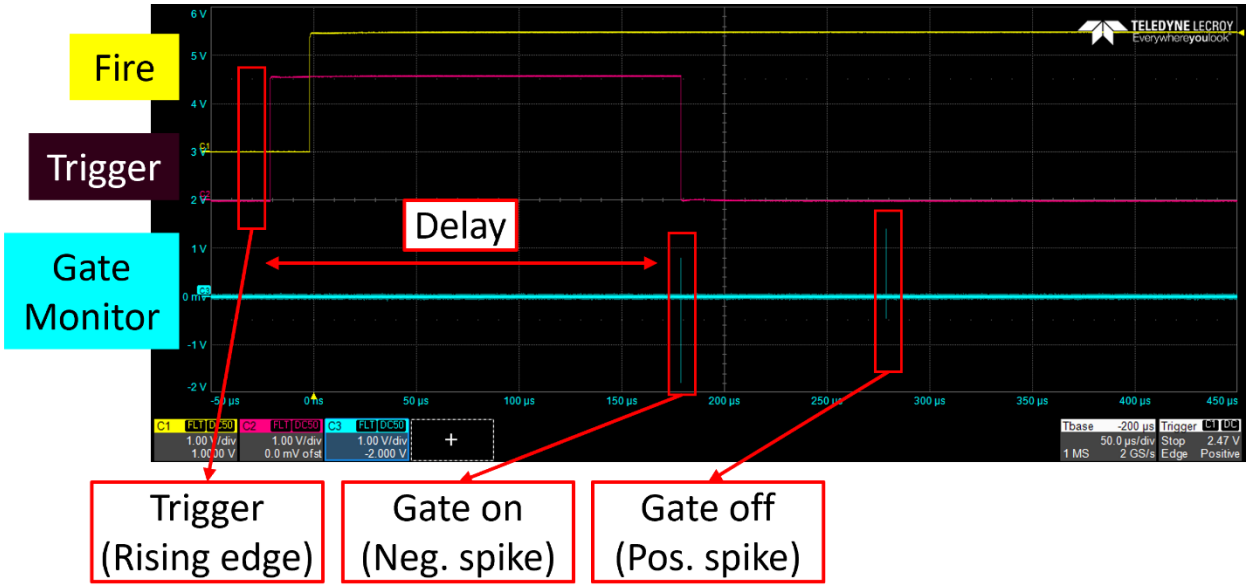

Figure 3.19 Example waveforms of the acquisition of I_{DS} in a single trigger pulse cycle.

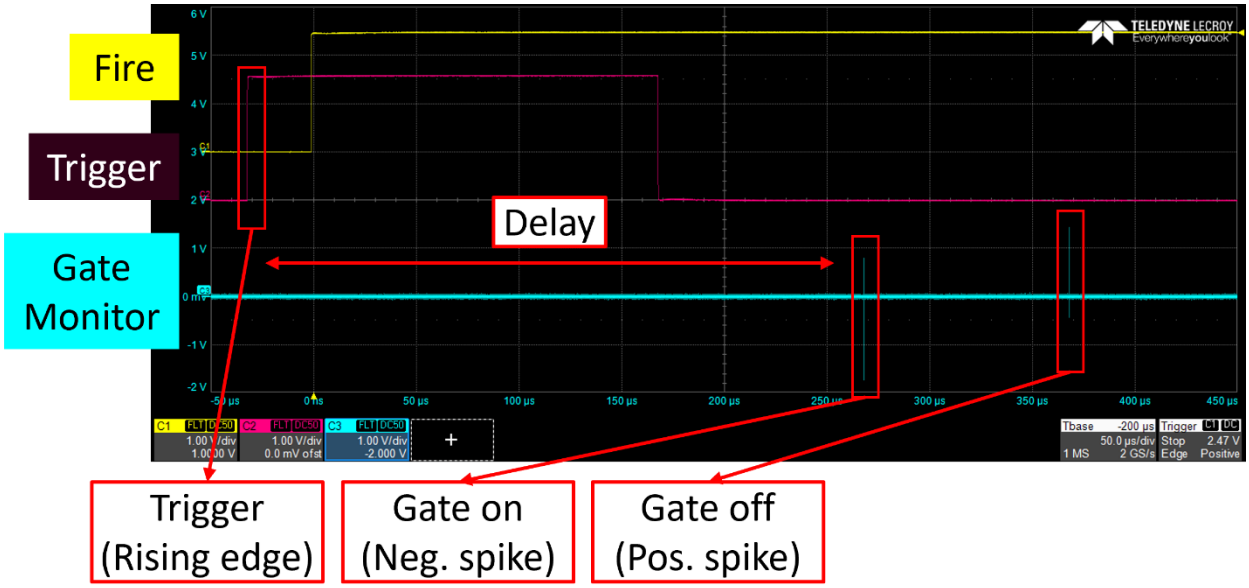

Figure 3.20 Example waveforms of the acquisition of I_{BG} in a single trigger pulse cycle.

3.5. System Characterization

3.5.1. UV Excitation Light Characterization

Unlike the light from a laser that is coherent and monochromatic, the light from a LED is incoherent and has a Gaussian-like distribution of wavelengths. Figure 3.21 (a) shows the UV-LED emission spectrum measured using a CCD spectrometer (CCS200, Thorlabs), the spectrum shows that the major peak of the LED emission has a broadband that extends to 430 nm and beyond, and it also has a broadband component in the visible range (490 nm to 640 nm). This component in the visible range can significantly bias our measurements because: (1) it overlaps with the spectral range we interested in (400 nm - 600 nm); (2) its ratio to the major peak intensity is greater than the quantum yield of most endogenous fluorophores, e.g., 0.019 for NADH [46] and 0.04 for FAD [47].

Therefore, we used a 365 nm BPF (Hg01-365-25, Semrock) to filter the UV-LED emission, and Figure 3.21 (b) shows the measured spectrum after filtration. The major peak now has a smaller

spectral width with a full width at half max (FWHM) of 14 nm, as a result its upper boundary is confined to below 400 nm. The visible range component is eliminated, which greatly improves the imaging quality.

We measured the optical power delivered onto the sample stage using the *ex vivo* system with camera lens and 45° incident illumination (Figure 3.5 (a)) and the *in vivo* system with camera lens and 90° incident illumination. With a repetition rate of 500 kHz and a pulse width of 80 ns, the pulsed light delivers an average of 4 W/m^2 and 4.8 W/m^2 power onto the sample, respectively. This power complies with NIOSH UV radiation exposure limits [48].

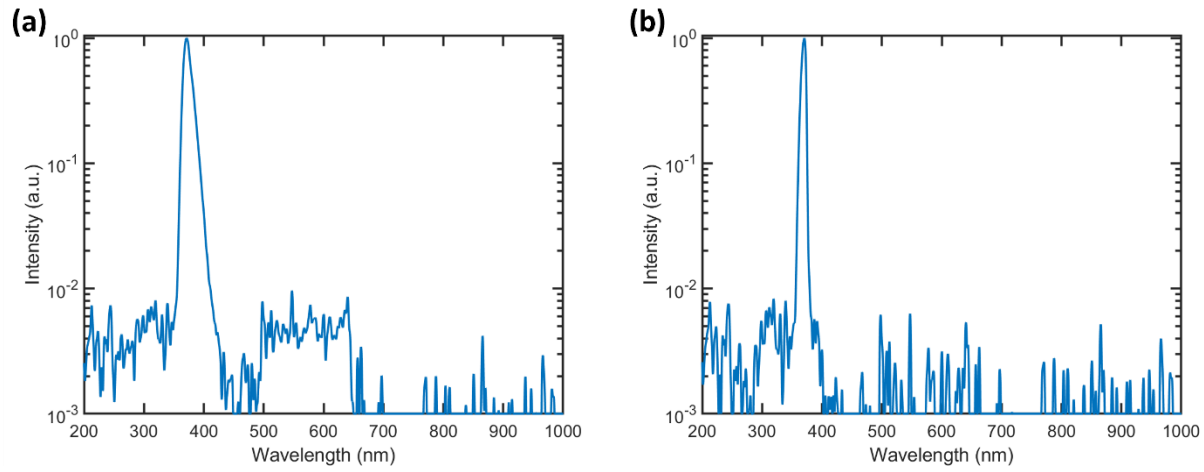

Figure 3.21 Spectra of: (a) the raw UV light; (b) filtered UV light with a 365 nm BPF

Figure 3.22 shows the optical pulse profile of the emitted UV light, the LED driver board was driven by a waveform generator outputting a pulse wave with a repetition rate of 500 kHz and a pulse width of 80 ns. The optical pulse profile was captured by the iCCD running in the kinetics scan mode: a series of 400 acquisitions were done, the step size (delay between two consecutive acquisitions) was 1 ns. The pulse profile has a two-step rising edge, it comes from the driver circuit design to ensure fast turn-on and turn-off for the LED. The pulse has a sharp and clean falling edge, the result of curve fitting to a single-exponential model shows the decay lifetime is 3.2 ns (adjusted

R^2: 0.9811). In the on-state area of the pulse, oscillations can be observed, the measured oscillation profile varies depending on different models of the iCCD.

According to the measured pulse profile, for the use in DOCI, the integration windows for the steady-state image (I_{SS}) and the decay-state image (I_{DS}) are placed back-to-back near the onset of the decay edge, and the integration window for the background image (I_{BG}) is placed at serval hundred nanoseconds away from the falling edge.

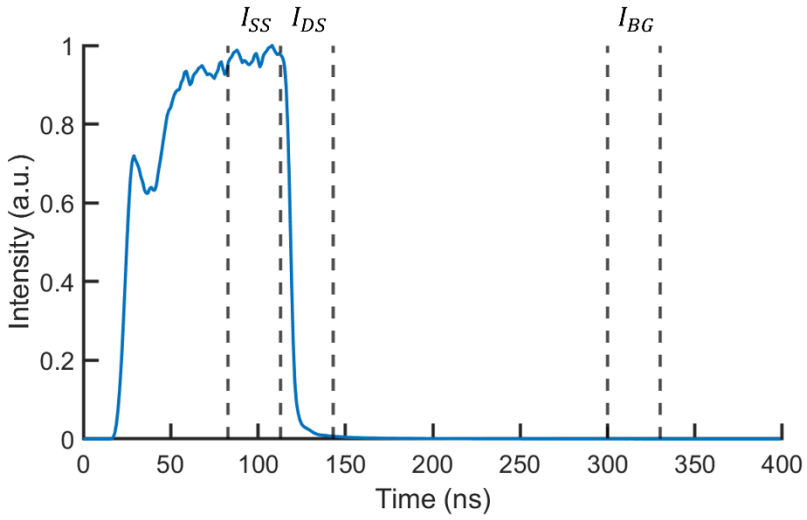

Figure 3.22 Pulse profile of the emitted UV light. Dashed lines indicate the integration windows for DOCI.

The kinetics scan mode of the iCCD was also employed to study the stability of the UV light pulse. Figure 3.23 shows the pulse profiles measured every 3 minutes from the moment the LED was turned on, a total of 60 pulse profiles were captured, covering a 3-hour time span. The pulse profiles are color-coded by the time the scan started relative to the time the LED was turned on. Over time, the UV pulse shifted in the direction of (1) smaller amplitude and (2) delayed rise and fall.

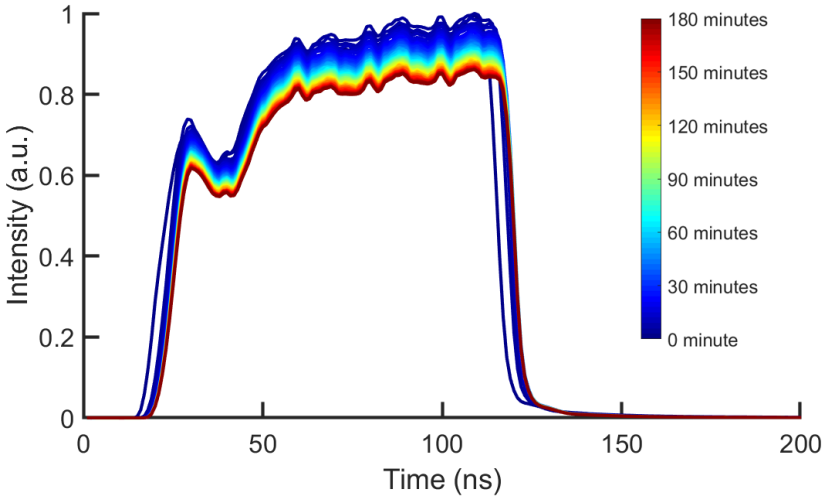

Figure 3.23 Optical pulse profiles measured at different times after turning on the LED

To determine the effect of pulse shifting on DOCI data measurement, a series of DOCI imaging on the UV-LED were acquired immediately after turning on the LED. The results are shown in Figure 3.24, a total of 720 measurements were acquired every 5 seconds for a total acquisition time of 1 hour. The medians of each image (DOCI, steady-state, decay-state, and background images) were used to plot the curves. In consistent with the results shown in Figure 3.22, with fixed integration window timings, the overall shift to the right resulted in a decrease in the steady-state intensity and an increase in the decay-state intensity, leading to an overall increase in the DOCI value. Although the steady-state intensity continued to drop, the corresponding DOCI value change gradually slowed down and almost stopped increasing after 20 minutes. After applied a cooling fan to reduce the LED temperature, the time for the system to reach stability reduced to 2 minutes and the LED temperature reduced from 90°C to 56°C (Figure 3.25).

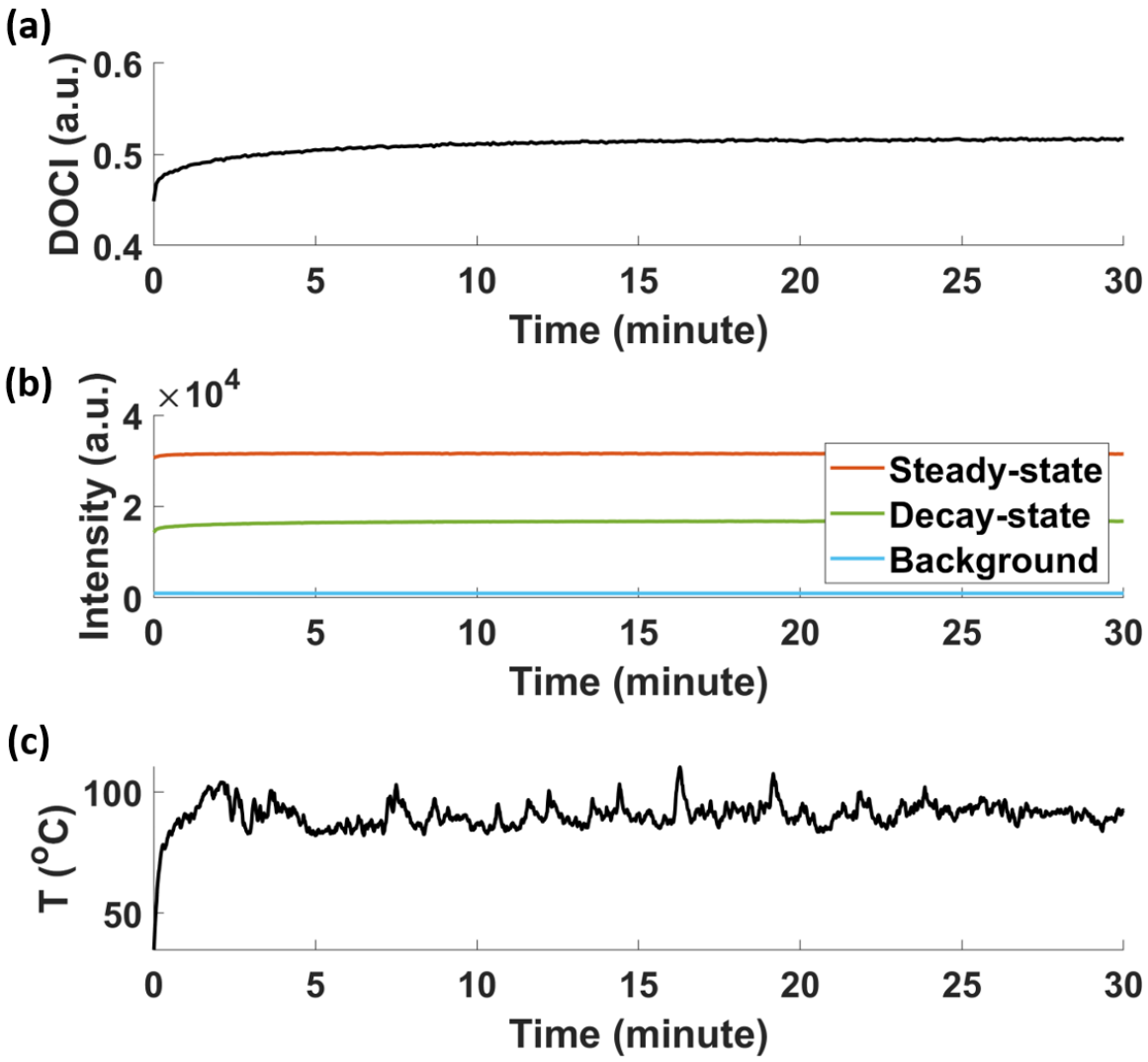

Figure 3.24 DOCI data measured at different times after turning on the LED, no cooling applied to the LED. X-axis: time of the measurement relative to the time the LED was turned on. Y-axis: (a) DOCI value; (b) steady-state, decay-state, and background intensities; (c) LED temperature.

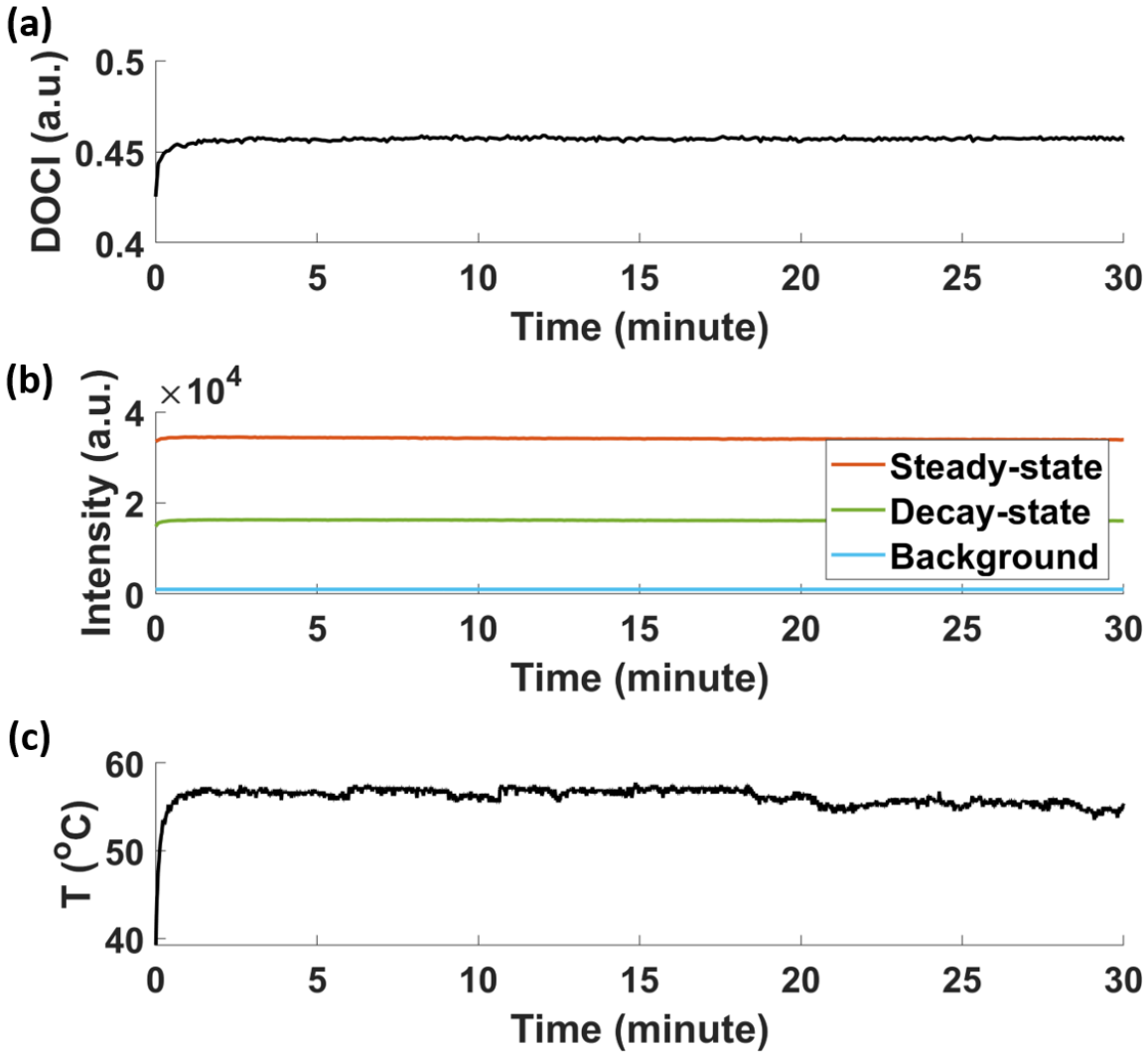

Figure 3.25 DOCI data measured at different times after turning on the LED, a 40 mm fan was used to cool down the LED. X-axis: time of the measurement relative to the time the LED was turned on. Y-axis: (a) DOCI value; (b) steady-state, decay-state, and background intensities; (c) LED temperature.

So far, we understand this UV light pulse shifting activity comes from the LED driver board, possibly related to the board trying to reach the stable working state after it starts pulsing. The detailed mechanism remains to be explored. This phenomenon does not affect us using the LED driver board in our system, as long as we always turn on the LED board at least 2 minutes before data acquisition.

3.5.2. Spatial and Temporal Resolutions

The *ex vivo* system with camera lens and 45° incident illumination (Figure 3.5 (a)) was used for system characterization of spatial and temporal resolutions. At a working distance of 50 mm, the implemented system has a 20 mm × 20 mm field of view and a 6 mm depth of field. The imaging result using a 1951 USAF resolution test chart (57-855, Edmund Optics) shows the system has a spatial resolution of 70 μm, the intensity and DOCI images are given in Figure 3.26.

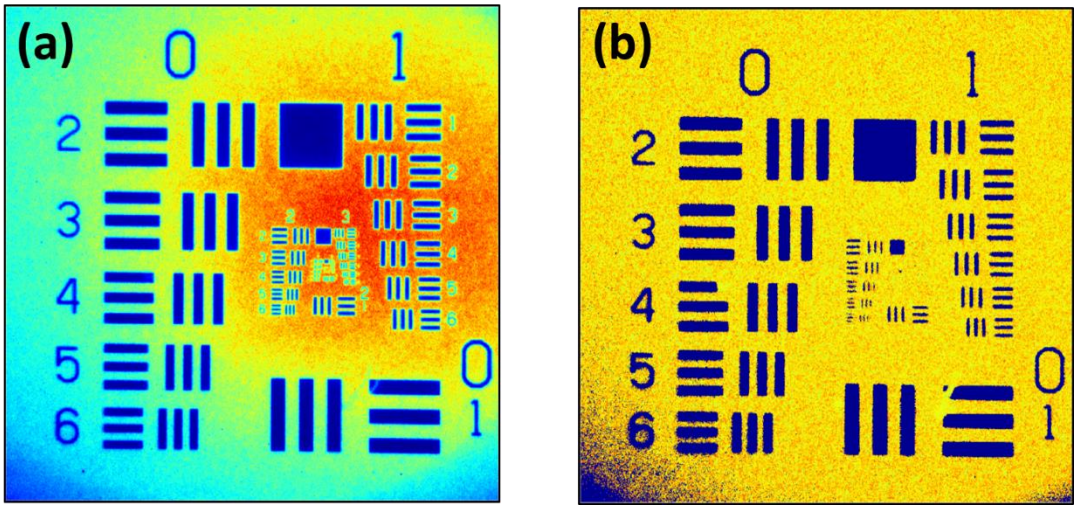

Figure 3.26 Imaging results using the 1951 USAF resolution test chart. (a) Fluorescence intensity image; (b) DOCI image.

Fluorescent dye solutions were used to verify the principles of the concept and characterize the basic characteristics of the system. Three types of fluorophores, each with two different concentrations are imaged simultaneously on the DOCI system and the result is compared with the measurement result from a commercially available FLIM system, i.e., the Leica Deep In Vivo Explorer SP8 DIVE at Advanced Light Microscopy and Spectroscopy (ALMS) Laboratory at the California NanoSystems Institute at UCLA.

In Figure 3.27 (a), from top to bottom, left to right, the drops are Laurdan (430 μM), Laurdan (650 μM), NADH (14500 μM), NADH (21500 μM), 7-Hydroxy-4-methylcoumarin

(200 μM) and 7-Hydroxy-4-methylcoumarin (400 μM), respectively. Figure 3.27 (b1) and (b2) are the decay image and reference image of the sample; Figure 3.27 (c) is the DOCI image of the sample from bandpass filter 605/15 nm. For each drop, a square region of interest (ROI) with the same size is picked for the mean and standard variation calculations. For the six drops mentioned, the corresponding mean and standard variation of DOCI values are 0.5225 ± 0.0077, 0.5237 ± 0.0069, 0.4064 ± 0.0067, 0.4038 ± 0.0061, 0.6183 ± 0.0070 and 0.6122 ± 0.0065. The fluorescence lifetimes of the samples were measured using the Leica FLIM system. The lifetimes of the Laurdan, NADH and 7-Hydroxy-4-methylcoumarin solutions were found to be 3.1 ns, 0.4 ns and 5.2 ns, respectively. Figure 3.27 (d) shows the fitted line using the DOCI values and the fluorescence lifetimes determined by FLIM. The fluorescent dye solution experiment shows that this DOCI system has a minimum temporal resolution of 0.16 ns.

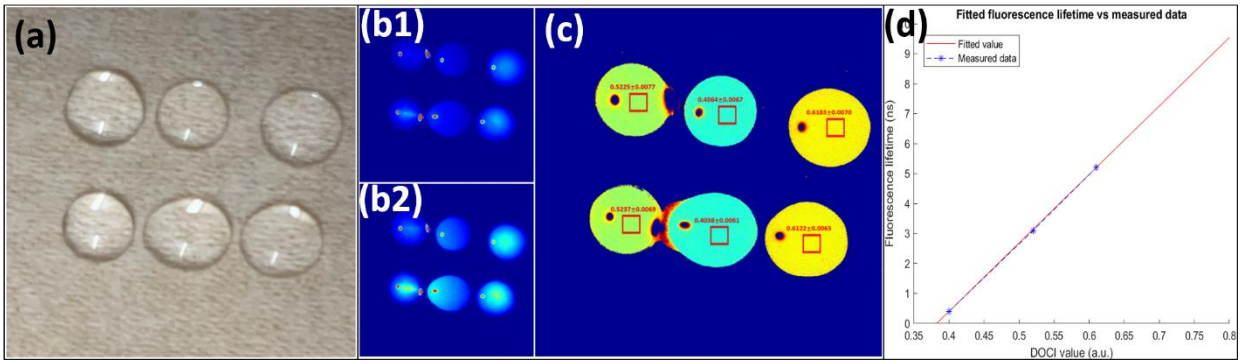

Figure 3.27 System characterization with fluorescence dyes. a) six drops of dyes (three types with two concentrations each) on a scope slide; b1) fluorescence intensity image taken in decaying period; b2) fluorescence intensity image taken in reference period; c) processed fluorescence lifetime (DOCI) image with means and standard variations noted in selected areas; d) DOCI values fitted to absolute fluorescence lifetime values with data from two-photon FLIM system. [43]

3.6. Conclusion

In this chapter, we discussed the system implementation of DOCI. An upgraded single-LED board is used in the current implementation to address the limitations of previous generation of DOCI system. 3 iterations of system design were implemented to accommodate different working conditions. A control software that features a simple-to-use GUI, complete device communication, and no-code parameter configuration was developed for system control. The characterization results of the current implementation demonstrated the performance of the system.

Chapter 4. Animal Tissue Differentiation

4.1. *Ex Vivo* and *In Vivo* Pig Tissue Imaging

4.1.1. Introduction

The pig tissue measurements served as an important for system validation, we have made a lot of improvements to the system based on the measurement results, including system architecture and system parameter adjustments. In the following, we select some representative data from both *ex vivo* and *in vivo* measurements for analysis, and explain the problems exposed and solutions we took.

4.1.2. Material And Methods

To demonstrate the ability for animal tissue differentiation, the *ex vivo* and *in vivo* DOCI systems were validated by imaging the thyroid gland and thyroid-adjacent tissues of healthy Yucatan mini pigs. The use of pigs for this study was approved by the Institutional Animal care and Use Committee (IACUC) at the University of California, Los Angeles. Table 4.1 shows the information on pigs used for imaging, including collection date, imaging method, tissue type and system used for imaging. For *ex vivo* imaging, the thyroid gland and adjacent tissues were excised and imaged with the *ex vivo* DOCI system. For *in vivo* imaging, freshly dead pigs were dissected to expose the thyroid gland and imaged with the *in vivo* DOCI system.

Table 4.1 Information on pigs used for DOCI imaging

#	Collection date	Method	Tissue type	System
1	12.19.2019	*Ex vivo*	Thyroid, thymus, fat	*Ex vivo* v1

2	12.20.2019	*Ex vivo*	Thyroid, thymus, fat	*Ex vivo* v1
3	7.20.2020	*Ex vivo*	Thyroid, fat	*Ex vivo* v2
4	10.20.2020	*Ex vivo*	Thyroid, fat	*Ex vivo* v2
5	10.20.2020	*Ex vivo*	Thyroid, thymus, fat, muscle, cartilage	*Ex vivo* v2
6	12.17.2020	*Ex vivo*	Thyroid, thymus, fat, lymph node	*Ex vivo* v2
7	12.17.2020	*Ex vivo*	Thymus	*Ex vivo* v2
8	3.19.2021	*Ex vivo*	Thyroid, thymus, fat, muscle	*Ex vivo* v2
9	6.8.2021	*Ex vivo*	Thyroid	*Ex vivo* v3
10	6.10.2021	*Ex vivo*	Thyroid, fat, muscle	*Ex vivo* v3
11	6.10.2021	*Ex vivo*	Thyroid, thymus, fat	*Ex vivo* v3
12	10.14.2021	*In vivo*	Thyroid, fat, muscle	*In vivo* v1
13	11.02.2021	*In vivo*	Thyroid, thymus, fat, muscle	*In vivo* v1

For each BPF channel, the normalized intensity image ($I_{norm,BPF}$) was calculated from the ratio of the aggregate steady-state fluorescence intensities between the BPF channel ($I_{SS,BPF}$) and the 405 nm LPF channel ($I_{SS,LPF}$):

$$I_{norm,BPF} = \frac{I_{SS,BPF}}{I_{SS,LPF}}$$

Normalization was applied to the steady-state fluorescence intensity data to alleviate the intensity variance caused by uneven illumination and rugged specimen surface.

4.1.3. Results

4.1.3.1. *Ex vivo* pig tissue imaging

Figure 4.1 shows the results of DOCI *ex vivo* imaging on pig tissues from pig #1, the *ex vivo* system with camera lens and 45° incident illumination (Figure 3.5 (a)) was used to acquire the data, the UV light generated has a repetition rate of 500 kHz and a pulse width of 40 ns. Thyroid, thymus, and adipose tissues were identified from H&E-stained histology (Figure 4.1 (b)), representative areas are highlighted in Figure 4.1 (a). Figure 4.1 (c) shows the fluorescence intensity image captured by the iCCD. With an exposure time of 0.5 s, the image preserved the details of the tissue. Figure 4.1 (d)-(f) are DOCI images from 3 selected channels: 405 nm LPF, 465/30 nm BPF and 572/28 nm BPF. Relatively, the adipose tissue has highest DOCI value, while the thyroid tissue has lowest DOCI value. The DOCI value maximum exceeds 1 because the applied pulse width was too short, so that the emission did not reach a complete steady state.

Meanwhile, the image has a lot of saturated areas (marked with red arrows) due to reflection from the excitation light output to the camera. The reflection resulted in elevated DOCI value of the corresponding area across all channels, as is shown in Figure 4.1 (d)-(f). BPF channels 415/10 nm, 434/17 nm and 465/30 nm are less affected and channels with longer wavelengths are more severely affected, indicating the reflected light consists mainly of long wavelength light. The reason for the reflection is that we did not filter the light when we collected this set of data, so the impurity light reached the surface of the sample and was reflected to the image sensor.

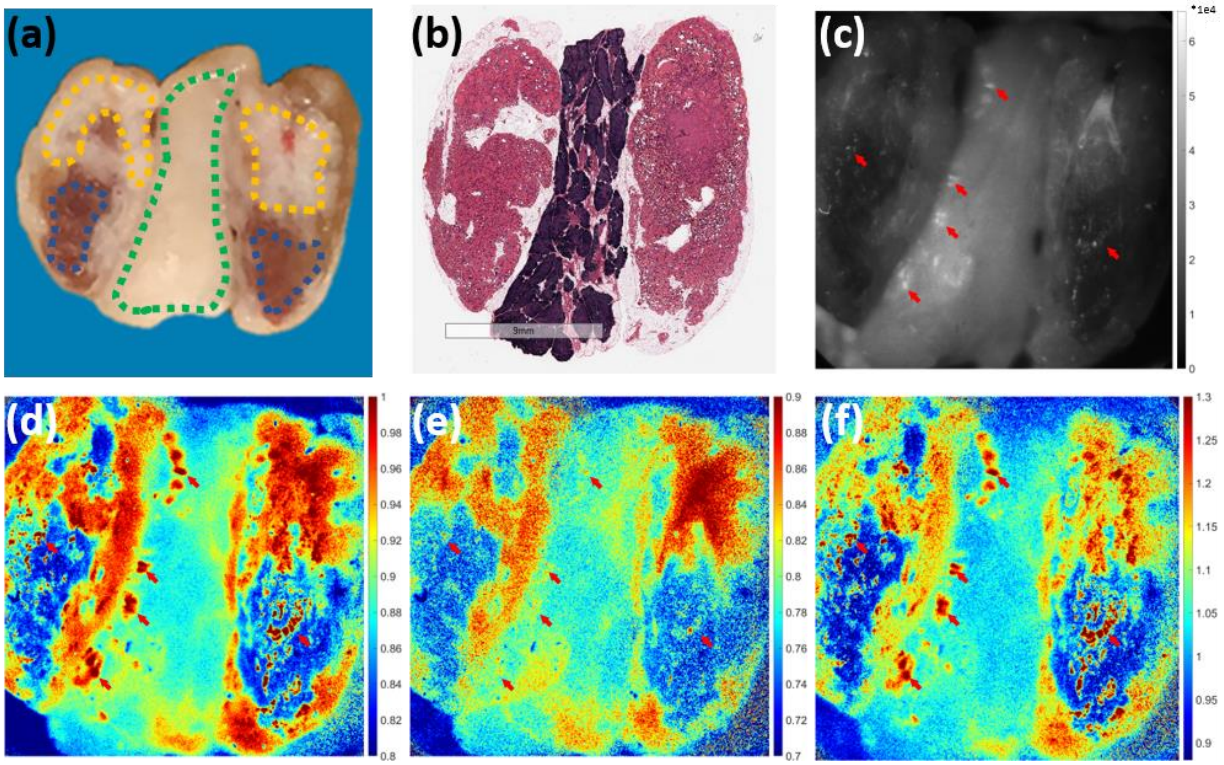

Figure 4.1 Pig *ex vivo* tissue image results from pig #1 in Table 4.1. (a) DSLR color image, areas highlighted with dashed lines are thyroid (blue), thymus (green) and adipose (yellow). (b) H&E-stained histology image (scalebar: 9 mm). (c) Fluorescence intensity image. (d) 405 nm LPF channel DOCI image. (e) 465/30 nm BPF channel DOCI image. (f) 572/28 nm BPF channel DOCI image. Red arrows in (c)-(f) denotes reflection hotspots.

Figure 4.2 shows the results of DOCI *ex vivo* imaging on pig tissues from pig #6 and #7, the system employed optical filters to eliminate the long-wavelength background of the excitation light, thus greatly reduced the reflection. A longer pulse width of 80 ns was applied to the excitation light, giving the fluorescence emission enough time to reach the steady-state and less chance to yield a DOCI value larger than 1. Thyroid, thymus, fat, and lymph node tissues were identified from H&E-stained histology (Figure 4.2 (b)). In Figure 4.2 (b), a couple of saturated hotspots are visible, they are not from reflection, but from exotic microfibers that got accidentally attached to the tissues. Figure 4.3 shows the box plots of DOCI values and normalized fluorescence

intensity values of pig tissue data corresponding to Figure 4.2. Distinctively different features can be observed from both DOCI values and intensity values. The two lymph node tissues have very similar values, as they were collected from the same lymph node specimen. The two thymus tissue data look slightly different, it comes from individual differences as they were harvested from two different pigs.

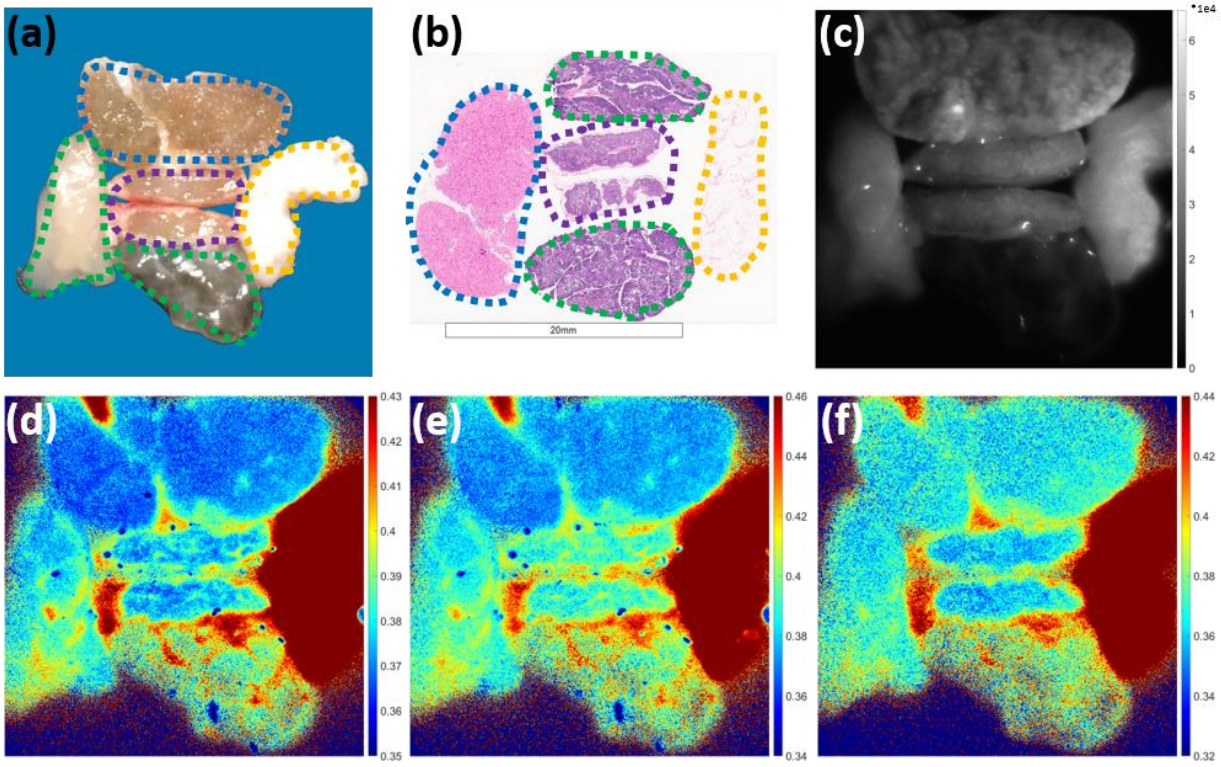

Figure 4.2 Pig *ex vivo* tissue image results from pig #6 and #7 in Table 3.1. (a) DSLR color image, areas highlighted with dashed lines are thyroid (blue), thymus (green), adipose (yellow) and lymph node (purple). (b) H&E-stained histology image (scalebar: 20 mm), all sections have one-to-one matching to the tissues in (a) except the positions of top thyroid and left thymus are swapped. (c) Fluorescence intensity image. (d) 405 nm LPF channel DOCI image. (e) 465/30 nm BPF channel DOCI image. (f) 572/28 nm BPF channel DOCI image.

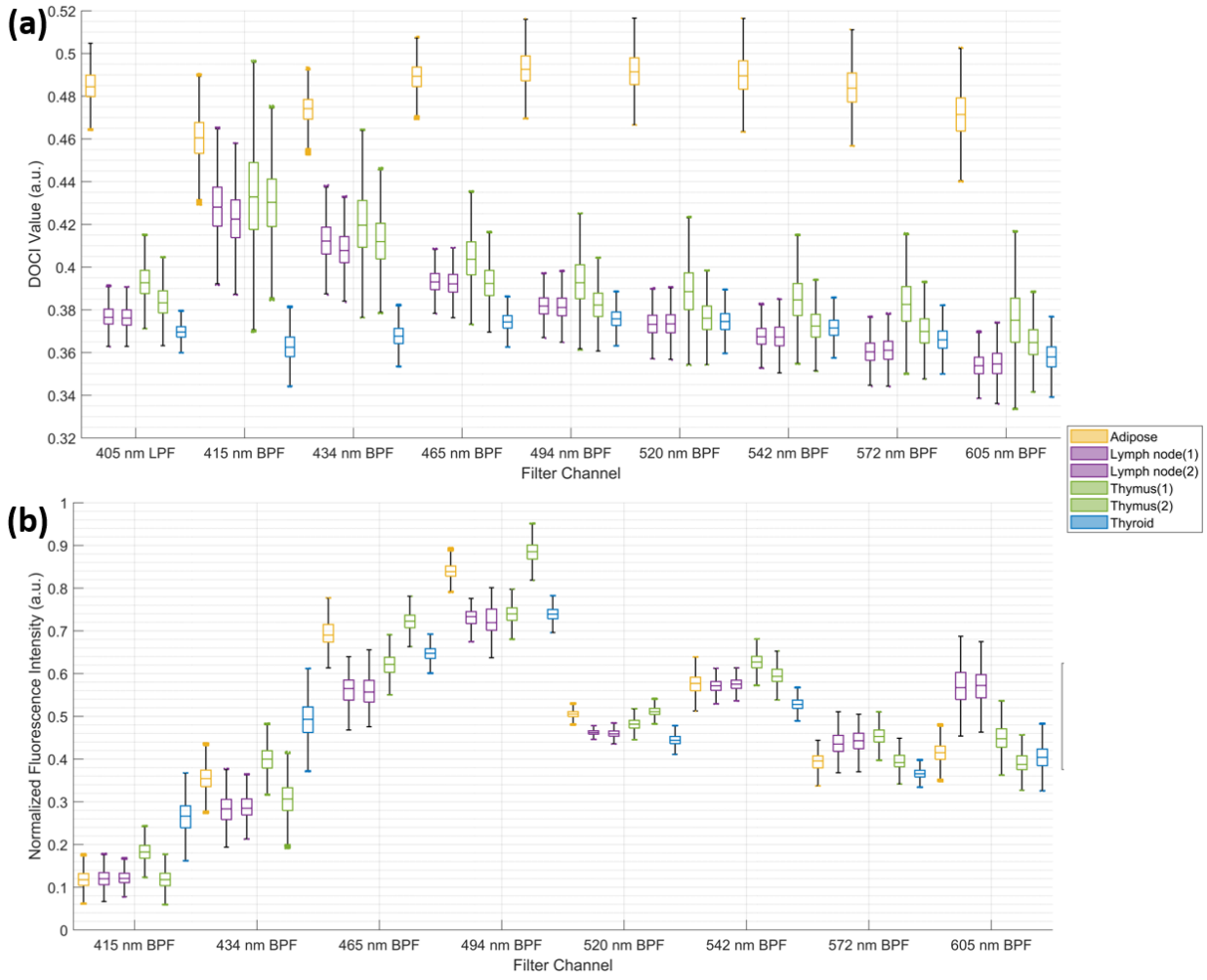

Figure 4.3 Box plots of (a) DOCI values and (b) normalized fluorescence intensity values of pig tissue data shown in Figure 4.2.

Figure 4.4 and Figure 4.5 shows the results of DOCI *ex vivo* imaging on pig tissues from pig #10 and #11, for the measurements we employed an optimized data acquisition flow on the iCCD camera, therefore the DOCI values of for the same type of tissue in Figure 4.3(a) and Figure 4.5(a) look different. We also applied the same sensor gain to all filter channels for quantitative analysis, therefore the normalized fluorescence intensity values for the same type of tissue look different in Figure 4.3(b) and Figure 4.5(b). The two thyroid specimens were collected individually

from pig #10 and #11, individual differences can be observed in their corresponding DOCI values and normalized intensity values.

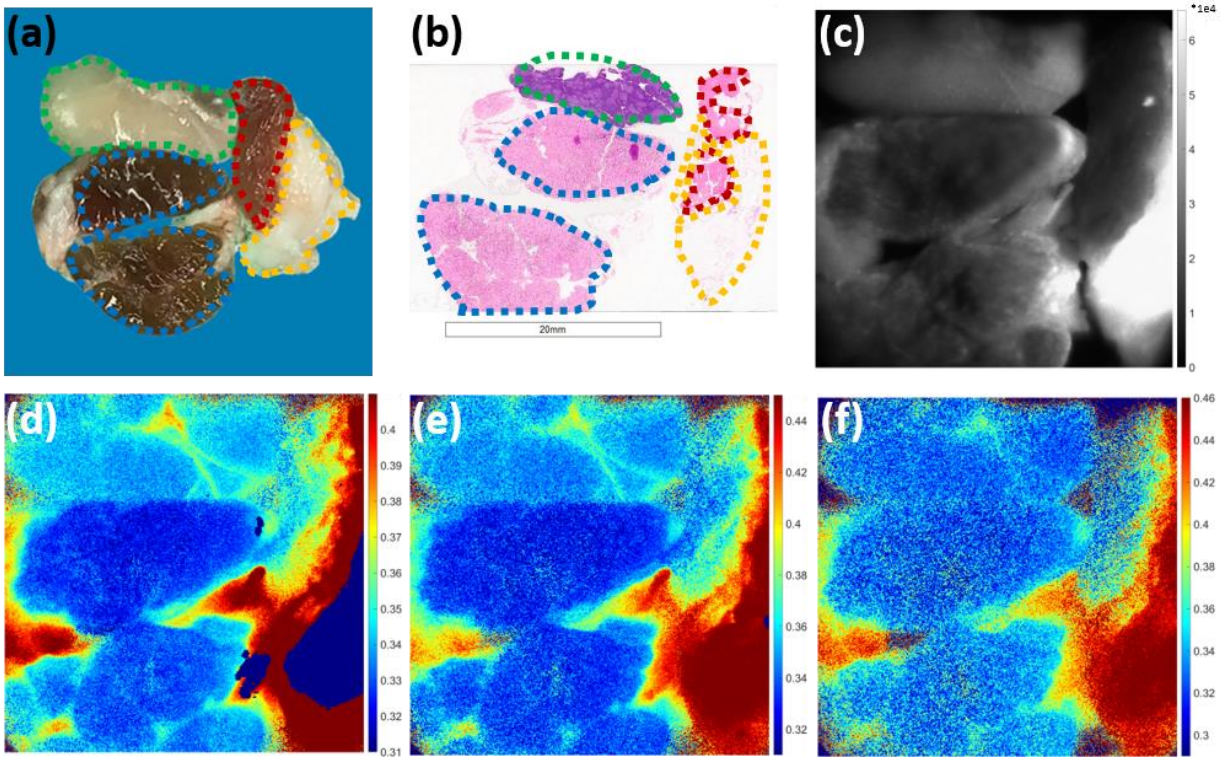

Figure 4.4 Pig *ex vivo* tissue image results from pig #10 and #11 in Table 3.1. (a) DSLR color image, areas highlighted with dashed lines are thyroid (blue), thymus (green), adipose (yellow) and muscle (red). (b) H&E-stained histology image (scalebar: 20 mm). (c) Fluorescence intensity image. (d) 405 nm LPF channel DOCI image. (e) 465/30 nm BPF channel DOCI image. (f) 572/28 nm BPF channel DOCI image.

Figure 4.5 Box plots of (a) DOCI values and (b) normalized fluorescence intensity values of pig tissue data shown in Figure 4.4.

4.1.3.2. *In vivo* pig tissue imaging

Figure 4.6 shows the *in vivo* imaging data from pig #12 and #13, Figure 4.6 (a) and (e) are reconstructed regular color images from the iCCD. Red, green, and blue filters were mounted in the filter wheel to yield single-channel images. The relationship of DOCI values among different tissue types is different between the *ex vivo* results from last section and the *in vivo* results: for *ex vivo* results, the adipose tissue had much higher DOCI value than other tissue types for all channels, with the second highest DOCI values from muscle tissue and the lowest from thyroid tissue; for *in*

vivo results, from low to high, the tissue types are muscle, thyroid, thymus and adipose, the difference between adipose tissue and other tissues are no longer so great. The difference between the *ex vivo* and *in vivo* results is mainly due to the fact that the tissues used for *ex vivo* imaging were sectioned to expose the internal tissue, which has a homogenous composition of the corresponding tissue type. For *in vivo* imaging, after located the thyroid and thymus tissues, we first attempted to remove the superficial connective and adipose tissues, but there were still some residual layers in place, the tissue inhomogeneity led to elevated DOCI values as doped adipose tissue has higher DOCI values.

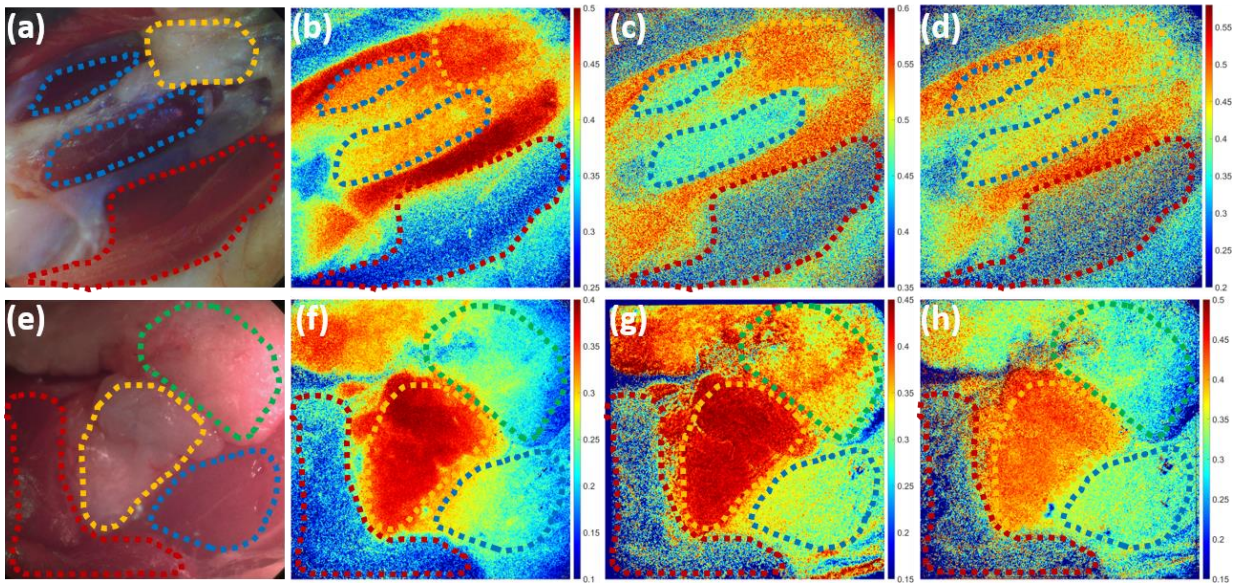

Figure 4.6 Pig *in vivo* tissue image results from pig #12 and #13 in Table 3.1. (a)-(d) Pig #12: (a) Regular color image; (b) 405 nm LPF channel DOCI image; (c) 465/30 nm BPF channel DOCI image; (d) 542/27 nm BPF channel DOCI image. (e)-(h) Pig #13: (a) Regular color image; (b) 405 nm LPF channel DOCI image; (c) 465/30 nm BPF channel DOCI image; (d) 542/27 nm BPF channel DOCI image. Areas highlighted with dashed lines are thyroid (blue), thymus (green), adipose (yellow) and muscle (red).

4.2. *In Vivo* Murine Tissue Imaging

4.2.1. Introduction

In this study, we demonstrate that DOCI can be utilized in an *in vivo* mouse model with head and neck squamous cell carcinomas (HNSCC) to identify malignant tissue and guide tumor resection and margins. We further demonstrate that DOCI can accurately identify microscopic perineural invasion with a 100% sensitivity and specificity. This proof-of-concept study demonstrates that DOCI has the potential to revolutionize cancer care by allowing the surgeon to precisely determine cancer margins and the presence of perineural invasion intraoperatively. In this study, we used the *ex vivo* DOCI system (Figure 3.5 (a)) with a modified imaging unit to have a smaller field of view.

4.2.2. Material And Methods

4.2.2.1. *In Vivo* Murine Model

The use of mice for this study was approved by the IACUC at the UCLA. Eight C3H/HeJ male mice underwent subcutaneous, bilateral flank injection either 500,000 SCC7 cells (RRID: CVCL_V412), a murine head and neck cancer cell line. Tumors were allowed to grow for a period of three weeks. 15 tumors successfully grafted to the host. The mice were then anesthetized with weight-based dosing of ketamine as well as carprofen. Under anesthesia, the mice were sterilely prepped for a surgery and a midline incision was made through the skin; bilateral skin flaps were raised until the tumor was exposed. At this point, the mice underwent DOCI imaging to determine the extent of resection necessary. After assessing DOCI imaging, tumor resection was performed, followed by additional DOCI imaging of the tumor bed. Any residual tumor detected on DOCI was then resected. Both tumor and adjacent tissue margins were sent to the translational pathology core laboratory (TPCL) for permanent sectioning

4.2.2.2. Perineural Invasion Model

Methods for the creation of a nerve model of perineural invasion were adapted from Deborde et al. [49] After induction of general anesthesia with weight-based ketamine, the bilateral sciatic nerves of six C3H/HeJ were dissected and exposed. Under a dissecting microscope and using a 33-gauge needle (Hamilton Company, Reno, NV), 3 µL of phosphate buffered saline (PBS) was slowly injected into the perineurium of the left sciatic nerve. Then, 50,000 SCC7 cells (RRID: CVCL_V412) in 3uL of PBS was injected into the perineurium of the right sciatic nerve. The skin was then re-approximated with 5-0 Nylon sutures and the mouse was allowed to recover. All mice were noted to have normal limb function post-operatively.

4.2.2.3. Sciatic Nerve Harvesting

On post-operative days 7, 10, and 14, the mice were again induced under general anesthesia with ketamine. The prior incision was opened, and the bilateral sciatic nerves were exposed. White light images were taken using a camera attached to the dissecting microscope. The bilateral nerves were then imaged using the *ex vivo* DOCI system. After imaging, the mice were euthanized with ketamine. The sciatic nerves were harvested proximally at the level of the spinal cord and distally at the end of the femur and then sent to TPCL for permanent sectioning.

4.2.3. Results

4.2.3.1. DOCI Delineates Margins Between HNSCC And Adjacent Healthy Tissue

After surgically exposing the flank, DOCI imaging was utilized to both identify the location of the tumor and guide resection (Figure 4.7). Tumor sizes ranged from 1 mm to 15 mm with an average size of 7 mm. Tumors were often difficult to distinguish from surrounding healthy tissue with

white light alone but were clearly identified with DOCI imaging (Figure 4.7 A). DOCI imaging delineated the margins between HNSCC (green), compared to muscle (blue) and adipose tissue (red). Permanent histology of the tumor and adjacent healthy tissue was concordant with DOCI imaging (Figure 4.7A, B). Following resection, the margins surrounding the tumor bed were re-imaged, revealing a 3 mm foci of remaining tumor inferior to the tumor bed (Figure 4.7C). DOCI was able to direct further resection in this area, where the tumor was not appreciated by the surgeon's visualization or palpation.

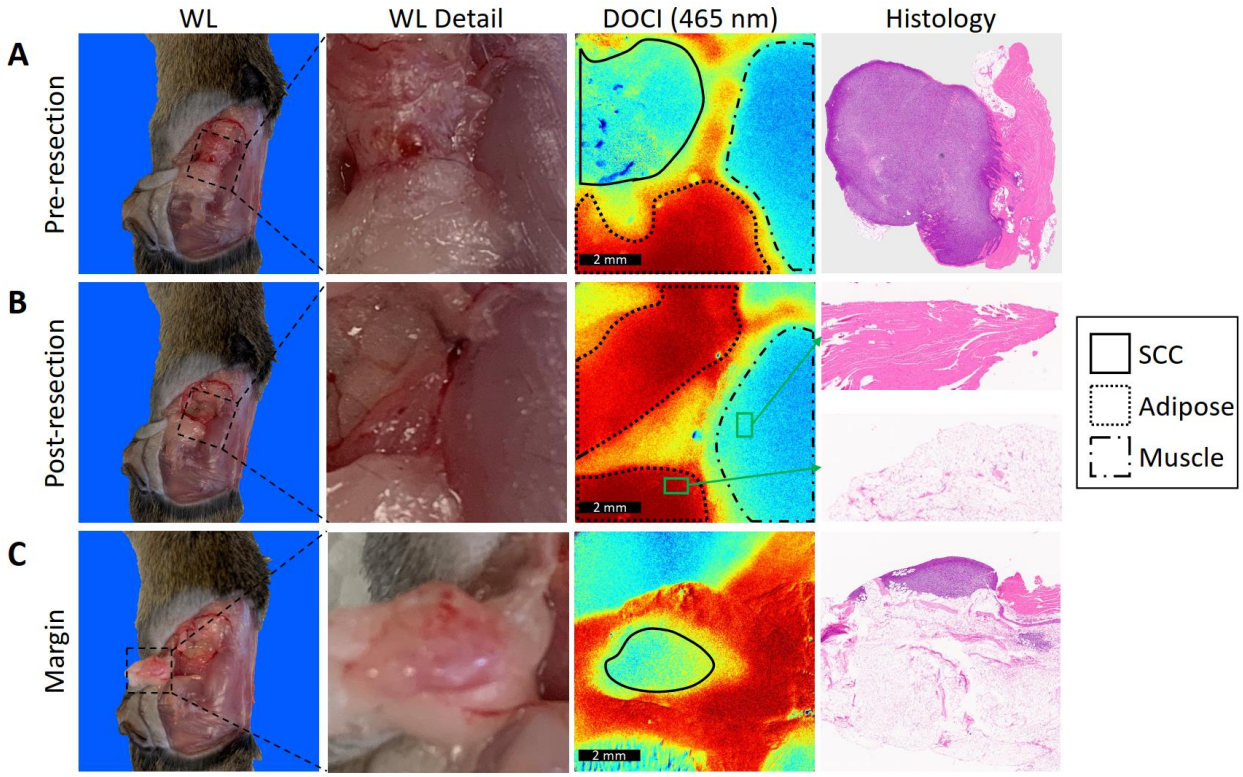

Figure 4.7 DOCI delineates margins between HNSCC and adjacent healthy tissue. A) Prior to surgical resection of the tumor, DOCI was utilized to identify the tumor and determines margins. White light (WL) detail images and DOCI images were captured at a 1:1 ratio for direct comparison. Histology demonstrated HNSCC, concordant with DOCI imaging. B) After resection, the tumor bed was imaged to identify any areas of tumor remaining. Histology taken from surrounding margins confirms healthy adipose and muscle tissue (green inset). C) DOCI imaging of margins reveals un-resected tumor along an adipose fat pad. Histology

confirms HNSCC with adjacent adipose fat. White light (WL), Dynamic Optical Contrast Imaging (DOCI), squamous cell carcinoma (SCC).

The average relative lifetimes of different tissue types as a function of wavelength are shown in Figure 2 A. Each tissue type—including muscle, dermal adipose tissue (DAT), adipose tissue, nerve—has a unique DOCI value and trend relative to HNSCC. Overall, the 465 nm BPF shows the greatest contrast between tissues (Figure 2 A). P values were calculated for the DOCI values of each tissue type compared to SCC across all BPFs (Figure 2 B).

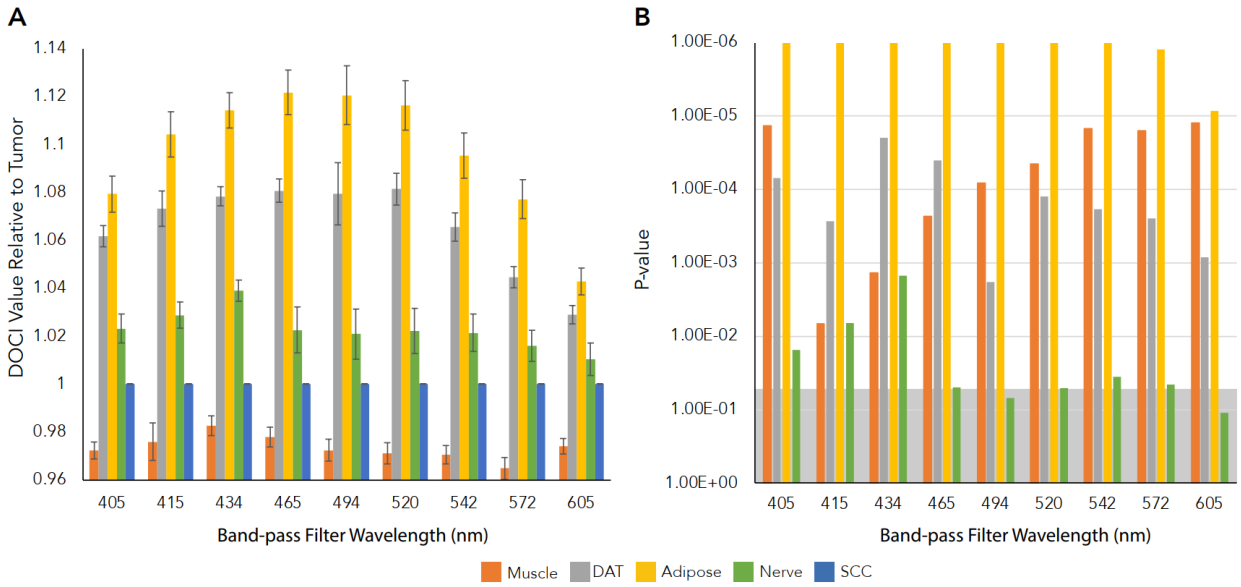

Figure 4.8 DOCI values of healthy and malignant tissue. A) DOCI values of different tissue types as a function of wavelength (n=15). B) Manhattan plot of P values for DOCI values of each tissue type compared to HNSCC across all wavelengths. Significance is defined as $P<0.05$. The significance threshold is denoted in gray and all bars above the threshold are considered significant. DAT: dermal adipose tissue.

4.2.3.2. DOCI Accurately Identifies Perineural Invasion

After validating that DOCI can delineate HNSCC margins in our *in vivo* murine model, we investigated the capacity of DOCI to identify PNI. DOCI images from sciatic nerves injected with PBS were compared to sciatic nerves injected with SCC7 (Figure 4.9). Control nerves had higher

relative lifetimes (white arrowheads) that were consistent along the entire length of the nerve. In contrast, portions of the nerve with perineural invasion had lower relative lifetimes (black arrowheads) compared to both the control nerve as well as healthy nerve adjacent to the tumor (grey arrowheads). Histology is concordant with DOCI imaging and also demonstrates the transition point between normal nerve and PNI. Control nerves had an average diameter of 0.81 mm. PNI+ nerves had a diameter ranging from 0.91 mm to 2.36 mm; there was a positive correlation between post-operative day and diameter of the PNI+ portion of the nerve. Mouse hindlimb function was intact in all mice after injection.

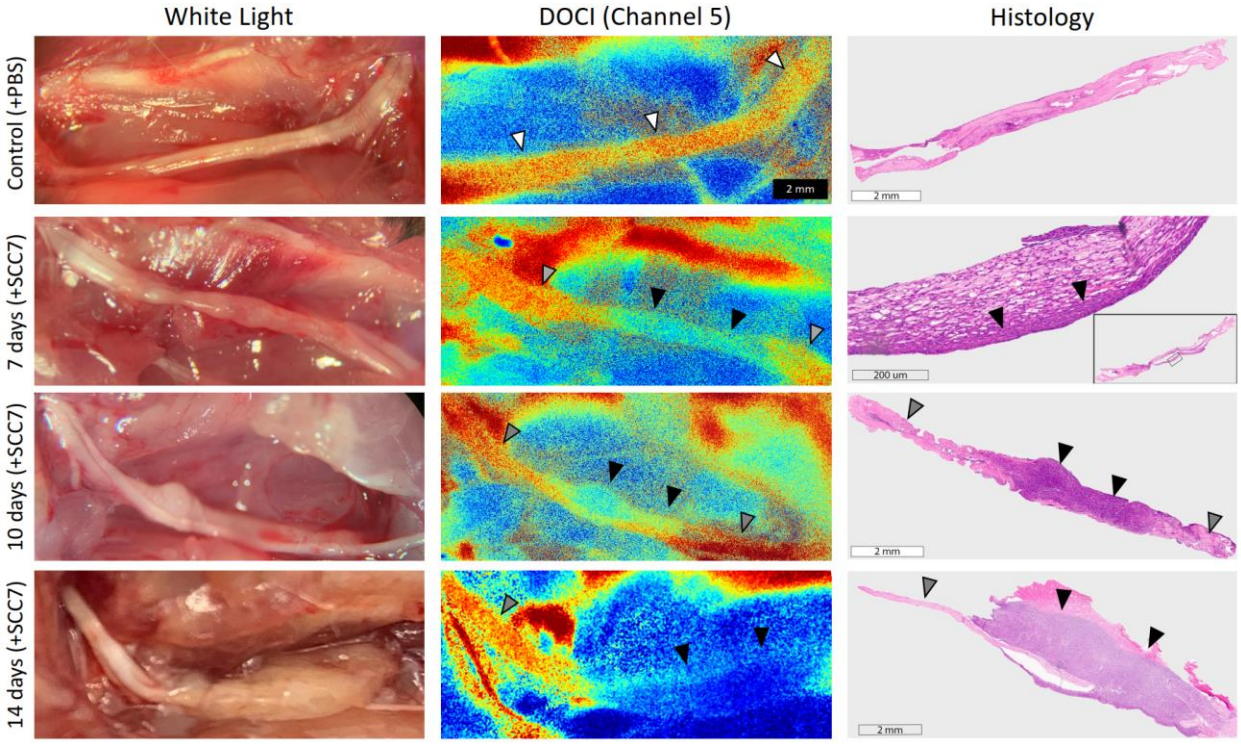

Figure 4.9 DOCI accurately identifies perineural invasion. The left sciatic nerves were injected with PBS while the right sciatic nerves were injected with SCC7. Sciatic nerves were harvested at 7, 10, and 14 days. All nerves underwent white light imaging, DOCI imaging, and permanent histologic sectioning. White arrowheads denote the control nerve, black arrowheads PNI, and grey arrowheads the normal nerve adjacent to the tumor.

The average relative lifetimes of several regions of interest including control and PNI+ nerve are shown in Figure 4.10 A. Healthy nerve adjacent to tumor (PNI-) is plotted separately from the control nerve (PBS) but shows no statistically significant difference across all wavelengths (Table 4.2). The P values of the different tissue types compared to PNI+ nerve are displayed in Figure 4.10 B as a Manhattan plot. In all BPFs, there was a significantly significant difference in DOCI values between the control and PNI+ nerve (Figure 4.10 B).

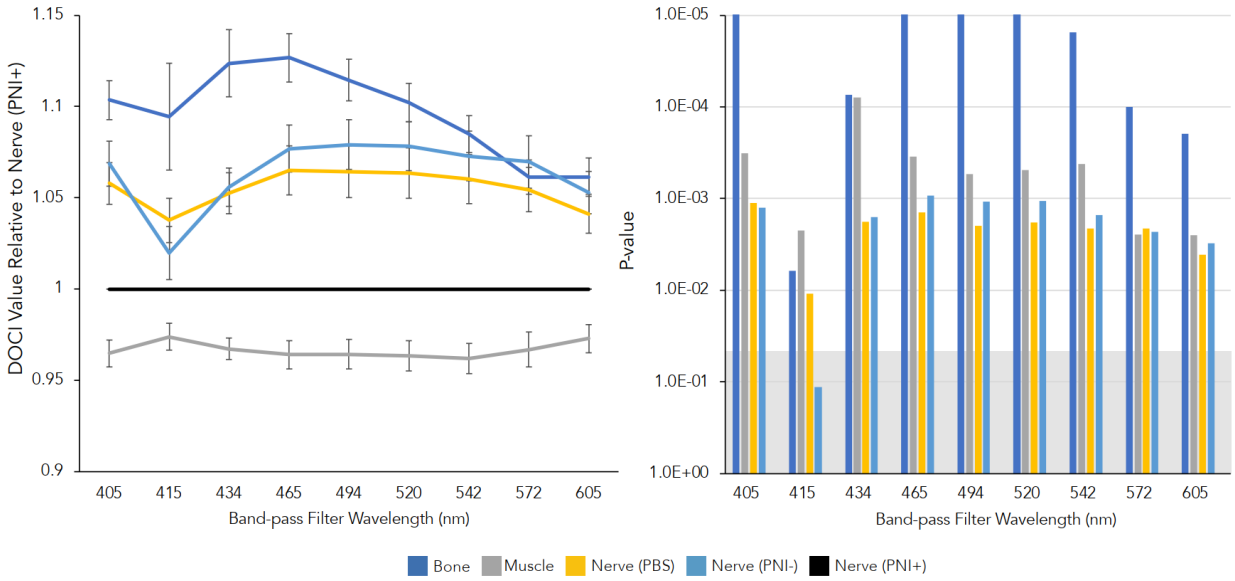

Figure 4.10 DOCI values of PNI compared to healthy tissue. A) DOCI values of different tissue types as a function of wavelength (n=6). PNI- nerve refers to normal nerve adjacent to tumor. B) Manhattan plot of P values for DOCI values of each tissue type compared to PNI+ nerve across all wavelengths. Significance is defined as $P<0.05$. The significance threshold is denoted in gray and all bars above the threshold are considered significant.

Table 4.2 *p*-value of PNI- nerve compared to PNI+ nerve

Filter	405 nm	415 nm	434 nm	465 nm	494 nm	520 nm	542 nm	572 nm	605 nm

p-value	0.53	0.37	0.83	0.53	0.47	0.47	0.52	0.44	0.48

4.2.4. Discussion

In this study, we demonstrate that DOCI can be reliably used in real-time *in vivo* to guide cancer resection and margins during surgery. Furthermore, DOCI can accurately identify perineural invasion, allowing the surgeon to identify in real-time which nerves need to be sacrificed and which reconstructive options are available once the affected nerve portion is removed. This is a very useful capacity as currently, PNI is determined by the surgeon's visualization of gross neural invasion or by frozen section analysis, which requires sectioning the nerve and thereby rendering it nonfunctional.

In terms of detecting PNI, the 465 nm wavelength appears to provide the greatest DOCI contrast between healthy neurons, bone, muscle, and PNI (Figure 4 A). The 465 nm wavelength also appears to provide excellent contrast between healthy tissues and HNSCC (Figure 2A). Research into the mechanism by which DOCI detects PNI is ongoing and is likely due to alterations in the biochemical properties of HNSCC as well as a disruption of the endogenous fluorophores that are unique to healthy neurons. Malignant tissues have a number of biochemical and structural changes that occur including alteration to the concentrations of the reduced form of nicotinamide adenine dinucleotide (NADH) and flavin adenine dinucleotide (FAD). For HNSCC specifically, NADH has been determined to be the main contributor to changes in fluorescence lifetime compared to healthy tissue. [50-52]

4.3. Conclusion

In this chapter, we presented studies on animal and human tissues. *Ex vivo* and *in vivo* pig tissues were used for system evaluation and optimization, and measurements showed clear differences between different tissue types. *In vivo* imaging was performed on two kinds of murine models, with SCC invasions on bilateral flank and sciatic nerves, respectively. DOCI measurement results showed that tumor margins were accurately delineated for both two models.

Chapter 5. *Ex Vivo* Hypercellular Parathyroid Gland Differentiation

5.1. Introduction

Primary hyperparathyroidism is one of the most common endocrine diseases, with an estimated prevalence of 0.86% in the United States [53]. Primary hyperparathyroidism is often caused by a solitary adenoma (80% - 85%), four-gland hyperplasia (10% - 15%) or carcinoma (<1%) resulting in elevated parathyroid hormone (PTH) [54]. Surgical excision of pathological gland is the standard of care as removal of the affected lesion effectively lowers PTH to normal limits [55]. Parathyroid glands can be difficult to identify intraoperatively as they have variable locations and indistinct visual and palpable features from surrounding fat, thymus, and lymph nodes, making parathyroid gland surgeries challenging. Inadvertent removal or devascularization of normal parathyroid tissue may result in significant morbidity and hypocalcemia [56].

Several preoperative imaging modalities such as ultrasonography, four-dimensional parathyroid computed tomography (4D-CT), MRI, and technetium-99m sestamibi scintigraphy are available for parathyroid localization. However, these methods are often insufficient to completely and accurately identify the correct location of the parathyroid glands, and in as many as 10% of operations the affected parathyroid gland is not localized [57, 58]. The establishment of intraoperative methods for parathyroid identification would greatly increase the success of gland localization, and thus would potentially help reduce the number of surgical complications [59]. While surgeons conventionally rely on frozen section histologic analysis because it accurately confirms the parathyroid tissue, the approach is invasive, time-consuming and costly [60].

Recently, various novel invasive and non-invasive methods have been developed as intraoperative adjuncts, such as methylene blue (MB) staining [61, 62], ICG angiography, [63, 64] and near-infrared autofluorescence (NIRAF) [65, 66]. MB stains parathyroid glands after intravenous administration, thus making parathyroid glands visible. ICG marks parathyroid glands via fluorescence when excited with NIR light. However, both MB and ICG may localize non-specifically to thyroid glands [67, 68], which can present complications for the accurate identification of the parathyroid glands. In addition, while intravenous administration of ICG and MB are overall well tolerated by the majority of patients, adverse effects can occur ranging from dermatitis to anaphylaxis [69, 70]. NIRAF is based on the autofluorescence of parathyroid glands excited by near infrared light. However, the detection of the autofluorescence is negatively impacted by ambient light [71]. The future goal for facile and clinically relevant intraoperative parathyroid identification should be non-invasive, easy to implement and affordable.

Since primary hyperparathyroidism is most often caused by solitary adenomas [54], it would be highly beneficial to be able to distinguish between hypercellular parathyroid adenomas and normal parathyroid glands. In this chapter, we demonstrate that DOCI and integrated machine learning algorithms can be utilized to visually differentiate and classify hypercellular parathyroid adenomas from normal parathyroid glands and surrounding tissue.

5.2. Materials and Methods

5.2.1. Tissue Collection

The acquisition of human tissue specimens for this study was approved by the UCLA Institutional Review Board (IRB). Suitable human subjects were identified from patients who underwent parathyroid and thyroid surgery at Ronald Reagan UCLA Medical Center. The tissue specimens

were imaged with DOCI immediately post resection. For each specimen imaged via DOCI, the tissue type composition of a corresponding sample was confirmed using H&E histology by a blinded head and neck pathologist. A total of 115 tissue specimen were obtained from 47 patients.

5.2.2. DOCI Instrumentation

In this study, the *ex vivo* DOCI system with camera lens and 45° incident illumination (Figure 3.5 (a)) was used for imaging. The fluorescence emission was spectrally resolved into 8 spectral channels using one 405 nm LPF (BLP01-405R-25, Semrock) to ensure blockage of all excitation source light, and 7 band-pass filters BPF with center wavelength/FWHM of: 434/17 nm (FF01-434/17-25, Semrock), 465/30 nm (FF01-465/30-25, Semrock), 494/20 nm (FF01-494/20-25, Semrock), 520/15 nm (FF01-520/15-25, Semrock), 542/27 nm (FF01-542/27-25, Semrock), 572/28 nm (FF01-572/28-25, Semrock), and 605/15 nm (FF01-605/15-25, Semrock). The UV excitation light pulse had a repetition rate of 500 kHz and a pulse width of 80 ns. An exposure time of 0.5 s per window was applied for imaging.

5.2.3. Image Processing

A DOCI image was computed for all 8 filter channels, and a normalized intensity image was computed for all 7 BPF channels. An aggregate intensity measurement was recorded from the moment the illumination started to decrease until the fluorescence ceased. For each BPF channel, the normalized intensity image ($I_{norm,BPF}$) was calculated from the ratio of the aggregate steady-state fluorescence intensities between the BPF channel ($I_{SS,BPF}$) and the 405 nm LPF channel ($I_{SS,LPF}$):

$$I_{norm,BPF} = \frac{I_{SS,BPF}}{I_{SS,LPF}}$$

Normalization was applied to the steady-state fluorescence intensity data to alleviate the intensity variance caused by uneven illumination and rugged specimen surface.

5.2.4. Statistical Analysis and Machine Learning Classification

The data analyses were performed with MATLAB R2021a. For each tissue sample with identified tissue type, one region-of-interest (ROI) was selected. For each ROI, the medians of the multi-spectral DOCI values and normalized intensity values were extracted as features for subsequent analysis. The nonparametric Wilcoxon Rank Sum Test [72] was used to compare the single-channel data between different tissue types. To investigate the classification task of hypercellular parathyroid versus other types of tissue, we selected 3 classifier models that have been adapted to multivariate analysis and classification of topics with complex samples in the biomedical community: logistic regression (LR) [73, 74], k-nearest neighbors (KNN) [75, 76] and artificial neural networks (ANN) [77]. The leave-one-out cross-validation was applied for classification performance evaluation: for each fold, one specimen was tested on the classifier model trained with the remaining specimens, this was repeated for all specimens and the mean performance was calculated.

5.3. Results

Of the 47 patients included in this study, 29 patients had at least one parathyroid gland removed, 23 patients had thyroid tissue removed, and 4 patients had both parathyroid and thyroid tissue removed (all based on clinical indications). Table 5.1 outlines all tissue specimens collected from the 47 individuals.

Table 5.1. Tissue Specimens Imaged Using DOCI

Tissue type	Count	Specimens	Patients
Hypercellular parathyroid	31	32.3%	55.3%
Normal parathyroid	6	6.3%	8.5%
Thyroid	35	36.5%	48.9%
Thymus	7	7.3%	12.8%
Lymph node	13	13.5%	14.9%
Adipose	25	24.0%	31.9%

Figure 5.1 demonstrates the DOCI results of different tissues collected from the same patient. The 405 nm LPF channel DOCI scans of three specimens are displayed here: hypercellular parathyroid (Figure 5.1 (A)), thyroid (Figure 5.1 (B)) and adipose (Figure 5.1 (C)). Corresponding H&E histology images (Figure 5.1 (D-F)) are shown below each DOCI image. Circular ROIs are highlighted in the DOCI images. The labeled tissue type only applies to the tissues in the ROI. The histology is matching the specific ROI portion. DOCI data from selected ROIs (Figure 5.1 (G)) show that the DOCI value of hypercellular parathyroid is smaller than thyroid ($p<0.001$) and adipose ($p<0.001$).

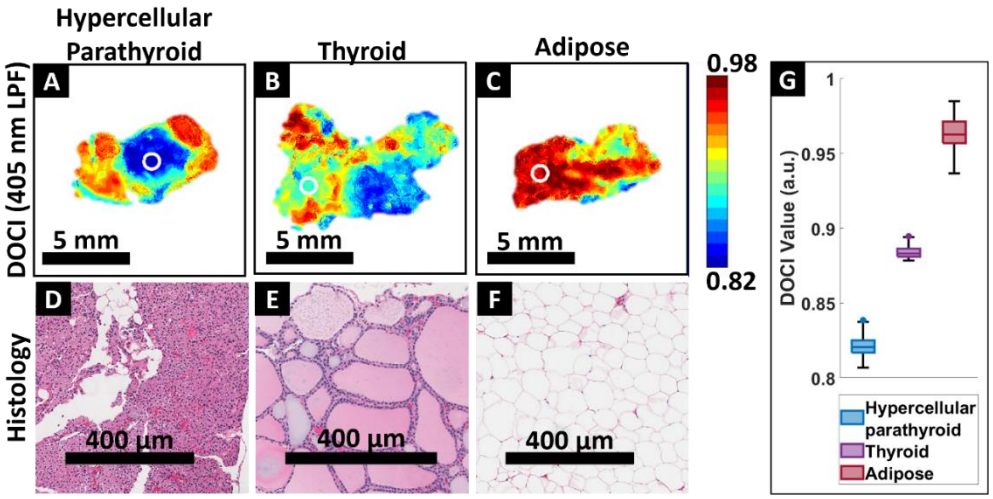

Figure 5.1 DOCI images of parathyroid (A), thyroid (B) and adipose (C) tissues, which were collected from the same patient. (D) - (F) Corresponding H&E histology confirms tissue composition. (G) Box plot of DOCI data from white circular ROIs marked on (A) - (C)

For each ROI, a total of 15 features were extracted: DOCI values from all 8 filter channels and normalized intensity values from 7 BPF channels. These features were grouped by tissue type and tested for statistical significance. Figure 5.2 shows the grouped box plot of DOCI values for each filter channel, and Figure 5.3 shows the grouped box plot of normalized intensity value for each BPF channel. The Wilcoxon Rank Sum Test was used for comparing hypercellular parathyroid with other tissue types, Figure 5.4 and Figure 5.5 show the Manhattan plots of calculated P values. A significant difference ($p<0.05$) in DOCI value was observed between hypercellular parathyroid and other tissue types for all 8 filter channels, except for hypercellular parathyroid versus normal parathyroid in the 434 nm BPF channel. Additionally, a significant difference ($p<0.05$) in normalized intensity value was observed between hypercellular parathyroid and two types of tissue, thyroid and adipose, for all 7 BPF channels.

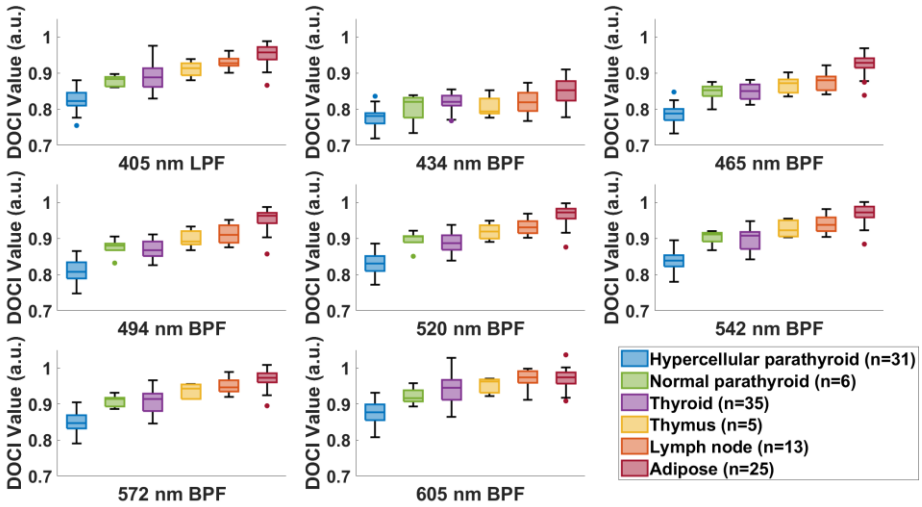

Figure 5.2 Box plots of DOCI value medians for all tissue types.

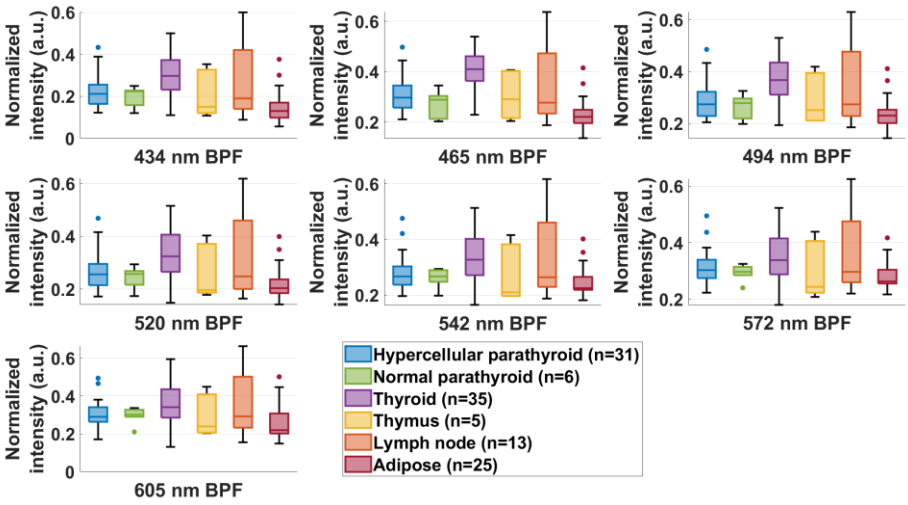

Figure 5.3 Box plots of normalized steady-state fluorescence intensity value medians for all tissue types.

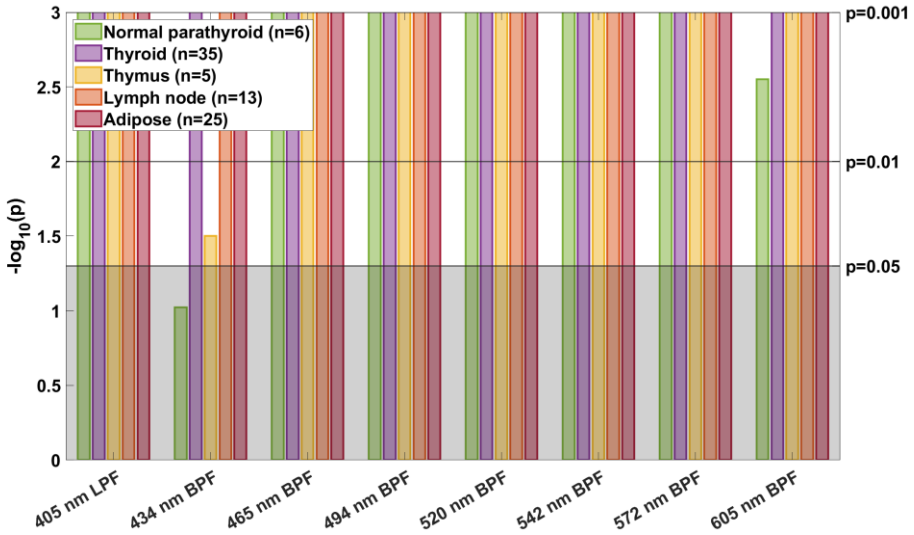

Figure 5.4 P values of DOCI value displayed as Manhattan plots, P values were calculated from the Wilcoxon Rank Sum Test between hypercellular parathyroid and other 5 tissue types. $p < 0.05$ is labeled as significant, $p = 0.01$ and $p = 0.001$ are also marked for reference.

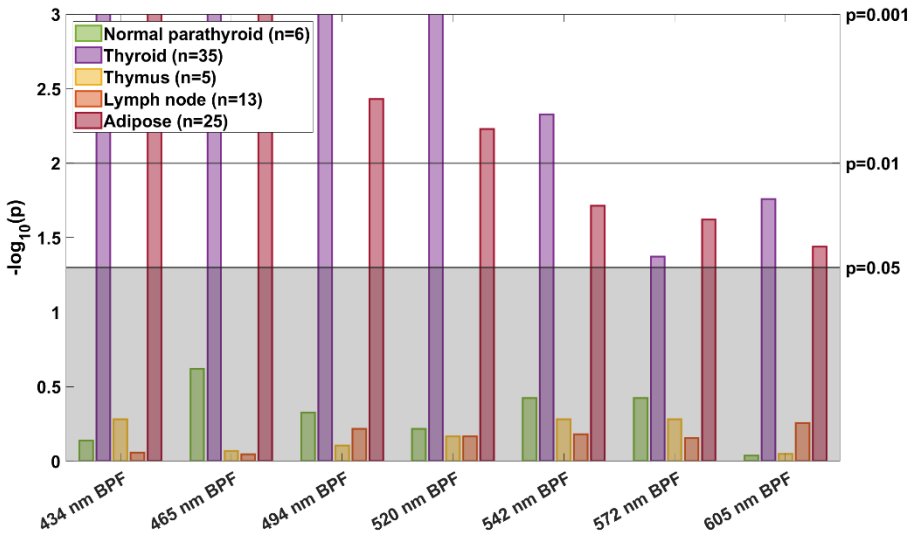

Figure 5.5 P values of DOCI value displayed as Manhattan plots, P values were calculated from the Wilcoxon Rank Sum Test between hypercellular parathyroid and other 5 tissue types. *$p < 0.05$* is labeled as significant, *$p = 0.01$* and *$p = 0.001$* are also marked for reference.

The classification of hypercellular parathyroid was evaluated on 3 data sets with a different number of features: DOCI value from the 405 LPF channel; DOCI values from all 8 filter channels; DOCI values from all 8 filter channels and normalized intensity values from all 7 BPF channels. Three classifier models were evaluated: LR, KNN (k=11) and ANN (activation function: ReLU). Table 5.2 presents the classification results on the 3 data sets, the sensitivity and specificity of each classifier model are displayed in the table. With more features included as the input, the classification performance improved and eventually reached 100% sensitivity and 98.8% specificity with the logistic regression classifier. Figure 5.6 shows the receiver operating characteristic (ROC) curves for comparisons between different classifier models on different data sets.

Table 5.2. Classification Performance of 3 Classifier Models on 3 Data Sets[a]

Features (n)[b]	Model		
	LR	KNN	ANN
405 nm LPF channel DOCI (1)	80.6% / 94.0%	74.2% / 91.7%	67.7% / 95.2%
All 8 filter channels DOCI (8)	90.3% / 95.2%	80.6% / 94.0%	87.1% / 96.4%
All 8 filter channels DOCI & all 7 BPF channels normalized intensity (15)	100% / 98.8%	83.9% / 94.0%	93.5% / 96.4%

[a]The two percentages in each cell are sensitivity and specificity, respectively.

[b]n: number of features.

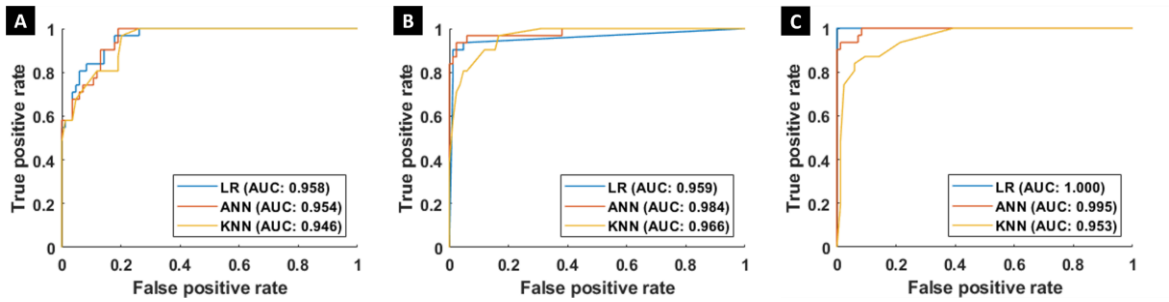

Figure 5.6 Receiver operating characteristic (ROC) curves for the 3 classifier models on: (A) 405 nm LPF channel DOCI value data set; (B) All 8 filter channels DOCI value data set; (C) All 8 filter channels DOCI value & all 7 BPF channels normalized intensity value data set. AUC: area under the curve.

5.4. Discussion

The variable location and indistinct external features of parathyroid glands can make their intraoperative identification challenging during parathyroidectomies. While inadequate removal of a diseased gland results in a prolonged surgery or reoperation, inadvertent removal of normal parathyroid glands results in clinical hypocalcemia [78]. The results presented in this study demonstrate that DOCI can be used as an adjunct diagnostic method to effectively distinguish hypercellular parathyroid glands from normal parathyroid glands and adjacent tissues, including, thyroid, thymus, and lymph nodes.

Previous publications have identified biologically relevant endogenous fluorophores that produce the lifetime contrast differences in tissues. The most notable fluorophores include NADH, FAD, elastin, and collagen [36]. The DOCI system principally characterizes lifetime by computing the ratio between the aggregate fluorescence decay intensity and the aggregate fluorescence steady-state intensity, thus allowing us to discriminate tissues based on their unique composition.

Across 8 different spectral channels, hypercellular parathyroid tissue was shown to have lower DOCI values when compared with normal parathyroid, thyroid, thymus, lymph node and

adipose tissue. The observed relationship of DOCI value between parathyroid tissue and other tissue types is concordant with previous publications and reported fluorescence lifetime data [22, 79]. Throughout all spectrally gated channels, there is an increasing trend among the DOCI values of hypercellular parathyroid, normal parathyroid and adipose tissue.

Histologically, normal parathyroid gland is composed mainly of chief cells and adipocytes with thin fibrous septa dividing the gland into lobules, while hypercellular parathyroid is usually characterized by chief cell proliferation and absent or reduced stromal adipocytes [80]. It is likely the DOCI value difference between hypercellular parathyroid, normal parathyroid and adipose tissue may be related to the change in the ratio between chief cells and adipocytes. Furthermore, the increased metabolic demand in the development of hypercellular parathyroid vs normal would potentially favor free NADH (lifetime 0.4ns) verses parathyroid with oxidative phosphorylation or bound NADH (lifetime 1 to 5ns), whereas fat stores retinol, a fluorescent compound with a 12 ns lifetime when bound [81]. This pattern of hypercellular parathyroid, normal parathyroid and fat having the shortest, intermediate, and longest lifetime respectively is also supported within our DOCI data (Figure 5.2)**.**

Since the DOCI calculation is formulated from the intensity image captured at steady state, decay state and background, the fluorescence intensity information can also be used as an input feature of the classifier to discriminate tissues or potentially fluorophores. Our previous works [78, 82-84] solely investigated the DOCI values. However here we demonstrate that adding the steady state fluorescent information with DOCI values provided a more robust AI training module. For the 2-class classification of hypercellular parathyroid against other tissue types, we observed pronounced improvement in classification performance after normalized steady-state fluorescence intensity was added as input for all three classifier models (Table 5.2). Specifically, the highest

sensitivity (100%) and specificity (98.8%) were from the logistic regression classifier trained on the comprehensive features from combined DOCI and normalized steady-state fluorescence intensity data, the addition of fluorescence intensity information helped increase 9.7% and 3.6% in sensitivity and specificity, respectively. The LR classifier model was the best fitting model, it suggests that the predicted probability of tissue type is a linear combination of multi-channel DOCI value and fluorescence intensity features. Benefited from the unique working principle of DOCI [78], the acquisition of fluorescence emission profile is an indispensable step. In other words, from the perspective of data acquisition, there is zero extra cost to add the steady-state fluorescence intensity data to data analysis. Data processing will add additional calculations, but because the overall data processing calculations are already very light, the additional calculation costs are affordable or even negligible.

DOCI imaging is rapid, it takes less than 2 seconds to acquire DOCI contrast across a wide field image. DOCI utilizes a non-ionizing light source and builds contrast based on a sample's autofluorescence. It allows for rapid and non-invasive probing of tissue composition, which makes it a reliable intraoperative adjunct imaging technique to find the location of hypercellular parathyroid glands. This study provided us with the feasibility that the DOCI technique can be used for hypercellular parathyroid localization.

Patient prognosis depends heavily on complete resection of the involved parathyroid glands. DOCI is a compact, user friendly, non-invasive, clinically relevant imaging system that can precisely detect parathyroid tissue and differentiate normal from hypercellular diseased glands. The DOCI system is clinically relevant and easily operable by clinical providers to better inform and improve the treatment of patients undergoing thyroid, parathyroid and neck surgery.

5.5. Conclusion

Advances in intraoperative parathyroid localization and diagnostics continue to be a major need in our treatment of patients with thyroid and parathyroid disease. The small size, variable location, and indistinct external features of parathyroid glands can make their identification quite challenging intraoperatively. Patient prognosis depends heavily on complete resection of the involved parathyroid glands. There remains a large gap in this area and improvement of intraoperative detection will be a key to optimize treatment and patient outcomes.

In this study, we demonstrated that DOCI can discriminate between a variety of tissues and with the incorporation of AI techniques, allows DOCI to specifically identify hypercellular parathyroid with greater confidence. We show statistically significant differences in DOCI values and normalized steady-state intensity values between hypercellular parathyroid glands, normal parathyroid glands, and adjacent tissues. We observed a best performance of 100% sensitivity and 98.8% specificity on classification of hypercellular parathyroid. This work lays the foundation for future *in vivo* research using DOCI as the basis of intraoperative instruments to guide the localization of parathyroid glands, and then to determine if they are normal or hypercellular. In the future, DOCI can serve as a platform for the early detection of specific tissue types throughout the body.

Chapter 6. Margin Detection for Oral and Oropharyngeal Squamous Cell Carcinoma

6.1. Introduction

Head and neck cancer is the sixth most common cancer in the world (Figure 6.1 (a)) [85], it usually begins in the squamous cells from the mucosal surfaces in the oral cavity, pharynx, and larynx, also known as HNSCC. HNSCC treatment can include surgery, radiation therapy, chemotherapy, targeted therapy, immunotherapy, or a combination of treatments. The primary aim of surgical management of HNSCC is adequate resection of the tumor and negative margins. The most common definition of a negative margin is a clear >5 mm pathologic margin on microscopic evaluation [86]. Positive surgical margins adversely affect patient outcomes, increasing local recurrence rates and mortality by 90% [87]. Excessively wide margins with over-resection of healthy tissue, however, increases patient morbidity including speech and swallowing deficits. Currently, intraoperative margins are assessed through a combination of visual cues, palpation, and surgeon experience as well as frozen section. Intraoperative imaging techniques under investigation frequently utilize nonspecific contrast agents such as ICG which have variable specificity and can result in adverse effects including anaphylaxis [69, 88].

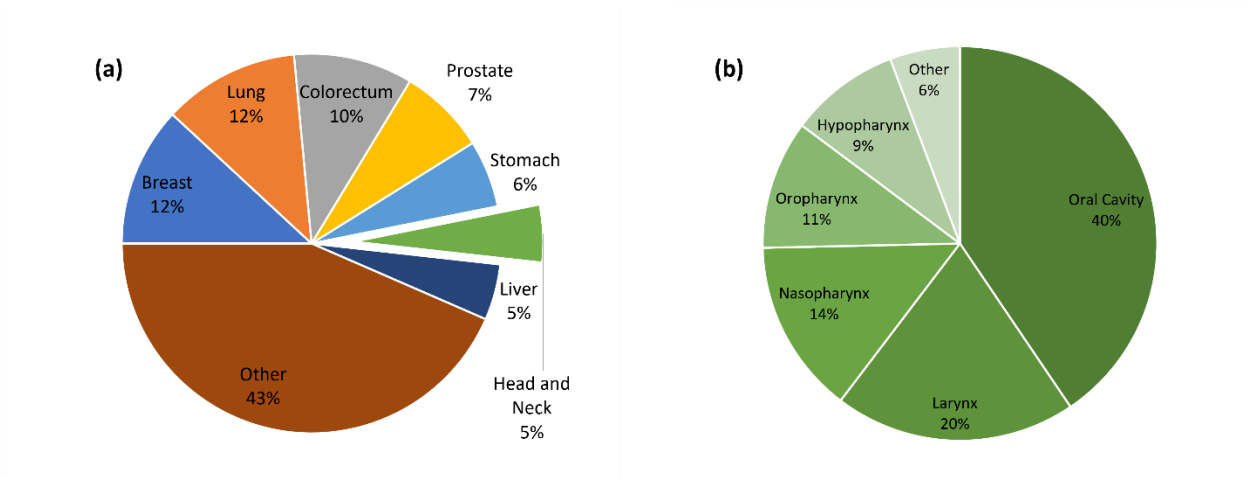

Figure 6.1 (a) Estimated incidence of all 18094716 cancer cases worldwide in 2020. (b) Estimated incidence of all 931931 head and neck cancer cases worldwide in 2020, cases are grouped by subsite. Data plotted from GLOBOCAN 2020 data. [85]

In this chapter, we demonstrate that DOCI (1) can differentiate malignant tissue from adjacent tissue in oropharyngeal and oral cavity cancers, (2) can accurately identify margins of oral cavity squamous cell carcinoma (OCSCC) intraoperatively, and (3) has the potential to identify margins of oropharyngeal squamous cell carcinoma (OPSCC) *in vivo* using an endoscopic configuration.

6.2. *Ex Vivo* Tissue Differentiation

6.2.1. Protocol For *Ex Vivo* Data Collection

The *ex vivo* study is approved by the UCLA IRB, eligible patients are those scheduled to receive HNSCC surgeries at Ronald Reagan UCLA Medical Center. The protocol for DOCI on HNSCC tissue specimens is illustrated in Figure 6.2. There are 5 steps in total:

1. The specimen is collected immediately after excision and discharged from the operating room, ideally with tumor-negative margins maintained, thus requiring sectioning to expose tumor tissue. In compliance with the clinical pathological examination protocol, the

specimen is sectioned by a pathologist's assistant to obtain millimeter-thick slices, on which the tumor and adjacent tissues are exposed.

2. Perform *ex vivo* DOCI measurement on each tissue slice, for each filter channel, the exposure time is 0.5 s.
3. After imaging, frozen section is performed on the tissue slice to obtain a 5 μm thick section (standard H&E (hematoxylin and eosin) stained slide with coverslip) and a 20 μm thick section (unstained, airdried slide and without coverslip) from each tissue slice.
4. The 20 μm thick unstained section is scanned with DOCI followed by immediate H&E staining, due to reduced signal intensity during DOCI, a longer exposure time or multiple integrations is applied to the measurement.
5. The frozen histology slides are digitized on a digital pathology slide scanner to obtain histopathological images for future co-registration.

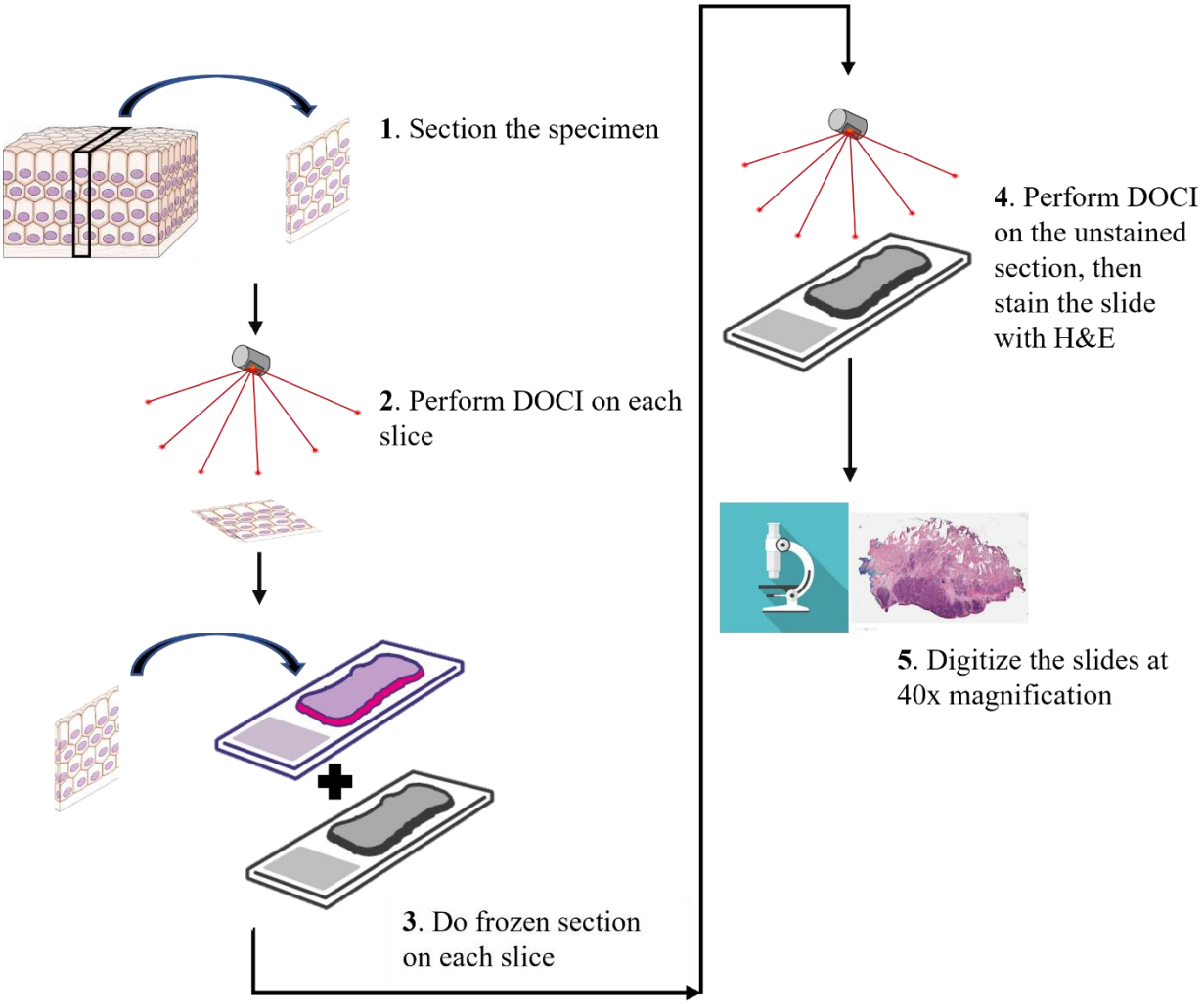

Figure 6.2 Protocol for DOCI on HNSCC tissue specimens

For each specimen, DOCI measurement is done twice individually on (1) the fresh tissue slice with a thickness of around 3 mm to 5 mm, and (2) the frozen section tissue with a thickness of 20 μm. The fresh tissue slice imaging provides the core *ex vivo* data in the study, and the frozen section imaging helps us to better understand the correlation between the fresh tissue DOCI images and the histopathological images. For the frozen section tissue, the DOCI images should have one-to-one match with the histology, because it is first imaged with DOCI followed by H&E staining immediately, and the 20 μm tissue thickness allows the UV excitation light to penetrate it completely [89]. The fresh tissue slice is too thick for the UV excitation light to penetrate, therefore

the histopathological information embedded in the DOCI images may differ from information from corresponding clinical standard 5 μm thick H&E slides.

6.2.2. *Ex Vivo* OPSCC Imaging

While the incidence of traditional carcinogen-induced HNSCC has continued to decline, the last thirty years have seen a significant increase in HNSCC in otherwise healthy populations driven primarily by a rise in human papilloma virus (HPV) associated OPSCC. [90, 91] HPV is now implicated in 70% of all OPSCC, and in 2009, the incidence of OPSCC in men surpassed cervical cancer in women. [92, 93] Over the past decade, transoral robotic surgery (TORS) has become a first-line treatment for early-stage OPSCC with over 90% 2-year locoregional control rate and overall survival. [94]

Patients with OPSCC undergoing surgical resection at UCLA Ronald Reagan Medical Center were identified and consented for the study. Immediately after surgical resection, the malignant tonsil as well as the contralateral tonsil were sectioned into thin slices, and the gross specimens were imaged using the DOCI *ex vivo* system. The gross specimen then underwent frozen histologic sectioning. A head and neck pathologist annotated the frozen histology slides for salivary glands, connective tissue, tonsillar crypts, and cancer. The annotations were then co-registered and transferred to the DOCI images.

OPSCC and normal contralateral tonsils from 10 patients (7 male, 3 female) were collected and imaged for DOCI. Patient's ages ranged from 36 to 87. All malignancies were noted on pathology to be p16+ squamous cell carcinoma. 7 out of 10 patients had T1 or T2 stage malignancies and three patients had T3 malignancies.

The histopathological information that DOCI captured from fresh tissue and frozen section tissue is in conformity with H&E-stained histology (Figure 6.3). The gross specimen (Figure 6.3A)

is a lymph node section with metastatic OPSCC, malignant (blue), connective (yellow) and adipose (red) tissues can be clearly found from the fresh tissue DOCI image (Figure 6.3C) and the frozen section tissue DOCI image (Figure 6.3D). The frozen section tissue DOCI image has more fine details that can also be observed from the frozen histology (Figure 6.3B), while areas of each tissue type are more homogenous in the fresh tissue DOCI image.

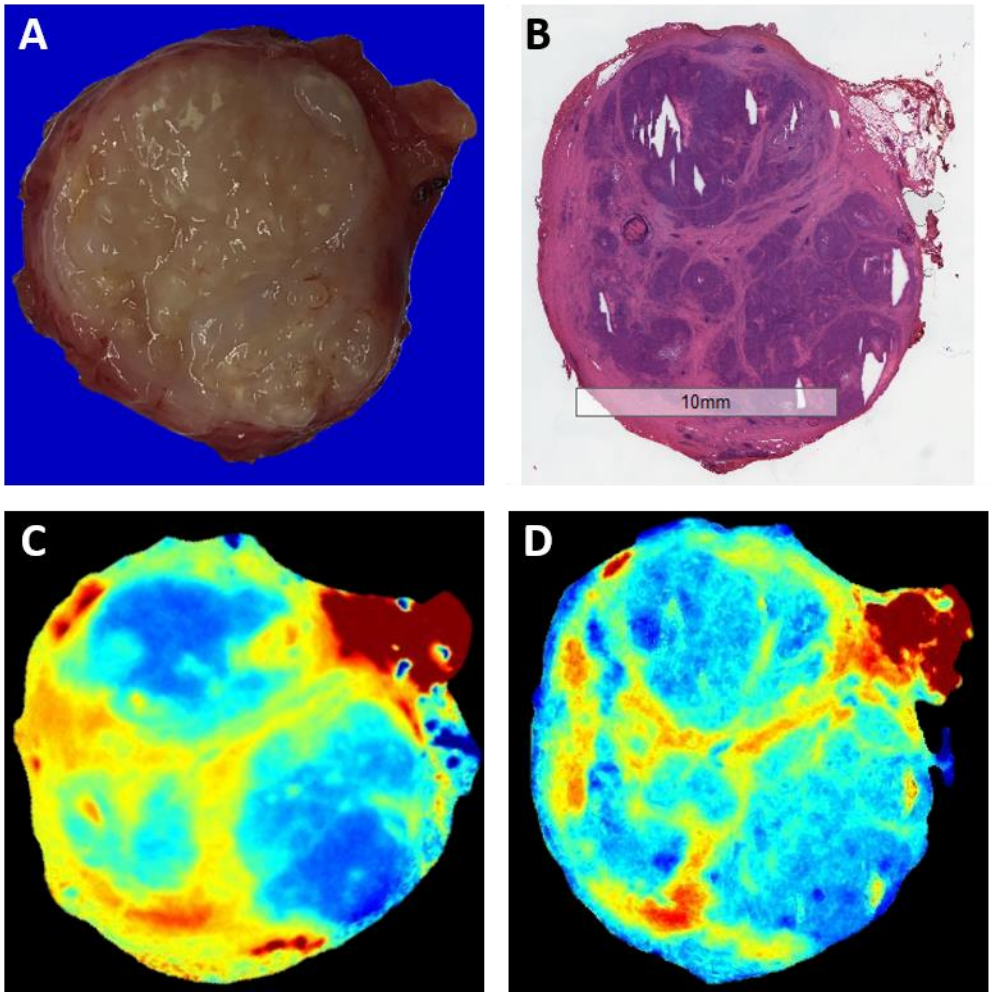

Figure 6.3 Comparison of DOCI data between fresh tissue and frozen section tissue. (A) Gross specimen. (B) Frozen section histology. (C) DOCI image of fresh tissue. (D) DOCI image of frozen section tissue, the frozen section tissue was first scanned with DOCI and then stained with H&E to provide (B).

The consistency between frozen section tissue DOCI image and frozen histology demonstrated DOCI captures histopathological information with high precision. The difference between fresh tissue DOCI image and froze histology was caused by 3 factors: the limited performance of focus of the DOCI system, the limited performance of penetration of the UV light, and the histological difference between tissues with different distance to the surface. In the following analysis, we choose fresh tissue DOCI data because it is closer to the real application scenario, and the most important thing is that fresh tissue slices have enough thickness.

OPSCC specimens imaged with DOCI revealed significant difference in fluorescence lifetime and intensity of healthy tissue compared to cancer (Figure 6.4). Immediately after TORS assisted resection of OPSCC of the palatine tonsil, the gross specimen (Figure 6.4 A) was imaged using DOCI, inking procedure was applied to the specimen for pathological orientation purpose. DOCI images were acquired in <2 seconds per channel and with a wide field of view (6.5 cm^2, Figure 6.4C). Frozen histology slides (Figure 6.4 B) were annotated for healthy and malignant tissue types and were found to be concordant with DOCI imaging (Figure 6.4 B, Figure 6.4 C), the areas affected by inking were avoided during annotation. The DOCI values corresponding to the regions of interest (ROI) demonstrated statistically significant differences between tonsillar crypt, salivary gland, and connective tissues compared to OPSCC (Figure 6.4 D). In the 405 nm BPF channel, tumor has a lower DOCI value compared to tonsillar crypts, salivary gland tissues, and connective tissue.

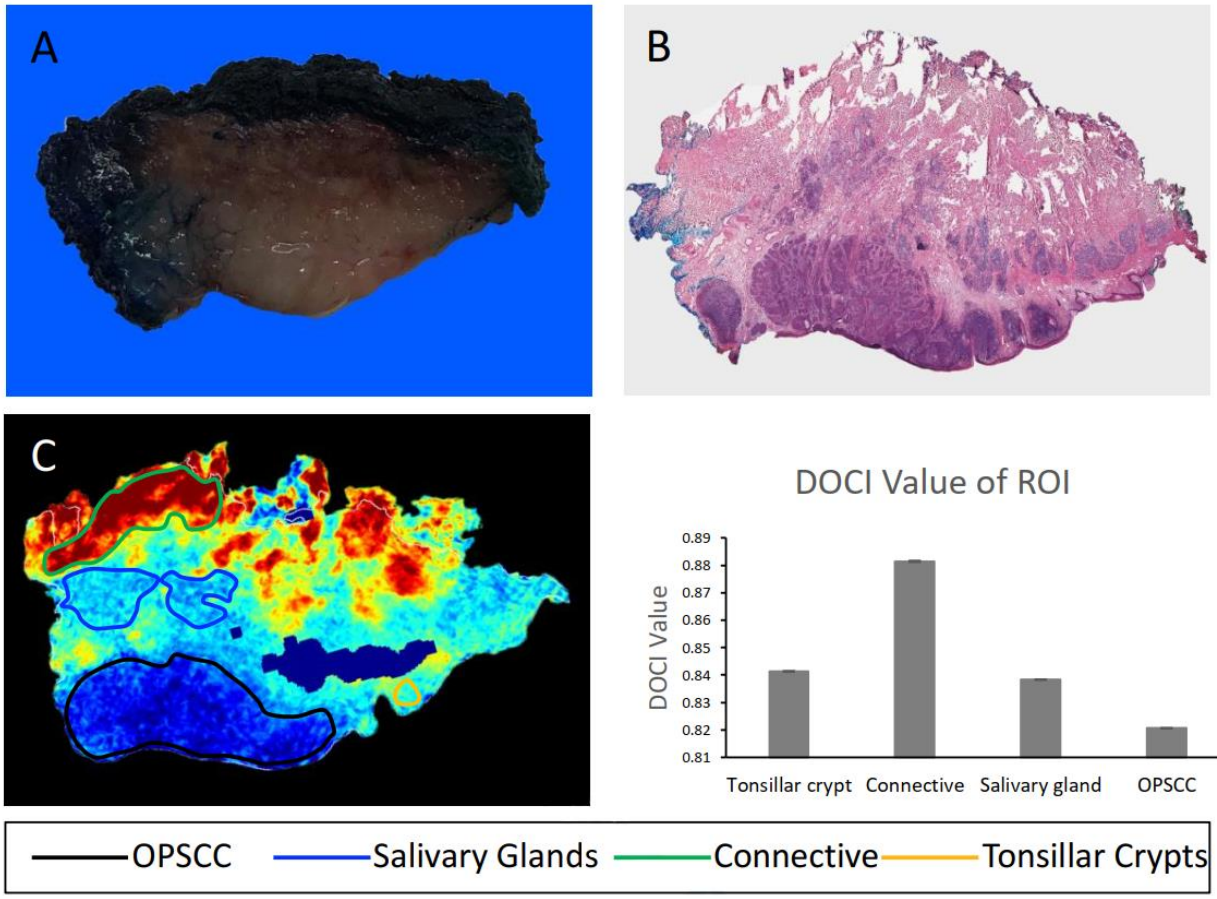

Figure 6.4 DOCI identifies margins between OPSCC and adjacent healthy tissue. (A) Gross specimen. (B) Frozen section histology. (C) 405 nm BPF channel DOCI imaging with annotated ROIs. (D) DOCI value of ROIs depicted in Figure 1C. OPSCC: oropharyngeal squamous cell carcinoma. BPF: bandpass filter. ROI: region of interest.

DOCI values corresponding to connective tissue, tonsillar crypts, and OPSCC were analyzed in 9 filter channels (n=10, Figure 6.5). Salivary gland tissue was not present in all specimens and was not sufficiently powered to provide meaningful analysis, therefore was not included here. Healthy tissues have distinct trends across 9 spectral channels relative to OPSCC (p<0.01). p-values of connective tissue and tonsillar crypts relative to OPSCC are plotted in Figure 6.5B in a negative log10 scale, where $p < 0.01$ is defined as significance. Overall, BPFs of the

middle wavelengths (465 nm to 542 nm) provided the greatest contrast between cancer and healthy tissues.

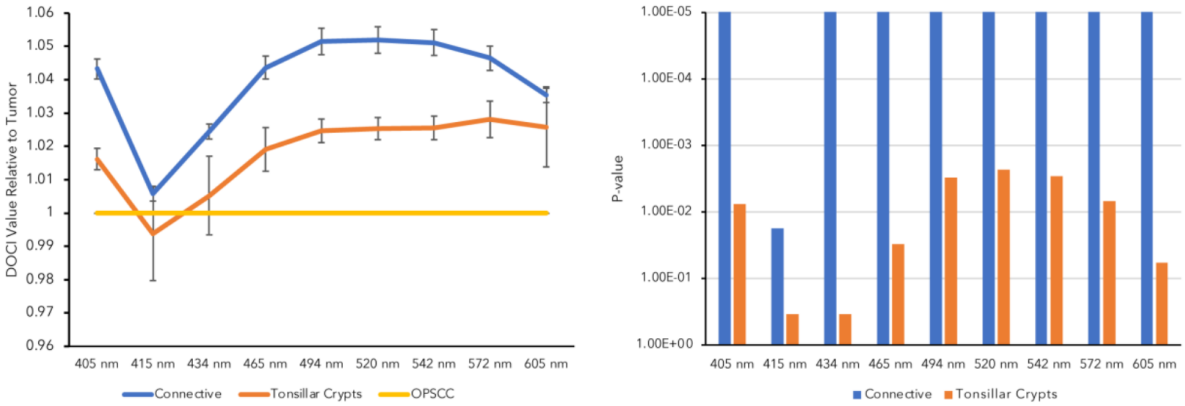

Figure 6.5 (A) DOCI values of healthy tissues relative to OPSCC across 9 spectral channels (n=10). (B) P-values of healthy tissues compared to OPSCC across 9 spectral channels. OPSCC: Oropharyngeal squamous cell carcinoma.

6.2.3. *Ex Vivo* OCSCC Imaging

OCSCC accounts for more than 90% of oral cavity cancer which holds the sixteenth position in malignancy worldwide [95, 96]. The contributing factors for the development of OCSCC include consumption of tobacco and alcohol, and exposure to HPV [97]. By definition, OCSCC includes subsites of buccal mucosa, floor of mouth, anterior tongue, alveolar rights, retromolar trigone, hard palate and inner part of lips.

12 tissue specimens from 11 patients with stages T2-T4a OCSCC underwent surgical excision and DOCI imaging. Specimens collected from various oral cavity subsites including oral tongue, buccal mucosa, and floor of mouth were first imaged using the DOCI system followed by histologic sectioning. A head and neck pathologist annotated the histology slides for connective tissue, adipose tissue, skin or mucosal epithelium, and OCSCC. Annotations were transferred and

co-registered with DOCI images, and signature emissions were compared between adjacent healthy and malignant tissue.

Irrespective of the tumor subsite, DOCI images clearly delineate the margins between cancer and healthy adjacent tissues in all 12 specimens (Figure 6.6 A). Frozen histology annotations of both malignant and healthy tissue are concordant with DOCI imaging. Tumor margins can be determined in multiple subsites, including oral tongue, buccal mucosa, and the floor of mouth (Figure 6.6 A). Epithelial, adipose, and connective tissues have significantly higher DOCI values compared to OCSCC (Figure 6.6 B, p=0.02, n=12). In contrast, muscle displayed lower DOCI values relative to tumor (p=0.02).

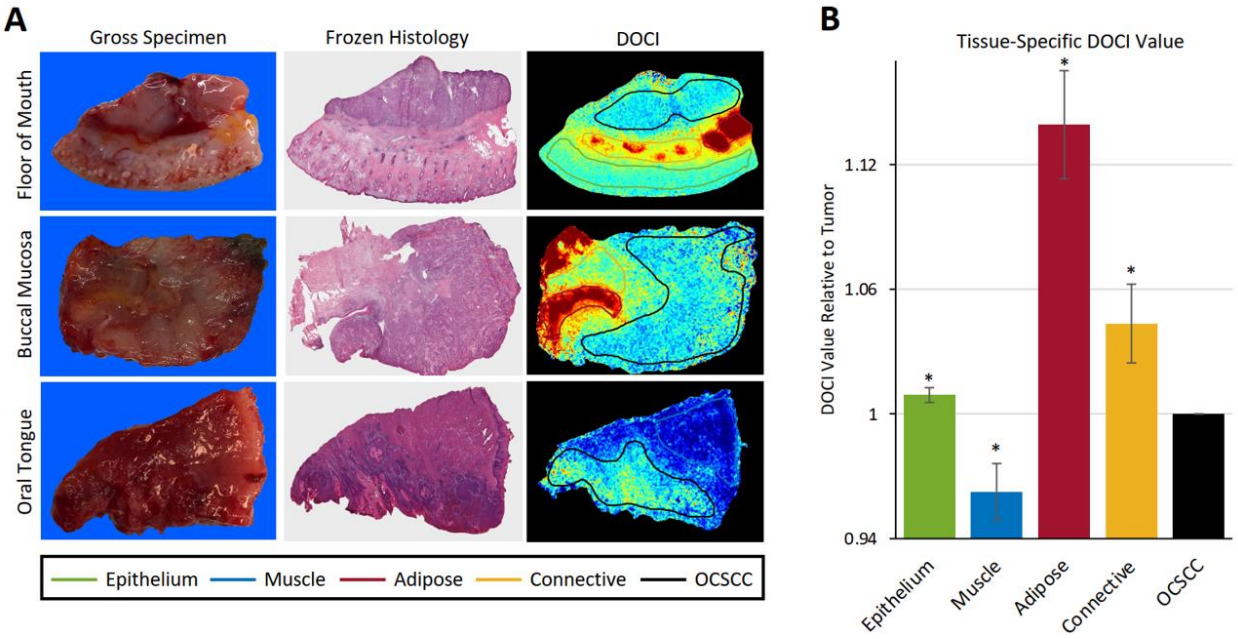

Figure 6.6 Intraoperative Dynamic Optical Contrast Imaging to Detect Margins for Oral Cavity Squamous Cell Carcinoma. (A) Gross specimens from the floor of mouth, buccal mucosa, and oral tongue were imaged with DOCI. Frozen histology from gross specimens were annotated for cancer, epithelial, connective, adipose and muscle tissue and co-registered with DOCI images. DOCI delineates margins that are concordant with histology. (B) Healthy tissues have statistically significant DOCI values compared to tumor (n=12). *p<0.05

6.2.4. Discussion

The results from OPSCC and OCSCC have shown that the SCC tissue can be differentiated from adjacent healthy tissues via DOCI. Epithelium tissue presented least distinctive DOCI features compared to SCC tissue, we think this is because SCC usually develops from the epithelium, and for HPV positive OPSCC, the SCC usually develops from the tonsillar crypt epithelium. Depending on the grading of SCC, the cancer cells may retain characteristics of normal squamous epithelium. Although remains to be explored, this relationship may explain why SCC and epithelium tissue exhibit similar DOCI signatures.

6.3. *In Vivo* Margin Detection

We introduced in chapter 2 the design of *in vivo* DOCI system, the first implementation is based on a Canon EF-S 55-250mm F4-5.6 IS lens which gives us descent depth-of-view. The imaging system is mounted on a heavy-duty monitor arm, a rotation stage is used to connect the system and the arm, this configuration allows free positioning of the system. However, limited working distance and bulky form factor make this system only for skin and oral cavity measurements. To get to oropharyngeal site, an endoscope-based system is needed. In this section, we first demonstrate the camera lens-based *in vivo* DOCI system can delineate margins for OCSCC, and second we show the concept of using our endoscope-based prototype for OPSCC margin detection.

6.3.1. *In Vivo* OCSCC Margin Detection

After validating that DOCI can delineate margins *ex vivo*, four patients with OCSCC involving the oral tongue, inferior alveolar ridge, and floor of mouth underwent intraoperative, *in vivo* DOCI imaging to help determine surgical margins. The *in vivo* system with camera lens and 90° incident illumination (Figure 2.7(b)) was used for measurement, for better image quality, we did multiple

accumulations (10-40) each with exposure time of 0.5 s. The entire patient preparation, system positioning, and measurement operations took on average 5 minutes.

Figure 6.7 depicts an 81-year-old female who underwent DOCI imaging of the inferior alveolar ridge and floor of mouth prior to mandibulectomy for OCSCC. In all patients, cancer has a lower DOCI value (blue) compared to the surrounding normal mucosa (n=4, p=0.007). Permanent histopathology confirms DOCI findings of invasive SCC surrounded by normal mucosa. An overlay of the DOCI and white light (WL) images provides the surgeon with additional information, aiding in cancer resection.

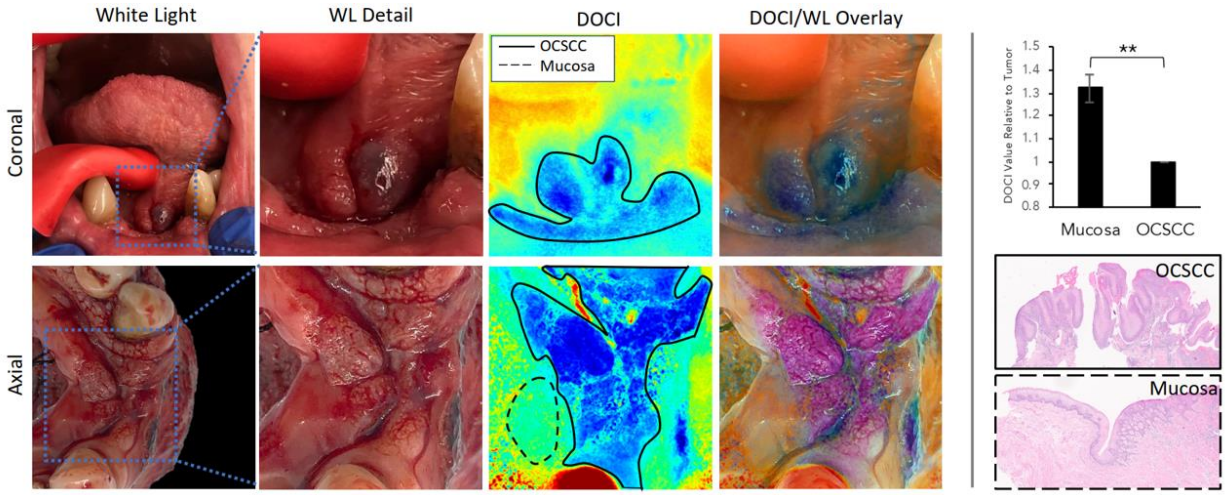

Figure 6.7 Intraoperative, *in vivo* DOCI images of a patient with OCSCC of the alveolar ridge and floor of mouth demonstrates clear margins between OCSCC and healthy mucosa, confirmed with histopathology. DOCI images overlaid with White Light (WL) images provides the surgeon with additional information regarding margins. Mucosa has a significantly higher DOCI value compared to tumor. **p<0.01

6.3.2. *In Vivo* OPSCC Margin Detection

One patient with OPSCC involving the palatine tonsil underwent intraoperative, *in vivo* DOCI imaging to help determine surgical margins, the *in vivo* system with endoscope and imaging fiber bundle (Figure 3.5 (c)) was used for measurement. Before imaging, the endoscope was first

detached from the system and put in the best position by a head and neck surgeon, a robotic endoscope holder was used to fix the position of the endoscope. Then, the imaging fiber bundle was connected to the eyepiece of the endoscope for measurement. With previous experience of endoscopic imaging on animals, we set the exposure time to 2.5s and did 30 accumulations.

Though with a low resolution, the DOCI image (Figure 6.8) still depicts the margin between the OPSCC and healthy oropharyngeal wall tissues. The low image quality is mainly resulted from two aspects: excitation and emission. The excitation UV light was not efficiently transmitted through the endoscope, as the internal fiber optics was not optimized for UV transmission. The emission light also suffered significant loss through the endoscope and the imaging fiber bundle. Next step on the endoscopic system development should focus on the improvement of these two aspects.

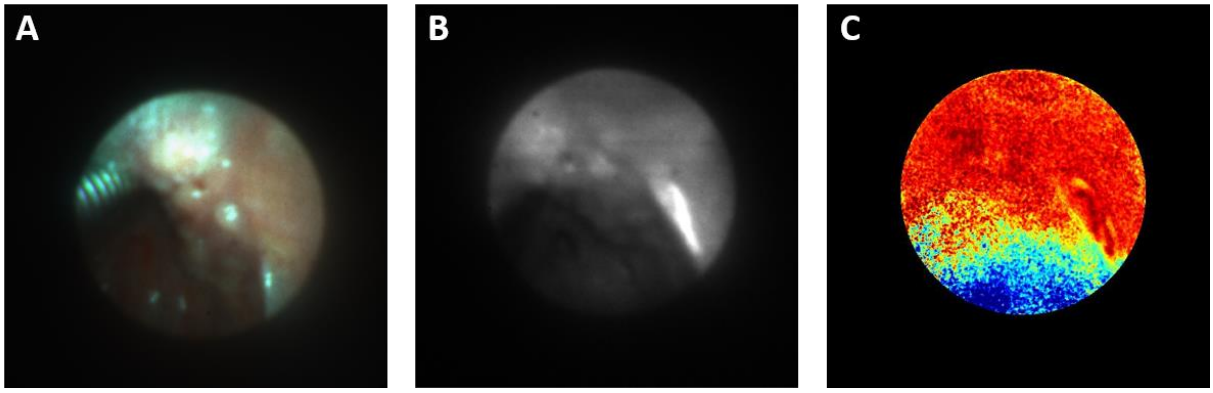

Figure 6.8 Intraoperative, *in vivo* DOCI images of a patient with OPSCC of the palatine tonsil demonstrates margin between OPSCC and healthy oropharyngeal wall. (A) White light image. (B) 405 nm BPF channel fluorescent intensity image. (C) 405 nm BPF channel DOCI image.

6.4. Conclusion

In this chapter, we explored the margin detection for OCSCC and OPSCC. From the *ex vivo* measurements, we found that the SCC tissue can be differentiated from adjacent healthy tissues

via DOCI for both OPSCC and OCSCC. Results from *in vivo* OCSCC measurements showed that DOCI captured clear margins between OCSCC and healthy mucosa, confirmed with histopathology. *In vivo* OCSCC measurement results showed that DOCI was able to differentiate between OPSCC and healthy oropharyngeal wall tissues, but a better image quality may be needed.

Chapter 7. Conclusion and Future Work

7.1. Conclusion

In this dissertation, we discussed recent advancements of the DOCI technique and its applications in head and neck surgical disciplines. As a relative fluorescence lifetime imaging technique, DOCI is based on the novel and rapid measurement of the specific temporal decay of tissue autofluorescence that allows for the generation of clinically relevant contrast over a large field of view in both macroscopic and cluttered, *in vivo* surgical fields. Compared with conventional FLIM methods, DOCI provides relative fluorescence lifetime images with extremely short acquisition and computational times.

Regarding DOCI system design and implementation, the current implementation of 3 iterations enables high-quality data acquisition from ex vivo samples and in vivo sites, systems were validated and characterized to ensure high-consistency measurement. Integrated system control makes operating system simple. However, current implementation has several limitations. First, the excitation light power still has room to improve according to the safety limit of UV radiation, for endoscopic application we need much more light to compensate for the light loss in transmission. Second, limited by instrumentation and system design, the current generation of DOCI system can only achieve 0.6 fps of DOCI video at 16-bit 1024x1024, which is inadequate for the human brain to create visual continuity. Third, for endoscopic imaging, the data quality awaits to be improved. Last, although the current *in vivo* system implementation has the capability to handle most of the head and neck surgical measurements, it requires noticeable amount of strength from the user to maneuver the system.

The system was used in several head and neck surgical applications. Data from animal tissue shows that DOCI accurately differentiates tissue type and clearly delineate margins from mouse cancer models. Results from *ex vivo* experiments demonstrate that DOCI enables sensitive and specific mapping of hypercellular parathyroid gland. It is demonstrated that DOCI allows for real-time visualization and accurate delineation of OCSCC and adjacent healthy tissue, and that DOCI can be used in to clearly delineate margins between oropharyngeal cancer and surrounding healthy tissue.

7.2. Future work

7.2.1. System Upgrade For *In Vivo* Imaging

Our current *in vivo* camera lens DOCI system requires the operator to manually focus the camera system on the target area, the bulky camera system weighs 20 pounds and is mounted on a monitor arm. It is strenuous but requires delicate manipulation, the degree of completion is determined from the live video feedback on the computer monitor by checking if the site of interest is in focus. To simplify the manipulation process, the iCCD camera and the filter wheel can be taken off from the arm, leaving only the objective lens and illumination outlet on the arm, thus greatly reduce the weight on the arm.

On the other hand, auxiliary positioning solutions, such as laser guided positioning, contrast detection assisted focusing, and motorized motion control, etc. can be integrated into the system. Manually focusing the camera through grayscale video is difficult, it requires the operator to adjust the position repeatedly to find the best position, yet the best position is subjective to the operator. Laser guidance can greatly speed up the process of moving the system to roughly in focus, fine grade focusing can be achieved by calculating the contrast on computer and finding the

numerically best spot. With motorized motion control, the system positioning can be done through the computer and positioning can be more accurate.

7.2.2. Towards Real-Time DOCI Video With Moderate Frame Rate

Clinical fluorescence imaging systems such as Spy (Stryker) and Rubina (Karl Storz) typically provide 1080p or higher quality live video at 60 frames per second (fps). Limited by instrumentation and system design, the current generation of DOCI system can only achieve 0.6 fps of DOCI video at 16-bit 1024x1024, which is inadequate for the human brain to create visual continuity. The iCCD camera used in our system has an USB 2.0 interface that provides a maximum data transmission rate of 60 MB/s, considering the size of a 16-bit 1024x1024 image is 2 MB and 3 images are acquired from the camera to produce one DOCI image, theoretically the maximum DOCI video rate is 20 fps. The bottleneck is the readout of image from the internal data buffer, the maximum readout speed is 5MHz at 16-bit, resulting in a maximum nominal frame rate of 4.2 fps for regular 1024x1024 video and 7.3 fps for regular 512x512 video. Considering the camera acquires 3 images in a row to produce one frame of DOCI, the frame rate of the 1024x1024 DOCI video drops to <1 fps.

Alternative camera models with higher frame rate are available, for example, the ANDOR iStar sCMOS camera series have a frame rate of 52 fps at 16-bit 2048x2048 and 203 fps at 16-bit 512x512. In addition to instrument upgrades, we can also improve the frame rate by using a different system design approach. Currently, the 3 images (steady-state, decay-state, and background) used to calculate 1 DOCI image are acquired separately from different emission pulsing cycles. If the 3 images can be acquired simultaneously from the same pulsing cycles, the overall acquisition time can be reduced by 66.7%, and motion correction would be no longer necessary. For example, the image can be split and relayed to 3 different sub-areas of the image

sensor, each with different optical delay, such as travelling through optical fibers with different lengths. Another way is to use relay the image to 3 identical cameras, each camera with a different delay setting. However, both solutions would greatly increase the budget and system complexity, a comprehensive assessment is required.

7.2.3. Cross-Platform Data Amalgamation

Cross-platform data amalgamation is necessary to ensure the same fluorescence activity measured from different DOCI system platforms yields consistent DOCI values within acceptable error limits. The measurement error between different systems arises from performance variations of every functional part of the system, among them the LED driver board brings the largest error. In our system, the UV-LED is driven to generate highly stable light pulses with both rising and falling edges constrained at nanosecond level, which is not the regular way to drive LEDs. From all LED products we have tried, none of them were designed for this type of application, therefore the LEDs' temporal response performance varies noticeably. To match the emission triggered by different excitation pulses, one possible way is to use convolution methods to estimate the transformation function relative to the same standard, the transformation function is applied to DOCI calculation to produce results with less error.

References

[1] D. J. Kaplan, J. N. Patel, F. A. Liporace, and R. S. Yoon, "Intraoperative radiation safety in orthopaedics: a review of the ALARA (As low as reasonably achievable) principle," *Patient Safety in Surgery,* vol. 10, no. 1, p. 27, 2016/12/12 2016, doi: 10.1186/s13037-016-0115-8.

[2] A. Šteňo, J. Buvala, V. Babková, A. Kiss, D. Toma, and A. Lysak, "Current Limitations of Intraoperative Ultrasound in Brain Tumor Surgery," (in eng), *Front Oncol,* vol. 11, pp. 659048-659048, 2021, doi: 10.3389/fonc.2021.659048.

[3] S. Gioux, H. S. Choi, and J. V. Frangioni, "Image-guided surgery using invisible near-infrared light: fundamentals of clinical translation," (in eng), *Mol Imaging,* vol. 9, no. 5, pp. 237-255, 2010.

[4] S. C. A. Steens *et al.*, "Evaluation of tongue squamous cell carcinoma resection margins using ex-vivo MR," (in eng), *Int J Comput Assist Radiol Surg,* vol. 12, no. 5, pp. 821-828, 2017, doi: 10.1007/s11548-017-1524-6.

[5] B. Z. Dashevsky *et al.*, "The Potential of High Resolution Magnetic Resonance Microscopy in the Pathologic Analysis of Resected Breast and Lymph Tissue," *Scientific Reports,* vol. 5, no. 1, p. 17435, 2015/12/07 2015, doi: 10.1038/srep17435.

[6] F. A. Jolesz, *Intraoperative imaging and image-guided therapy*. Springer Science & Business Media, 2014.

[7] C. M. C. Tempany *et al.*, "Multimodal imaging for improved diagnosis and treatment of cancers," *Cancer,* https://doi.org/10.1002/cncr.29012 vol. 121, no. 6, pp. 817-827, 2015/03/15 2015, doi: https://doi.org/10.1002/cncr.29012.

[8] W. M. Benjamin, M. M. David, III, W. P. Brian, D. P. Keith, A. W. M. D. Wendy, and J. B. M. D. Richard, "Review of methods for intraoperative margin detection for breast conserving surgery," *Journal of Biomedical Optics,* vol. 23, no. 10, pp. 1-19, 10/1 2018, doi: 10.1117/1.JBO.23.10.100901.

[9] Y. Zhang *et al.*, "Applications of hyperspectral imaging in the detection and diagnosis of solid tumors," *Translational Cancer Research,* vol. 9, no. 2, pp. 1265-1277, 2020.

[10] H. Martin *et al.*, "Cancer detection using hyperspectral imaging and evaluation of the superficial tumor margin variance with depth," in *Proc.SPIE*, 2019, vol. 10951, doi: 10.1117/12.2512985. [Online]. Available: https://doi.org/10.1117/12.2512985

[11] L. Guolan and F. Baowei, "Medical hyperspectral imaging: a review," *Journal of Biomedical Optics,* vol. 19, no. 1, pp. 1-24, 1/1 2014, doi: 10.1117/1.JBO.19.1.010901.

[12] M. Barberio *et al.*, "Intraoperative Guidance Using Hyperspectral Imaging: A Review for Surgeons," *Diagnostics,* vol. 11, no. 11, 2021, doi: 10.3390/diagnostics11112066.

[13] G. Succo, P. Garofalo, M. Fantini, V. Monticone, G. C. Abbona, and E. Crosetti, "Direct autofluorescence during CO2 laser surgery of the larynx: can it really help the surgeon?," *Acta Otorhinolaryngologica Italica,* vol. 34, no. 3, p. 174, 2014.

[14] J. D. Meier *et al.*, "Time-resolved laser-induced fluorescence spectroscopy as a diagnostic instrument in head and neck carcinoma," *Otolaryngology–Head and Neck Surgery,* vol. 142, no. 6, pp. 838-844, 2010/06/01 2010, doi: 10.1016/j.otohns.2010.02.005.

[15] J. A. Jo *et al.*, "In Vivo Simultaneous Morphological and Biochemical Optical Imaging of Oral Epithelial Cancer," *IEEE Transactions on Biomedical Engineering,* vol. 57, no. 10, pp. 2596-2599, 2010, doi: 10.1109/TBME.2010.2060485.

[16] Y. Sun *et al.*, "Endoscopic Fluorescence Lifetime Imaging for In Vivo Intraoperative Diagnosis of Oral Carcinoma," *Microscopy and Microanalysis,* vol. 19, no. 4, pp. 791-798, 2013, doi: 10.1017/S1431927613001530.

[17] E. Duran-Sierra *et al.*, "Clinical label-free biochemical and metabolic fluorescence lifetime endoscopic imaging of precancerous and cancerous oral lesions," *Oral Oncology,* vol. 105, p. 104635, 2020/06/01/ 2020, doi: https://doi.org/10.1016/j.oraloncology.2020.104635.

[18] M. Marsden *et al.*, "Intraoperative Margin Assessment in Oral and Oropharyngeal Cancer Using Label-Free Fluorescence Lifetime Imaging and Machine Learning," *IEEE Transactions on Biomedical Engineering,* vol. 68, no. 3, pp. 857-868, 2021, doi: 10.1109/TBME.2020.3010480.

[19] H. S. Yinghua *et al.*, "Fluorescence lifetime imaging microscopy for brain tumor image-guided surgery," *Journal of Biomedical Optics,* vol. 15, no. 5, pp. 1-5, 9/1 2010, doi: 10.1117/1.3486612.

[20] S. R. Kantelhardt *et al.*, "In vivo multiphoton tomography and fluorescence lifetime imaging of human brain tumor tissue," *Journal of Neuro-Oncology*, vol. 127, no. 3, pp. 473-482, 2016/05/01 2016, doi: 10.1007/s11060-016-2062-8.

[21] R. A. Romano, R. G. Teixeira Rosa, A. G. Salvio, J. A. Jo, and C. Kurachi, "Multispectral autofluorescence dermoscope for skin lesion assessment," *Photodiagnosis and Photodynamic Therapy*, vol. 30, p. 101704, 2020/06/01/ 2020, doi: https://doi.org/10.1016/j.pdpdt.2020.101704.

[22] M. Marsden, S. S. Weaver, L. Marcu, and M. J. Campbell, "Intraoperative Mapping of Parathyroid Glands Using Fluorescence Lifetime Imaging," *Journal of Surgical*

Research, vol. 265, pp. 42-48, 2021/09/01/ 2021, doi: https://doi.org/10.1016/j.jss.2021.03.023.

[23] J. E. Phipps, D. Gorpas, J. Unger, M. Darrow, R. J. Bold, and L. Marcu, "Automated detection of breast cancer in resected specimens with fluorescence lifetime imaging," *Physics in Medicine & Biology,* vol. 63, no. 1, p. 015003, 2017/12/14 2017, doi: 10.1088/1361-6560/aa983a.

[24] J. Unger *et al.,* "Real-time diagnosis and visualization of tumor margins in excised breast specimens using fluorescence lifetime imaging and machine learning," *Biomedical Optics Express,* vol. 11, no. 3, pp. 1216-1230, 2020/03/01 2020, doi: 10.1364/BOE.381358.

[25] L. Zhou *et al.,* "Metabolic Changes in Maternal and Cord Blood in One Case of Pregnancy-Associated Breast Cancer Seen by Fluorescence Lifetime Imaging Microscopy," *Diagnostics,* vol. 11, no. 8, 2021, doi: 10.3390/diagnostics11081494.

[26] B. Pradère *et al.,* "Two-photon optical imaging, spectral and fluorescence lifetime analysis to discriminate urothelial carcinoma grades," *Journal of Biophotonics,* https://doi.org/10.1002/jbio.201800065 vol. 11, no. 11, p. e201800065, 2018/11/01 2018, doi: https://doi.org/10.1002/jbio.201800065.

[27] A. Batista, H. G. Breunig, T. Hager, B. Seitz, and K. König, "Early evaluation of corneal collagen crosslinking in ex-vivo human corneas using two-photon imaging," *Scientific Reports,* vol. 9, no. 1, p. 10241, 2019/07/15 2019, doi: 10.1038/s41598-019-46572-3.

[28] S. Coda *et al.,* "Fluorescence lifetime spectroscopy of tissue autofluorescence in normal and diseased colon measured ex vivo using a fiber-optic probe," *Biomedical Optics Express,* vol. 5, no. 2, pp. 515-538, 2014/02/01 2014, doi: 10.1364/BOE.5.000515.

[29] W. C. Zúñiga *et al.*, "Raman Spectroscopy for Rapid Evaluation of Surgical Margins during Breast Cancer Lumpectomy," *Scientific Reports*, vol. 9, no. 1, p. 14639, 2019/10/10 2019, doi: 10.1038/s41598-019-51112-0.

[30] X. Liu *et al.*, "Fast fluorescence lifetime imaging techniques: A review on challenge and development," *Journal of Innovative Optical Health Sciences*, vol. 12, no. 05, p. 1930003, 2019/09/01 2019, doi: 10.1142/S1793545819300039.

[31] J. D. Visgauss, W. C. Eward, and B. E. Brigman, "Innovations in Intraoperative Tumor Visualization," *Orthopedic Clinics*, vol. 47, no. 1, pp. 253-264, 2016, doi: 10.1016/j.ocl.2015.08.023.

[32] J. Pei-Chi, M. S. Oscar, and S. G. M. D. Warren, "Quasi-real-time fluorescence imaging with lifetime dependent contrast," *Journal of Biomedical Optics*, vol. 16, no. 8, pp. 1-10, 8/1 2011, doi: 10.1117/1.3609229.

[33] C. Harrison *et al.*, "Dynamic optical contrast imaging (DOCI): system theory for rapid, wide-field, multispectral optical imaging using fluorescence lifetime contrast mechanism," in *Proc.SPIE*, 2019, vol. 10951, doi: 10.1117/12.2513823. [Online]. Available: https://doi.org/10.1117/12.2513823

[34] M. Kasha, "Characterization of electronic transitions in complex molecules," *Discussions of the Faraday society*, vol. 9, pp. 14-19, 1950.

[35] L.-C. Chen *et al.*, "The potential of label-free nonlinear optical molecular microscopy to non-invasively characterize the viability of engineered human tissue constructs," *Biomaterials*, vol. 35, no. 25, pp. 6667-6676, 2014.

[36] M. Y. Berezin and S. Achilefu, "Fluorescence lifetime measurements and biological imaging," *Chemical reviews*, vol. 110, no. 5, pp. 2641-2684, 2010.

[37] J. R. Lakowicz, *Principles of fluorescence spectroscopy*. Springer science & business media, 2013.

[38] L. Marcu, "Fluorescence lifetime techniques in medical applications," *Annals of biomedical engineering,* vol. 40, no. 2, pp. 304-331, 2012.

[39] C. D. Geddes and J. R. Lakowicz, *Reviews in fluorescence 2006*. Springer, 2005.

[40] J. McGinty *et al.*, "Wide-field fluorescence lifetime imaging of cancer," *Biomedical optics express,* vol. 1, no. 2, pp. 627-640, 2010.

[41] E. Gratton, S. Breusegem, J. D. Sutin, Q. Ruan, and N. P. Barry, "Fluorescence lifetime imaging for the two-photon microscope: time-domain and frequency-domain methods," *Journal of biomedical optics,* vol. 8, no. 3, pp. 381-391, 2003.

[42] M. A. Digman, V. R. Caiolfa, M. Zamai, and E. Gratton, "The phasor approach to fluorescence lifetime imaging analysis," *Biophysical journal,* vol. 94, no. 2, pp. L14-L16, 2008.

[43] H. Yong, S. M. Andy, P. Peter, H. Shan, S. Oscar, and J. Maie St, "Design and validation of an intraoperative autofluorescence lifetime imaging device," in *Proc.SPIE*, 2020, vol. 11213, doi: 10.1117/12.2560000. [Online]. Available: https://doi.org/10.1117/12.2560000

[44] H. Cheng, "Translational Research for Biophotonics Image-Guided Surgery," UCLA, 2018.

[45] "Andor SDK2 - Software Manual." [Online]. Available: https://andor.oxinst.com/downloads/uploads/Andor_Software_Development_Kit_2.pdf

[46] T. G. Scott, R. D. Spencer, N. J. Leonard, and G. Weber, "Synthetic spectroscopic models related to coenzymes and base pairs. V. Emission properties of NADH. Studies of

fluorescence lifetimes and quantum efficiencies of NADH, AcPyADH, [reduced acetylpyridineadenine dinucleotide] and simplified synthetic models," *Journal of the American Chemical Society,* vol. 92, no. 3, pp. 687-695, 1970/02/01 1970, doi: 10.1021/ja00706a043.

[47] J. Galbán, I. Sanz-Vicente, J. Navarro, and S. de Marcos, "The intrinsic fluorescence of FAD and its application in analytical chemistry: a review," *Methods and Applications in Fluorescence,* vol. 4, no. 4, p. 042005, 2016/12/19 2016, doi: 10.1088/2050-6120/4/4/042005.

[48] N. I. f. O. Safety and Health, *Criteria for a Recommended Standard ... Occupational Exposure to Ultraviolet Radiation*. 1972.

[49] S. Au - Deborde *et al.*, "An In Vivo Murine Sciatic Nerve Model of Perineural Invasion," *JoVE,* no. 134, p. e56857, 2018/04/23/ 2018, doi: doi:10.3791/56857.

[50] M. C. Skala *et al.*, "In vivo multiphoton microscopy of NADH and FAD redox states, fluorescence lifetimes, and cellular morphology in precancerous epithelia," *Proceedings of the National Academy of Sciences,* vol. 104, no. 49, p. 19494, 2007, doi: 10.1073/pnas.0708425104.

[51] A. T. Shah, M. Demory Beckler, A. J. Walsh, W. P. Jones, P. R. Pohlmann, and M. C. Skala, "Optical Metabolic Imaging of Treatment Response in Human Head and Neck Squamous Cell Carcinoma," *PLOS ONE,* vol. 9, no. 3, p. e90746, 2014, doi: 10.1371/journal.pone.0090746.

[52] R. A. Schwarz *et al.*, "Noninvasive evaluation of oral lesions using depth-sensitive optical spectroscopy," *Cancer,* https://doi.org/10.1002/cncr.24177 vol. 115, no. 8, pp. 1669-1679, 2009/04/15 2009, doi: https://doi.org/10.1002/cncr.24177.

[53] D. M. Press *et al.*, "The prevalence of undiagnosed and unrecognized primary hyperparathyroidism: a population-based analysis from the electronic medical record," *Surgery*, vol. 154, no. 6, pp. 1232-1238, 2013.

[54] R. A. DeLellis, P. Mazzaglia, and S. Mangray, "Primary hyperparathyroidism: a current perspective," *Archives of pathology & laboratory medicine*, vol. 132, no. 8, pp. 1251-1262, 2008.

[55] B. C. Silva, N. E. Cusano, and J. P. Bilezikian, "Primary hyperparathyroidism," *Best practice & research Clinical endocrinology & metabolism*, vol. 32, no. 5, pp. 593-607, 2018.

[56] J. Baj *et al.*, "Preoperative and intraoperative methods of parathyroid gland localization and the diagnosis of parathyroid adenomas," *Molecules*, vol. 25, no. 7, p. 1724, 2020.

[57] A. Mohebati and A. R. Shaha, "Imaging techniques in parathyroid surgery for primary hyperparathyroidism," *American journal of otolaryngology*, vol. 33, no. 4, pp. 457-468, 2012.

[58] A. Wong, J. C. Wong, P. U. Pandey, and S. M. Wiseman, "Novel techniques for intraoperative parathyroid gland identification: a comprehensive review," *Expert Review of Endocrinology & Metabolism*, vol. 15, no. 6, pp. 439-457, 2020.

[59] M. Schneider *et al.*, "Complete and incomplete recurrent laryngeal nerve injury after thyroid and parathyroid surgery: Characterizing paralysis and paresis," *Surgery*, vol. 166, no. 3, pp. 369-374, 2019.

[60] A. K. Dewan, S. B. Kapadia, C. S. Hollenbeak, and B. C. Stack Jr, "Is routine frozen section necessary for parathyroid surgery?," *Otolaryngology—Head and Neck Surgery*, vol. 133, no. 6, pp. 857-862, 2005.

[61] N. E. Dudley, "Methylene blue for rapid identification of the parathyroids," *Br Med J,* vol. 3, no. 5776, pp. 680-681, 1971.

[62] J. Bewick and A. Pfleiderer, "The value and role of low dose methylene blue in the surgical management of hyperparathyroidism," *The Annals of The Royal College of Surgeons of England,* vol. 96, no. 7, pp. 526-529, 2014.

[63] P. Jitpratoom and A. Anuwong, "The use of ICG enhanced fluorescence for the evaluation of parathyroid gland preservation," *Gland surgery,* vol. 6, no. 5, p. 579, 2017.

[64] S. M. Sadowski, J. V. Fortuny, and F. Triponez, "A reappraisal of vascular anatomy of the parathyroid gland based on fluorescence techniques," *Gland surgery,* vol. 6, no. Suppl 1, p. S30, 2017.

[65] C. Paras, M. Keller, A. Mahadevan-Jansen, L. White, and J. Phay, "Near-infrared autofluorescence for the detection of parathyroid glands," *Journal of biomedical optics,* vol. 16, no. 6, p. 067012, 2011.

[66] M. A. McWade *et al.*, "Label-free intraoperative parathyroid localization with near-infrared autofluorescence imaging," *The Journal of Clinical Endocrinology & Metabolism,* vol. 99, no. 12, pp. 4574-4580, 2014.

[67] S. W. Kim *et al.*, "Intraoperative real-time localization of normal parathyroid glands with autofluorescence imaging," *The Journal of Clinical Endocrinology & Metabolism,* vol. 101, no. 12, pp. 4646-4652, 2016.

[68] R. M. Devine, J. A. Van Heerden, C. S. Grant, and J. J. Muir, "The role of methylene blue infusion in the management of persistent or recurrent hyperparathyroidism," *Surgery,* vol. 94, no. 6, pp. 916-918, 1983.

[69] W. Chu, A. Chennamsetty, R. Toroussian, and C. Lau, "Anaphylactic Shock After Intravenous Administration of Indocyanine Green During Robotic Partial Nephrectomy," *Urology Case Reports,* vol. 12, pp. 37-38, 2017/05/01/ 2017, doi: https://doi.org/10.1016/j.eucr.2017.02.006.

[70] P. Dewachter, C. Mouton-Faivre, P. Trechot, J.-C. Lleu, and P. M. Mertes, "Severe anaphylactic shock with methylene blue instillation," *Anesthesia & Analgesia,* vol. 101, no. 1, pp. 149-150, 2005.

[71] B. Kahramangil *et al.*, "Detection of parathyroid autofluorescence using near-infrared imaging: a multicenter analysis of concordance between different surgeons," *Annals of surgical oncology,* vol. 25, no. 4, pp. 957-962, 2018.

[72] M. Hollander, D. A. Wolfe, and E. Chicken, *Nonparametric statistical methods*. John Wiley & Sons, 2013.

[73] A. J. Walsh *et al.*, "Classification of T-cell activation via autofluorescence lifetime imaging," *Nature biomedical engineering,* vol. 5, no. 1, pp. 77-88, 2021.

[74] K. Samimi, E. C. Guzman, S. M. Trier, D. L. Pham, T. Qian, and M. C. Skala, "Time-domain single photon-excited autofluorescence lifetime for label-free detection of T cell activation," *Optics letters,* vol. 46, no. 9, pp. 2168-2171, 2021.

[75] C. A. Gómez *et al.*, "Phasor analysis of NADH FLIM identifies pharmacological disruptions to mitochondrial metabolic processes in the rodent cerebral cortex," *PLoS one*, vol. 13, no. 3, p. e0194578, 2018.

[76] Q. Yang, M. Qi, Z. Wu, L. Liu, P. Gao, and J. Qu, "Classification of skin cancer based on fluorescence lifetime imaging and machine learning," in *Optics in Health Care and*

Biomedical Optics X, 2020, vol. 11553: International Society for Optics and Photonics, p. 115531Y.

[77] M. A. K. Sagar, K. P. Cheng, J. N. Ouellette, J. C. Williams, J. J. Watters, and K. W. Eliceiri, "Machine Learning Methods for Fluorescence Lifetime Imaging (FLIM) Based Label-Free Detection of Microglia," (in eng), *Front Neurosci*, vol. 14, pp. 931-931, 2020, doi: 10.3389/fnins.2020.00931.

[78] Y. Hu *et al.*, "A Tool to Locate Parathyroid Glands Using Dynamic Optical Contrast Imaging," *The Laryngoscope*, vol. 131, no. 10, pp. 2391-2397, 2021.

[79] M. P. Brandao *et al.*, "Optical Characterization of Parathyroid Tissues," *Applied spectroscopy*, vol. 70, no. 10, pp. 1709-1716, 2016.

[80] J. Guilmette and P. M. Sadow, "Parathyroid pathology," *Surgical pathology clinics*, vol. 12, no. 4, pp. 1007-1019, 2019.

[81] R. Datta, T. M. Heaster, J. T. Sharick, A. A. Gillette, and M. C. Skala, "Fluorescence lifetime imaging microscopy: fundamentals and advances in instrumentation, analysis, and applications," *Journal of biomedical optics*, vol. 25, no. 7, p. 071203, 2020.

[82] B. A. Tajudeen *et al.*, "Dynamic optical contrast imaging as a novel modality for rapidly distinguishing head and neck squamous cell carcinoma from surrounding normal tissue," *Cancer*, vol. 123, no. 5, pp. 879-886, 2017.

[83] A. J. Sherman *et al.*, "Normalized fluorescence lifetime imaging for tumor identification and margin delineation," in *Advanced Biomedical and Clinical Diagnostic Systems XI*, 2013, vol. 8572: International Society for Optics and Photonics, p. 85721H.

[84] I. A. Kim *et al.*, "Dynamic optical contrast imaging: A technique to differentiate parathyroid tissue from surrounding tissues," *Otolaryngology–Head and Neck Surgery*, vol. 156, no. 3, pp. 480-483, 2017.

[85] H. Sung *et al.*, "Global Cancer Statistics 2020: GLOBOCAN Estimates of Incidence and Mortality Worldwide for 36 Cancers in 185 Countries," *CA: A Cancer Journal for Clinicians*, https://doi.org/10.3322/caac.21660 vol. 71, no. 3, pp. 209-249, 2021/05/01 2021, doi: https://doi.org/10.3322/caac.21660.

[86] J. D. Meier, D. A. Oliver, and M. A. Varvares, "Surgical margin determination in head and neck oncology: Current clinical practice. The results of an International American Head and Neck Society Member Survey," *Head & Neck*, https://doi.org/10.1002/hed.20269 vol. 27, no. 11, pp. 952-958, 2005/11/01 2005, doi: https://doi.org/10.1002/hed.20269.

[87] A. Binahmed, R. W. Nason, and A. A. Abdoh, "The clinical significance of the positive surgical margin in oral cancer," *Oral Oncology*, vol. 43, no. 8, pp. 780-784, 2007/09/01/ 2007, doi: https://doi.org/10.1016/j.oraloncology.2006.10.001.

[88] J. Pan *et al.*, "Real-time surveillance of surgical margins via ICG-based near-infrared fluorescence imaging in patients with OSCC," *World Journal of Surgical Oncology*, vol. 18, no. 1, p. 96, 2020/05/15 2020, doi: 10.1186/s12957-020-01874-z.

[89] M. Merve, K. Ronald, A. Angelika, H. Ulrike, and T. Hagen, "Wavelength-dependent penetration depths of ultraviolet radiation in human skin," *Journal of Biomedical Optics*, vol. 13, no. 4, pp. 1-5, 7/1 2008, doi: 10.1117/1.2957970.

[90] D. Pulte and H. Brenner, "Changes in Survival in Head and Neck Cancers in the Late 20th and Early 21st Century: A Period Analysis," *The Oncologist,* vol. 15, no. 9, pp. 994-1001, 2010, doi: 10.1634/theoncologist.2009-0289.

[91] K. K. Jakobsen *et al.*, "Increasing incidence and survival of head and neck cancers in Denmark: a nation-wide study from 1980 to 2014," *Acta Oncologica,* vol. 57, no. 9, pp. 1143-1151, 2018/09/02 2018, doi: 10.1080/0284186X.2018.1438657.

[92] Y.-J. Kim and J. H. Kim, "Increasing incidence and improving survival of oral tongue squamous cell carcinoma," *Scientific Reports,* vol. 10, no. 1, p. 7877, 2020/05/12 2020, doi: 10.1038/s41598-020-64748-0.

[93] E. A. Van Dyne, S. J. Henley, M. Saraiya, C. C. Thomas, L. E. Markowitz, and V. B. Benard, "Trends in Human Papillomavirus-Associated Cancers - United States, 1999-2015," (in eng), *MMWR Morb Mortal Wkly Rep,* vol. 67, no. 33, pp. 918-924, 2018, doi: 10.15585/mmwr.mm6733a2.

[94] J. R. de Almeida *et al.*, "Oncologic Outcomes After Transoral Robotic Surgery : A Multi-institutional Study," *JAMA Otolaryngology–Head & Neck Surgery,* vol. 141, no. 12, pp. 1043-1051, 2015, doi: 10.1001/jamaoto.2015.1508.

[95] F. Bray, J.-S. Ren, E. Masuyer, and J. Ferlay, "Global estimates of cancer prevalence for 27 sites in the adult population in 2008," *International Journal of Cancer,* https://doi.org/10.1002/ijc.27711 vol. 132, no. 5, pp. 1133-1145, 2013/03/01 2013, doi: https://doi.org/10.1002/ijc.27711.

[96] G. F. Funk, L. H. Karnell, R. A. Robinson, W. K. Zhen, D. K. Trask, and H. T. Hoffman, "Presentation, treatment, and outcome of oral cavity cancer: A national cancer data base

report," *Head & Neck,* https://doi.org/10.1002/hed.10004 vol. 24, no. 2, pp. 165-180, 2002/02/01 2002, doi: https://doi.org/10.1002/hed.10004.

[97] A. Chamoli *et al.,* "Overview of oral cavity squamous cell carcinoma: Risk factors, mechanisms, and diagnostics," *Oral Oncology,* vol. 121, p. 105451, 2021/10/01/ 2021, doi: https://doi.org/10.1016/j.oraloncology.2021.105451.